DIR

Diagnostic and Interventional
Radiology

Contents

Full text of these articles can be accessed online at www.dirjournal.org or through PubMed (https://www.ncbi.nlm.nih.gov/pmc/journals/2754/).

Dear Reviewers,

Thank you for your invaluable contributions as reviewers to Diagnostic and Interventional Radiology in 2024. Your expertise and insightful feedback have helped to maintain our journal's high standards and ensure the quality of the articles we publish. We appreciate your interest in our journal and wish you every success in your academic career.

Sincerely,

Abidin Kılınçer	Bilgin Kadri Arıbaş	Fatih Erdem
Adalet Elçin Yıldız	Bo Liang	Fatma Bilge Ergen
Afak Durur Karakaya	Bora Korkmazer	Fatma Harman
Afonso César Polimanti	Bora Peynircioğlu	Fazıl Gelal
Ahmet Baki Yağcı	Bökebatur Ahmet Raşit Mendi	Ferhat Can Pişkin
Ahmet Erdemir	Bright Benfor	Fırat Atak
Ahmet Kürşad Poyraz	Burak Binboğa	Figen Demirkazik
Ahmet Rahmi Onur	Burak Koçak	Filiz Elbüken
Ahmet Sığırcı	Burçak Çakır Peköz	Funda Dinç
Alexandra Fairchild	Bünyamin Ece	Furkan Ufuk
Ali Balcı	Carlos A Farinas	Gamze Durhan
Ali Fuat Tekin	Cem Önal	Gary Horn
Ali Yusuf Öner	Cem Yücel	Geert Maleux
Alper Selver	Costantino Del Giudice	Georgios Kalarakis
Alperen Elek	Çağdaş Topel	Giorgio Treglia
Anish Kirpalani	Çağlar Uzun	Gizem Timoçin Yığman
Anuradha S. Shenoy-Bhangle	Çağrı Erdim	Gonca Eldem
Arnaldo Stanzione	Daniel Gräfe	Gökçe Kaan Ataç
Aslı Tanrıvermiş Sayıt	Daniella Braz Parente	Gökçen Çoban
Atilla Hikmet Çilengir	David Laszlo Tarnoki	Gökhan Gökalp
Aydın Demircioğlu	Dilek Sağlam	Gregoire Boulouis
Aydın Eresen	Dita Aditianingsih	Gülnur Erdem
Aymen Meddeb	Duygu Özgül Özesen	Güven Kahriman
Aysenur Oktay	Ece Ateş Kuş	H. Nursun Özcan
Ayşe Kalyoncu Uçar	Ekim Gümeler	Habibe İnci
Ayşe Özlem Balık	Elena Belloni	Haitao Yang
Aytaç Gülcü	Elif Günay Bulut	Hakan Artaş
Aytül Hande Yardımcı	Emre Ünal	Hale Aydın
Bahri Üstünsöz	Ercan Ayaz	Harri Merisaari
Baki Hekimoglu	Erkan Gökçe	Hasan Yigit
Barış Türkbey	Erkin Arıbal	Hector Ferral
Başak Atalay	Esra Özkavukcu	Huseyin Tugsan Balli
Berat Acu	Evren Üstüner	Ina Sorge
Berna Dirim Mete	Ezgi Güler	Irmak Durur Subaşı
Betül Emine Derinkuyu	Fabio Corvino	Işıl Basara Akın

İlkay Çamlıdağ

İlkay S. İdilman

İlker Ercan

İnci Kızıldağ Yırgın

İsmail Akdulum

İsmail Meşe

İsmail Oran

Jatin Singh

Jean-Marc Alsac

Ji Hoon Shin

Jiaywei Tsauo

Jie Lee

Jin Ho Hwang

Jing Ye

Jingyu Zhong

Joanie M Garratt

John O. Delancey

Jonathan Pace

Jonghyouk Yun

Joost A. Bekken

Jorge Lopera

Jose Luis Del Cura

Joshua Hanna

Juergen Machann

Justin P. Mcwilliams

Kader K. Oğuz

Kamil Karaali

Kemal Buğra Memiş

Keno Bressem

Kerim Aslan

Kewen Jiang

Kohzoh Makita

Kumi Ozaki

Kunwarpal Singh

Kutsev Bengisu Özyörük

L. Gilbert Vezina

Lin Qi

Lixin Wang

Liza Lindenberg

Makato Aoki

Marc A. Raj

Marco Oderda

Martin Rössle

Martin Weng Chin Hng

Matthew G.Cable

Mehmet Öztürk

Mehmet Fatih İnecikli

Mehmet Ruhi Onur

Mehmet Sedat Durmaz

Melis Baykara Ulusan

Merter Keçeli

Michail E. Klontzas

Mohab Elmohr

Mohamed-Ihab Reda

Mohammad Alarifi

Mohammad Hadi Gharib

Muhammed Said   Beşler

Muhammed Tekinhatun

Murat Baykara

Murat Beyhan

Murat Canyiğit

Murat Velioğlu

Murat Yüce

Mustafa Ege Seker

Mustafa Mahmut   Barış

Mutlu Gülbay

Nail Bulakbaşı

Naim Ceylan

Nam Yeol Yim

Natally Horvat

Nermin Tunçbilek

Nicola Pirozzi

Nil Tokgöz

Nuno Adubeiro

Nurdan Çay

Nuri Karabay

Nursel Yurttutan

Oğuz Dicle

Oğuzhan Tokur

Okan Akhan

Okan İnce

Onur Buğdaycı

Onur Taydaş

Osman Kızılkılıç

Osman Melih Topçuoğlu

Osman Ocal

Ömer Kaya

Özgur Tosun

Özüm Yüksel Buğdaycı

Pankaj Sharma

Patrick Krumm

Patrick O. Richard

Paul M. Bunch

Peter Brader

Pınar Balcı

Polat Göktaş

Rafael De Athayde

Rafael De Freitas

Ravza Yılmaz

Raymond F. Sekula

Recep Sade

Renato Franco

Rengarajan Rajagopal

Rıfat Özpar

Roberto Cannella

Rupi Jamwal

Sabahattin Yüzkan

Şafak Parlak

Sanjay Rastogi

Sara Marziali

Sara Pacella

Sari Vahaaho

Sebastiano Piana

Selin Ardalı Düzgün

Sena Tunçer Azamat

Serçin Özkök

Sevtap Arslan

Shaun M. Honig

Sherif Elsherif

Shintaro Ichikawa

Shiyu Wang

Simay Altan Kara

Sinan Balcı

Sriram Jaganathan

Stanimir Sirakov

Stefan Ruschke

Suzan Şaylısoy

Syed Naseer Ahmad Shah

Şebnem Örgüç

Preoperative prediction of lymphovascular invasion and T-staging of rectal cancer via a dual-energy computed tomography iodine map: a feasibility study

Jinliang Zhang[1]*
Hui Qi[2]*
Chun Yang[2]
Ling Liu[3]
Yuxin Wang[2]
Wei Li[2]

[1]Shandong Public Health Clinical Center, Department of Medical Imaging, Jinan, China

[2]The First Affiliated Hospital of Shandong First Medical University, Department of Medical Imaging, Jinan, China

[3]GE Healthcare, CT Imaging Research Center, Shanghai, China

PURPOSE

To investigate the value of dual-energy computed tomography (DECT) in predicting lymphovascular invasion (LVI) and the accuracy of preoperative T-staging of rectal cancer (RC).

METHODS

Forty-nine patients with RC who had not received radiotherapy were enrolled to undergo a DECT scan. All patients underwent surgical tumor resection within 3–5 days after the DECT scan. Preoperative T-staging of RC based on images was performed by experienced radiologists. The normalized iodine concentrations (NIC) of the tumor and the perirectal adipose tissue (PAT) from the arterial phase (AP) and venous phase (VP) were measured using DECT. The tumor LVI and T-staging confirmed by pathology were used as the gold standard for grouping (group A, LVI–; group B, LVI+; group C, T1-2; and group D, T3-4a). The NIC values between two groups were compared using the Mann–Whitney U test, with $P < 0.05$ indicating a statistically significant difference. The accuracy of NIC in predicting LVI and distinguishing T1-2 RC from T3-4a RC were determined via receiver operating characteristic curve analysis, and the optimal cut-off of NIC was determined using the area under the curve.

RESULTS

The tumor NIC values were significantly higher in the LV+ group than in the LVI– group in the VP (0.728 ± 0.031 vs. 0.669 ± 0.034, $P < 0.001$). The NIC values of PAT were significantly higher in the T3-4a group than in the T1-2 group in both the AP (4.034 ± 0.991 vs. 3.115 ± 0.581, $P < 0.05$) and the VP (5.481 ± 1.054 vs. 3.450 ± 0.980, $P < 0.001$). The accuracy of using NIC values to distinguish between the LVI+ group and the LVI– group and to diagnose the T3-4a group were 85.7% and 89.8%, respectively. However, there was no statistically significant difference between the NIC value in the LVI+ group and in the LVI– group in the AP. There was also no statistical difference in the tumor NIC value between the T1-2 group and the T3-4a group.

CONCLUSION

The tumor and PAT NIC are valuable indicators in RC that can preoperatively predict LVI and improve the accuracy of preoperative RC T-staging.

CLINICAL SIGNIFICANCE

The use of DECT improves the T-staging and LVI prediction of RC, which is helpful in guiding the clinical selection of appropriate treatment modalities and improving prognostic outcomes.

KEYWORDS

DECT, lymphovascular invasion, normalized iodine concentration, rectal cancer, T-staging

*Joint first authors

Corresponding author: Wei Li

E-mail: lwqfsh@126.com

According to the 2022 global cancer statistics, rectal cancer (RC) is the third most common malignant cause of morbidity (19.5%) and mortality (9.0%) and has become a major global health problem.[1] Preoperative staging of patients using imaging instruments has a great clinical significance for formulating the best possible individualized treatment plan.[2] Currently, TNM staging is globally recognized as a standard staging system for distinguishing the extent of cancer spread. The T-stages of RC according to the 8th edition of the cancer staging manual[3] are shown in Table 1. This staging system has a notable clinical significance for preoperatively distinguishing between stage T1-2 RC and stage T3-4 RC,[4] and relevant research shows that patients with T1-2 RC have a low recurrence rate after radical surgery, which can effectively prolong the survival period; in contrast, patients with T3-4 RC do not directly benefit from surgery, and preoperative adjuvant radiotherapy and chemotherapy are needed to improve the surgical resection and radical cure rate.[5] Whether there is lymphovascular invasion (LVI) can be a decidable indicator of preoperative adjuvant chemotherapy.[6] For patients with stage T3-4 or LVI+ RC, declining the adenocarcinoma grade before surgery is significant for treatment and prognosis.[1,7]

Transrectal ultrasonography (TRUS) and magnetic resonance imaging (MRI) have been widely used for preoperative T-staging of RC, and the diagnostic accuracies of TRUS for preoperative T-staging of patients with RC have been reported in the literature to range from 71% to 95%.[8] However, the diagnostic accuracy of TRUS is highly dependent on the experience and skill of the operator.[9] Moreover, the field of view of TRUS is limited, and high-grade and stenotic tumors are often difficult to reach with the probe.[10] Preoperative T-staging of patients with RC via MRI has been proven to have an accuracy of 65%–86%, and MRI has become the most commonly used technology in clinical rectal examination.[11,12] However, despite the many advantages of the radiation-free rectal MRI, the examination is expensive, requires a long scanning time and presents a potential safety risk for some specific individuals (e.g., those with metal implants, claustrophobia, and epilepsy).[13] In addition, the preparation for patients with RC is challenging (e.g., the gas and fluid in the intestines and other intestinal contents present during the examination produce artifacts on MRI images). The main advantages of computed tomography (CT) when compared with MRI are more available clinical scanning and a shorter scanning time; thus, CT is often used to detect distant metastases in patients with RC. In clinical practice, radiologists also use conventional CT to complete preoperative-image naked-eye T-staging of RC. Some studies[12,14] note that it is difficult to precisely distinguish stage T2 RC and T3 RC using CT or MRI images, since the rectal surface is rough, and the indication of peripheral fat is uneven. Therefore, determining whether the condition is caused by tumor infiltration from only the imaging point of view is complicated. Moreover, inflammatory exudation is easily misdiagnosed as a fibrous cord of adipose tissue around the RC in cancer invasion, causing a high false positive rate for clinical diagnosis of stage T3 RC. Similarly, the appearance of a tumor invading the surrounding soft tissue is difficult to distinguish from blood vessels or local inflammation, often leading to radiologists misdiagnosing stage T3 RC as stage T2 RC. Sometimes, inflammation, image artifacts, small blood vessels, and other factors may also lead to the same imaging results. As a result, the rate of misdiagnosing stage T2 RC as stage T3 RC in clinical practice is high.

In summary, novel methods for improving the sensitivity, specificity, and accuracy of preoperative prediction of LVI and T-staging of RC are in high demand.

Dual-energy computed tomography (DECT) uses two X-ray beams of different energy levels to simultaneously scan the desired object, showing both alterations in conventional CT features and quantitatively reflecting differences in the energetic categories of tissues, thus providing many quantitative parameters reflecting biological properties, such as iodine concentration (IC).[15] The iodine-based images provided by DECT are pseudo-color images.[16,17] Compared with the images provided by conventional CT, which only provide a CT value, DECT iodine-based images are more convenient for naked-eye distinguishing of the RC invasion extent. In addition, the IC provided by DECT is a quantitative parameter that can provide a better objective basis for diagnosis. For early invasion of cancer cells, abnormal tumor angiogenesis appears in the affected area, and DECT can evaluate the microcirculation in the region of interest (ROI) by measuring the concentration of iodine in the adipose tissue around the tumor, thus helping determine whether it has been invaded.[18,19] Furthermore, DECT can detect the iodine density maps in the tissue, since it can simultaneously collect two data sets of different energy spectra in a single acquisition, and iodine has strong photoelectric absorption at the low tube voltage close to the K edge of iodine, making it easily distinguishable from other materials.[18] Related studies have shown that IC in perigastric adipose tissue can predict whether gastric cancer will invade the serosa tissue and determine the T4 stage of gastric cancer.[20] Moreover, DECT has been used to identify various other diseases (e.g., lymph node metastasis of colorectal cancer,[21,22] liver metastasis of colorectal cancer[23-25]) and determine the diagnostic classi-

Main points

- Preoperative prediction of lymphovascular invasion (LVI) and T-staging of rectal cancer (RC) via a dual-energy computed tomography (DECT) iodine map.

- Compared with the pathological gold standard, the accuracy of conventional computed tomography in differentiating between T3-4a RC and T1-2 RC was only 67.3%, whereas the accuracy of iodine mapping using DECT was 89.8%. In addition, DECT was relatively effective in predicting LVI positivity (85.7%).

- The obtained results showed that the normalized iodine concentration of the tumor and the perirectal adipose tissue in RC can preoperatively predict LVI and improve the accuracy of T-staging.

Table 1. T-staging for rectal cancer

T-staging		Rectal wall involvement/description
T0		No evidence of primary tumor
Tis		Carcinoma *in situ*, intramucosal (tumor invades the *lamina propria* of the mucosa but does not break through the muscular layer of the mucosa)
T1		Tumor invasion of the submucosa
T2		Tumor invasion of the *lamina propria*
T3		Tumor penetration of the intrinsic muscular layer to reach the sub-plasma layer or invasion of paracolorectal tissue without peritoneal coverage
T4	T4a	Tumor penetration of the peritoneal visceral layer
	T4b	Tumor directly invades or adheres to adjacent organs or structures

fication of benign and malignant colorectal lymph nodules.[26] Thus, this study aims to evaluate the value of IC in RC PAT and tumors using DECT in predicting (i) pre-operative LVI and (ii) the accuracy of preoperative RC T-staging.

Methods

Patient characteristics

The study was approved according to the principles of the Declaration of Helsinki by the Local Institutional Ethics Committee of the First Affiliated Hospital of Shandong First Medical University [approval no: 2022 LUN (S521)], and all participants signed a written informed consent form. A total of 62 patients with non-T4b-stage primary RC endoscopically and pathologically confirmed between November 2020 and February 2022 were retrospectively enrolled in the study. The 62 patients underwent preoperative DECT scanning at the First Affiliated Hospital of Shandong First Medical University. All enrolled patients underwent three-phase DECT scans, including unenhanced CT scan and contrast-enhanced arterial phase (AP) and venous phase (VP) DECT scans.

Of the 62 patients initially included in the study, 13 were excluded (2 without adequate intestinal preparation, 2 who underwent surgery more than a week after the CT scan, 3 with severe image artifacts, 4 who refused to accept any treatment, and 2 who underwent preoperative neoadjuvant chemotherapy). A

final number of 49 subjects was selected (33 men and 16 women), with an average age of 61.3 years (31–76 years). The inclusion and exclusion criteria are summarized in Figure 1, and the patient characteristics are shown in Table 2.

The surgically resected tissue specimens were pathologically examined and utilized as the gold standard to determine the RC stage. Some studies stage-divided RC into the T1-2 group and the T3-4 group based on prognosis.[27,28] Considering that the T4b stage could be clearly differentiated from the T3 stage on CT images, all enrolled patients with stage T4 RC indicated stage T4a RC. Finally, the patients were divided into group A (LVI–) and group B (LVI+); group C (no serosa invasion, T1-2), and group D (serosa invasion, T3-4a).

Dual-energy computed tomography scan

All DECT images were acquired using a 256-row energy spectrum CT scanner (Revolution CT, GE Healthcare, WI, USA). An intestine preparation time of 30 minutes was required per patient before the CT examination. A mixture of pure water and medical ultrasonic couplants at a ratio of 1:1 was prepared and injected into the rectum based on the distance between the tumor and the anus. Moreover, 400 mL of water was given to patients before the DECT examination.

All patients received routine intravenous administration, followed by an intravenous injection of the contrast agent, iopromide

(370 mg iodine/mL, Ultravist®, Bayer Schering Pharma), through the elbow vein at a flow rate of 4 mL/s. The injection dose of the contrast agent was calculated based on the body weight (2 mL/kg) of each patient. The scanning of the AP was triggered at a threshold of 100 HU for the abdominal aorta. After a delay of 40 seconds, VP scanning was performed. Thus, DECT images in the AP and VP were achieved.

The conventional imaging acquisition protocol was as follows: tube voltage = 120 kVp; automatic tube current modulation range = 200–720 mA; noise index (NI) = 10; rotation time = 0.8 s; detector coverage = 80 mm; scan slice thickness = 5 mm; reconstructed thickness/interval = 0.625/0.625 mm; and pitch = 0.992:1. The spectral (Gemstone Spectral Imaging) mode was used in both the AP and VP using the following parameters: tube voltage = 80 and 140 kVp with a tin filter; tube currents = 190 mA; NI = 10; rotation time = 0.8 s; detector coverage = 80 mm; scan slice thickness = 5 mm; reconstructed thickness/interval = 0.625/0.625 mm; and pitch = 0.992:1.

Image analysis and quantitative parameters

Two experienced radiologists performed naked-eye preoperative T-staging of patients with RC using a PACS system and conventional CT images, as shown in Figure 2, Figure 3a and b. The staging was as follows: (1) T1-2 stage: the tumor had invaded the
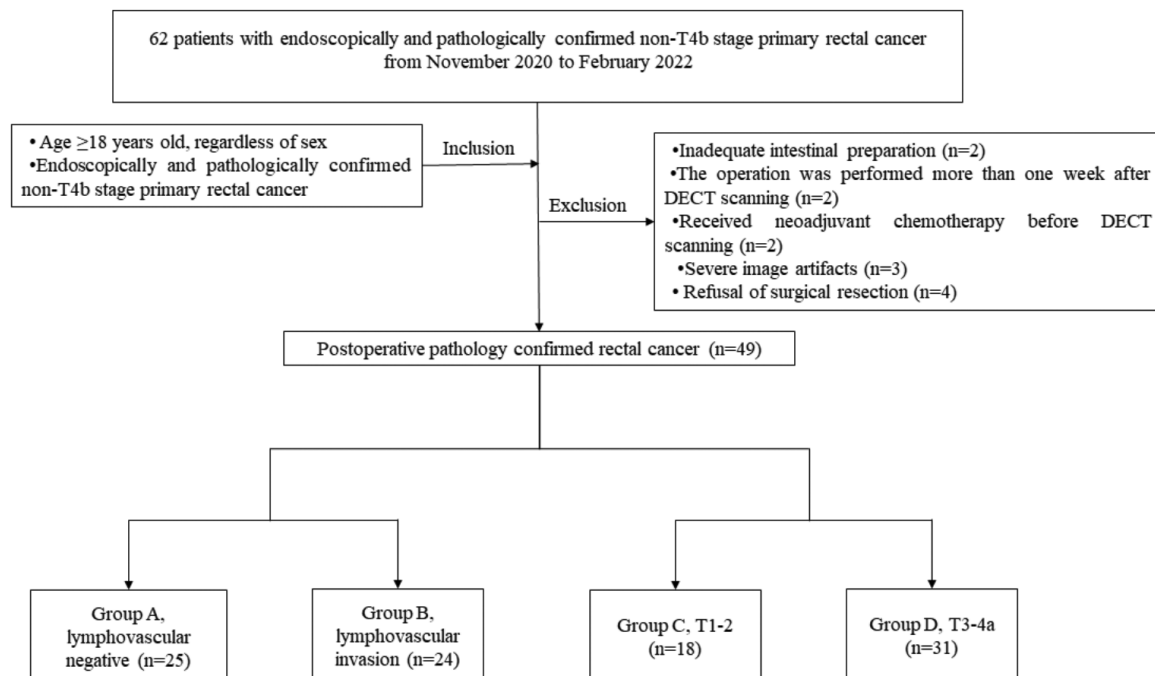
Figure 1. Flowchart showing the inclusion and exclusion criteria for patient selection. DECT, dual-energy computed tomography.

submucosal and muscular layers but had not breached the muscularis propria; (2) T3 stage: the tumor had penetrated the intrinsic muscle layer and reached the lower serosa layer or invaded the perirectal tissue without peritoneal coating; (3) and T4 stage: the tumor had penetrated the serous layer and reached the peritoneum (T4a), or adjacent organs were involved (T4b). Morphological features included plain scan and enhanced scan CT values, whether the tumor edge was blurred, whether the density of adjacent adipose tissue had increased, and whether the surrounding structures and organs had been infiltrated. The radiologists were blinded to the results of IC measurement and histology.

A slice thickness of 0.625 mm was chosen to reconstruct the dual-energy AP and VP iodine-based images to quantitatively measure IC using a GE AW4.2 workstation (GE Healthcare). The IC was calculated by manually delineating ROIs in the tumor, perirectal adipose tissue (PAT), and iliac arteries. A 50–75 mm² ROI was obtained from the tumor and iliac artery, covering as much tumor as possible, outside of blood vessels and necrotic lesions. A 45–70 mm² ROI was found in the PAT; the distance between the ROI and RC intestinal wall was >1 mm, and the ROI didn't involve the tumor intestinal wall.[20] To obtain the adipose tissue normalized IC (NIC), identical ROIs of the same size were placed at the same level in the area away from the tumor (Figure 2, Figure 3c-f).

The corresponding IC was measured from the AP and VP images of each patient. Each measurement was repeated six times (three layers of images were selected for measurement, and the data from each layer were measured twice), and the average IC was recorded for further analysis. The second measurement was completed using the same method after 2 months, and the two measuring results were averaged to obtain more rigorous measurement results.

The NIC_1 values of the initial lesion and the NIC_2 values of the adipose tissue around the RC were calculated using the following formulas:

$$NIC_1 = \frac{IC_{tumor}}{IC_{iliac\,artery}}, NIC_2 = \frac{IC_{near\,the\,RC}}{IC_{away\,from\,RC}},$$

which minimized variations in different patients.

Statistical analysis

Statistical analysis was performed using the SPSS 26.0 software (IBM Corp. Armonk, NY, USA). The Mann–Whitney U test was used to compare the NIC values between group A and group B; $P < 0.05$ was considered statistically significant. The values of NIC_1 and NIC_2 in diagnosing LVI and T3-4a RC were determined via receiver operating characteristic (ROC) curve analysis. The area under the ROC curve (AUC) was used to determine the optimal cut-off of NIC for tumor classification. Inter-observer agreement between two measurements of DECT parameters was evaluated using the interclass correlation coefficient (ICC). The ICC values were as follows: <0.5 = poor reliability; 0.5–0.75 = moderate reliability, 0.75–0.9 = good reliability; and >0.9 = excellent reliability.

Results

Quantitative parameters of dual-energy computed tomography

In the AP, the difference in the NIC_1 values between group A and group B was not statistically significant ($P > 0.05$). However, in the VP, the NIC_1 was significantly higher in group B than in group A (0.728 ± 0.031 vs. 0.669 ± 0.034, $P < 0.001$) (Table 2). For VP images, the ROC curve (Figure 4) analysis of LVI pre-
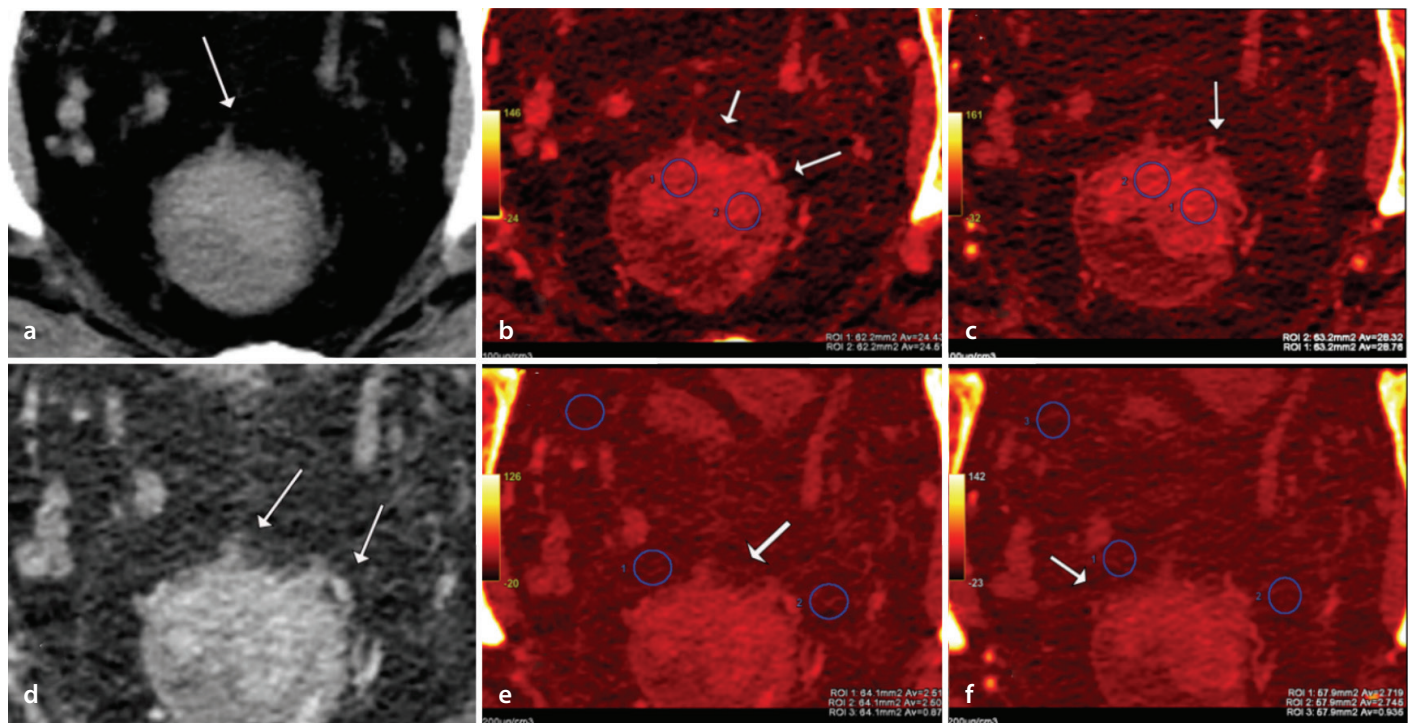
Figure 2. A 60-year-old man with lymphovascular invasion negative stage T2 rectal cancer. The white arrow denotes the thickening and transmural enhancement of the rectal wall. The density of the perirectal fat increases with the stripe-like shadow. In **(a)** and **(b)**, the radiologist diagnosed the rectal tumor as clinical staging T3 with traditional computed tomography (CT) before surgery, but the pathological stage was pathological staging T2; **(c-f)** were used to measure the iodine concentration (IC) in tissues using post-processing techniques; **(c)** and **(d)** show the method of drawing regions of interest (ROIs) on the tumor in the arterial phase (AP) and venous phase (VP), respectively; **(e)** shows that the mean IC was 0.501 mg/mL in the perirectal fat tissue (ROI: 1.2) and 0.175 mg/mL in the fat tissue distant from the tumor in the AP (ROI: 3); **(f)** shows that the mean IC was 0.546 mg/mL in the fat tissue near the tumor (ROI: 1.2), and 0.195 mg/mL in the fat tissue distant from the tumor in the VP (ROI: 3). The dual-energy CT corrected the preoperative T-staging of the patient as non-T3.

diction via DECT denoted that the AUC was 0.868, and the best cut-off of NIC_1 for distinguishing group B from group A was 0.690, with a sensitivity of 87.5%, a specificity of 84.0%, and an accuracy of 85.7%.

There was no statistical difference in the tumor NIC_1 values between group C and group D. However, the NIC_2 was significantly higher in group D than in group C in both the AP (4.034 ± 0.991 vs. 3.115 ± 0.581, $P < 0.05$) and the VP (5.481 ± 1.054 vs. 3.450 ± 0.980, $P < 0.001$) (Table 2). The ROC curve (Figure 5) analysis of the preoperative T-staging of RC showed that the AUC was 0.794 in the AP image and 0.905 in the VP image. For AP images, the best cut-off of NIC_2 for distinguishing group D from group C was 3.346, with a sensitivity of 80.6%, a specificity of 77.3%, and an accuracy of 83.7%. The best cut-off of NIC_2 for the VP image was 4.105, with a sensitivity of 90.3%, specificity of 88.9%, and accuracy of 89.8%.

Interobserver agreement for dual-energy computed tomography spectral parameters

The ICC score of NIC_1 was 0.988 (95% CI: 0.982 to 0.992), and the ICC score of NIC_2 was 0.968 (95% CI: 0.955 to 0.978), which was considered an excellent consensus.

Conventional computed tomography preoperative T-staging

Using the pathological results as the gold standard, 20 cases of T1-2 were diagnosed via conventional CT imaging, of which 11 cases were correctly diagnosed, and 9 cases of T3-4a were misdiagnosed as T1-2. A total of 29 patients were diagnosed with T3-4a using conventional CT imaging, of which 22 patients were correctly diagnosed, and 7 patients with T1-2 were misdiagnosed with T3-4a (Table 3). Compared with the pathological staging, the accuracy of conventional CT in differentiating T3-4a from T1-2 was 67.3% (33/49).

Quantitative parameters of dual-energy computed tomography T-staging

According to NIC measured by DECT, 18 patients were diagnosed with T1-2, and 31 patients were diagnosed with T3-4a in the AP. Compared with the pathological results, 14 patients were correctly diagnosed with T1-2, 4 patients with T3-4a were misdiagnosed with T1-2, 27 patients were correctly diagnosed with T3-4a, and 4 patients with T1-2 were misdiagnosed with T3-4a (Table 3). The accuracy of DECT in differentiating T3-4a from T1-2 was 83.7% (41/49) in the AP.

In the VP, 17 patients were diagnosed with T1-2 and 32 patients with T3-4. Compared with the pathological results, 15 patients were correctly diagnosed with T1-2, 2 patients with T3-4 were misdiagnosed with T1-2, 29 patients were correctly diagnosed with T3-4, and 3 patients with T1-2 were misdiagnosed with T3-4 (Table 3). The accuracy of DECT in differentiating T3-4a from T1-2 was 89.8% (44/49) in the VP.

Discussion

The purpose of this study was to investigate the value of DECT in predicting LVI and evaluate the accuracy of preoperative RC T-staging. The postoperative histological results were used as the gold standard for grouping.

1. The tumors were divided into the LVI− (group A) and the LVI+ (group B). The LVI was defined as the presence of cancer cells in peritumoral lymphatic vessels and small non-muscularized blood vessels or
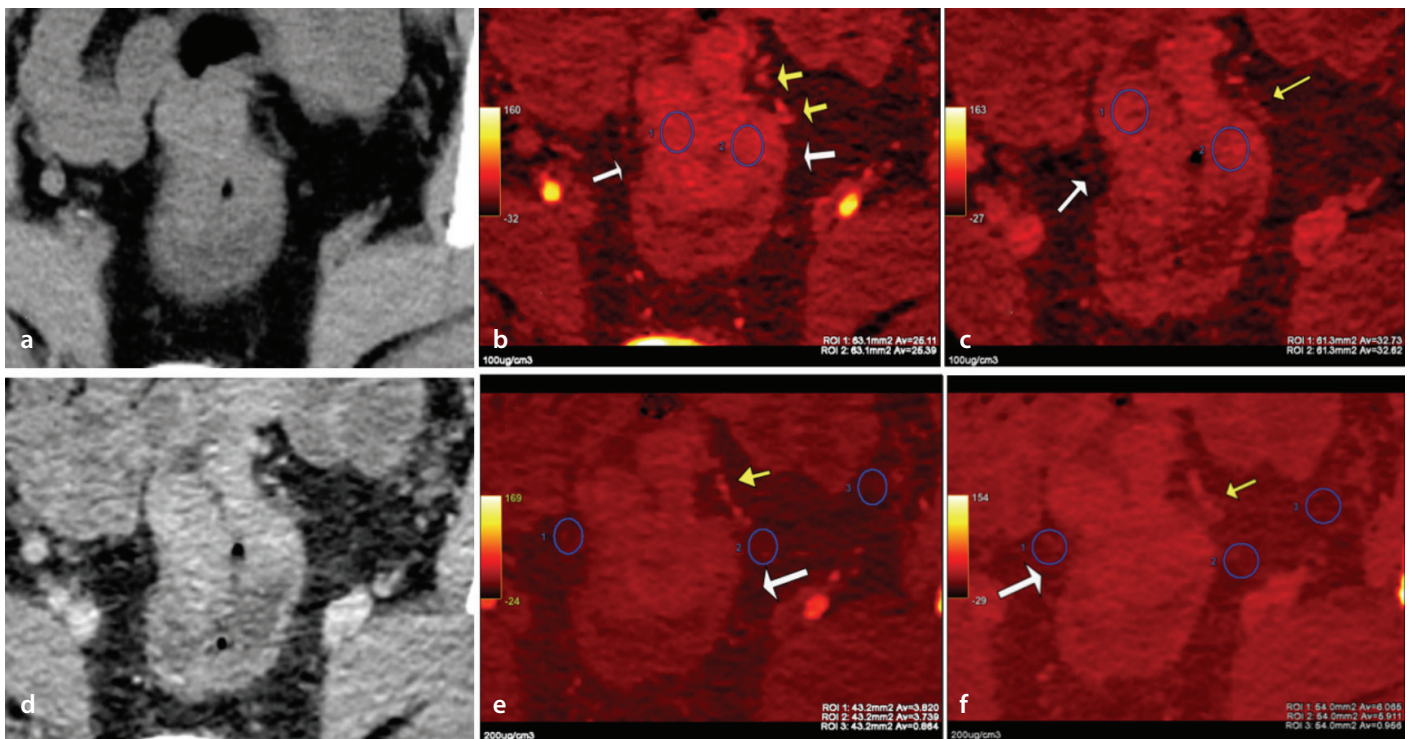
Figure 3. A 59-year-old man with lymphovascular invasion positive stage T3 rectal cancer. The white arrow denotes the thickening of the rectal wall, which was enhanced. The density of fat tissue around the tumor was more uniform. The local strip high-density shadow (denoted by the yellow arrow) is the vascular tissue. In **(a)** and **(b)**, the radiologist diagnosed the rectal tumor as clinical staging T2 with traditional computed tomography (CT) before surgery, but the pathological stage was pathological staging T3; **(c)** and **(d)** show the method of drawing regions of interest (ROIs) on the tumor tissue in the arterial phase (AP) and the venous phase (VP), respectively; **(e)** shows that the mean iodine concentration (IC) was 0.756 mg/mL in the perirectal fat tissue (ROI: 1.2) and 0.173 mg/mL in the fat tissue distant from the tumor in the AP (ROI: 3); **(f)** shows that the mean IC was 1.198 mg/mL in the fat tissue near the tumor (ROI: 1.2), and 0.191 mg/mL in the fat tissue distant from the tumor in the VP (ROI: 3). The dual-energy CT corrected the preoperative T-staging of the patient as non-T2.

both,[29] and was related to the dissemination of cancer cells.[30] Therefore, the NIC_2 of the adipose tissue around the tumor was not employed to evaluate LVI. Moreover, the study found that the difference in NIC_1 values between group A and group B was not statistically significant ($P > 0.05$) in the AP. However, in the VP, the NIC_1 was significantly higher in group B than in group A ($P < 0.001$). Setting 0.690 as the cut-off value, the accuracy of NIC_1 in LVI evaluation was 83.7%. There are several possible reasons for this result. First, LVI denoted a high invasiveness of cancer cells.[31] Second, the cancer cells of patients with LVI+ RC were relatively active, and the blood flow led to an increase in IC values. The study indicates that using the NIC value in the VP can distinguish between LVI− and LVI+. Further study, such as the use of a combination of different quantitative parameters, may improve the sensitivity and specificity of DECT technology.

2. The tumors were divided into two groups: group C (no serosa invasion, T1-2) and group D (serosa invasion, T3-4a). Conventional CT scanning was used for naked-eye observation of PAT density to determine whether the serosa had been infiltrated. Seven patients with stage T1-2 RC were overestimated as having stage T3 RC, and 9 patients with stage T3 RC were underestimated as having stage T1-2 RC, with an accuracy rate of 67.3%. These findings denoted the limitations of multi-slice spiral CT in the assessment of serosa invasion. The present study demonstrated that DECT was more valuable than conventional plain CT in diagnosing T3-4a RC. The NIC_2 in the PAT was significantly higher when the serosa had been invaded than when it had not been invaded. The ROC curve (Figure 5) analysis showed that the NIC_2 was more capable of distinguishing whether RC had invaded the surrounding adipose tissue in the VP than in the AP. The accuracy of NIC_2 in evaluating serous infiltration was 83.7% (AP) and 89.8% (VP) when setting the cut-off as 3.346 and 4.105 in the AP and VP, respectively, which was higher than the CT value. This study found that the NIC_1 of RC tissue was not related to the T-stage, which differed from the results of Li et al.[27] A possible reason for this result is that the invasiveness of the tumor was not only related to benignancy and malignancy, but also closely related to the accuracy of cancer detection time.[32]

Poorly differentiated RC may not break through the muscular layer in the early stage; in contrast, highly differentiated RC may invade the peripheral adipose space of the intestinal wall; and even distant metastasis will occur in the late stage. Whether the tumor had invaded the perirectal tissue or not was the criterion for judging stage T3 of RC. In summary, these observations suggest that DECT is an innovative and accurate imaging

Table 2. Demographic and clinical characteristics of the included participants

Characteristic	Group A (LVI−)	Group B (LVI+)	P value
Gender (n)			
Male	14	19	0.086
Female	11	5	
Age (year, mean ± SD)	59.7 ± 9.7	63.0 ± 8.7	0.237
Height (cm)	166.6 ± 6.2	169.6 ± 6.0	0.091
Weight (kg)	69.7 ± 8.3	74.4 ± 10.3	0.090
BMI (kg/m²)	25.0 ± 1.8	25.7 ± 2.3	0.262
Quantitative parameters			
NIC_1 AP	0.126 ± 0.003	0.127 ± 0.005	0.659
NIC_1 VP	0.669 ± 0.034	0.728 ± 0.031	<0.001**
	Group C (T1-2)	**Group D (T3-4a)**	**P value**
Gender (n)			
Male	10	23	0.187
Female	8	8	
Age (mean ± SD)	59.1 ± 7.6	62.6 ± 9.9	0.065
Height (cm)	166.1 ± 5.6	169.2 ± 6.4	0.092
Weight (kg)	68.1 ± 7.8	74.3 ± 9.8	0.029*
BMI (kg/m²)	24.6 ± 1.3	25.8 ± 2.3	0.022*
Stage (n)			
T1	2	0	
T2	16	0	
T3	0	28	
T4a	0	3	
Quantitative parameters			
NIC_1 AP	0.124 ± 0.003	0.127 ± 0.004	0.417
NIC_1 VP	0.690 ± 0.040	0.704 ± 0.044	0.342
NIC_2 AP	3.115 ± 0.581	4.034 ± 0.991	0.003*
NIC_2 VP	3.450 ± 0.980	5.481 ± 1.054	<0.001**

*$P < 0.05$, **$P < 0.001$; NIC_1, normalized iodine concentration of the initial tumor; NIC_2, normalized iodine concentration of the adipose tissue around the rectal tumor; AP, arterial phase; VP, venous phase; LVI+, lymphovascular invasion positive; LVI−, lymphovascular invasion negative; BMI, body mass index; SD, standard deviation.

Table 3. T-staging of rectal cancer using preoperative conventional computed tomography and dual-energy computed tomography compared with postoperative histology staging

Confusion matrix		Conventional CT		DECT arterial phase		DECT venous phase		Total
		T1-2	T3-4a	T1-2	T3-4a	T1-2	T3-4a	
Histologic stage	Group C (T1-2)	11	7[a]	14	4[a]	15	3[a]	18
	Group D (T3-4a)	9[b]	22	4[b]	27	2[b]	29	31

[a]Seven patients with RC in group C were misdiagnosed as group D using conventional CT; 5 of them were corrected using DECT in the arterial phase (AP), and 6 of them were corrected using DECT in the venous phase (VP). In addition, the conventional CT diagnosis of 2 patients in group C was correct, but the DECT was misdiagnosed as group D. [b]Nine patients with RC in group D were misdiagnosed as group C using conventional CT; 6 of them were corrected using DECT in the AP, and 8 of them were corrected using DECT in the VP. In addition, the conventional CT diagnosis of 1 patient in group D was correct, but the DECT led to a misdiagnosis as group C. CT, computed tomography; DECT, dual-energy computed tomography; RC, rectal cancer.
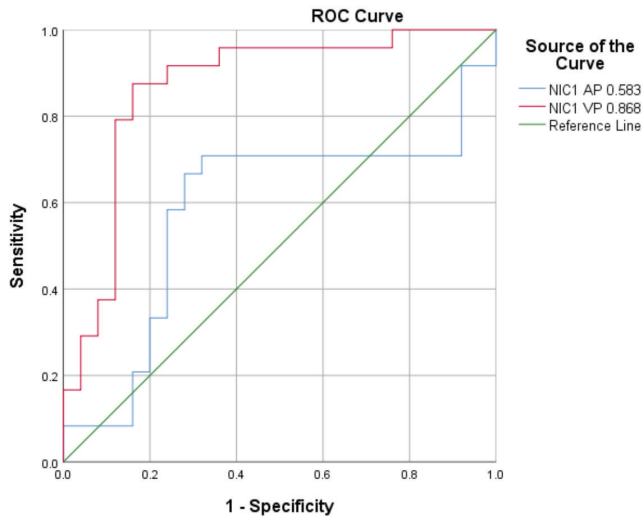
Figure 4. The receiver operating characteristic (ROC) curve showed the ability of preoperative normalized iodine concentration (NIC) values in the arterial phase (AP) and venous phase (VP) to predict the lymphovascular invasion (LVI) of rectal cancer. The ROC curves showed that the NIC_1 could predict the LVI of rectal cancer more accurately in the VP than in the AP. NIC_1, normalized iodine concentration of initial tumor; NIC_2, normalized iodine concentration of adipose tissue around rectal tumor.
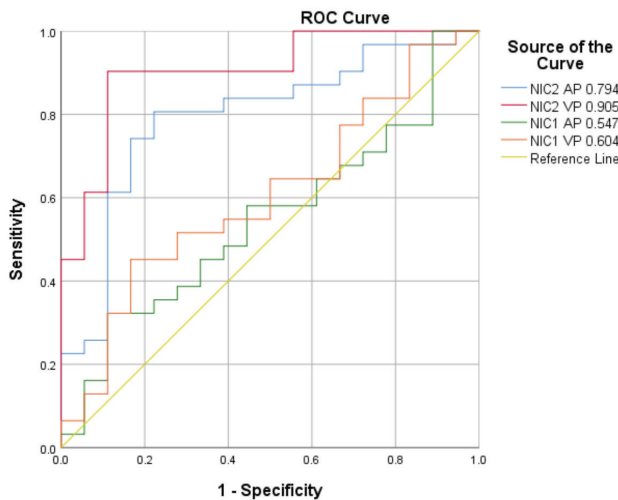
Figure 5. The receiver operating characteristic (ROC) curve showed the ability of preoperative normalized iodine concentration (NIC) values in the arterial phase (AP) and venous phase (VP) to predict the invasion of adipose tissue around the tumor; NIC_1 means the NIC of tumor tissue, and NIC_2 means the NIC of perirectal adipose tissue. The ROC curves showed that NIC_2 could predict the invasion of adipose tissue around the tumor more accurately in the VP than in the AP. NIC_1, normalized iodine concentration of initial tumor; NIC_2, normalized iodine concentration of adipose tissue around rectal tumor.

method for predicting LVI and improving the accuracy of preoperative RC T-staging.

Peng et al.[33] utilized the novel multiparametric imaging capabilities of DECT to predict very early distant metastasis (VEDM) following colorectal cancer surgery and noted that the venous enhancement fraction, the slope of the VP spectral curve (λ_{-V}) and the inverse of the VP-standardized IC ($1/NIC_{-V}$) presented significant discriminative abilities in predicting VEDM, with AUC values of 0.822, 0.738, and 0.713, respectively.

LVI is an early sign of lymph node metastasis and distant metastasis, which is the initial manifestation of lymph node metastasis and other types of organ metastasis;[34] the IC parameter of the tumor was applied in the prediction of LVI with an accuracy of 85.7%. Thus, it can guide clinical treatment and intervention in a relatively precise manner and in the early disease stage.

Jia et al.[35] compared the image quality of MRI and DECT virtual monochrome imaging techniques and assessed their accuracy

in T-staging, demonstrating that the overall diagnostic accuracy of dual-layer spectral CT and high-resolution MRI in T-staging was 65.67% and 71.64%, respectively, with no significant difference ($P > 0.05$). Qin et al.[36] investigated the optimal DECT parameter-AP λ_{HU} for differentiating between T3 and T4a stages of RC, with an overall accuracy of 76.9%. The present study on the T-staging of RC was conducted according to different clinical treatment modalities and focused on distinguishing the difference between T1-2 and T3-4a, which was more relevant to clinical needs than the other studies. The authors of the present study comprehensively considered the critical factors for the selection of clinical treatment options, including both tumor T-staging and LVI. This study set the research protocol according to clinical needs; the diversity and depth of this study contribute to a more comprehensive understanding of the application of DECT in oncology and may lead to the development of future diagnostic and therapeutic strategies. With the continuous development of DECT technology and the growing demand for a more accurate prediction of cancer staging and metastasis in clinical practice, more spectral parameters may be derived[33,37] and combined with clinical parameters[38] or even radiomics and artificial intelligence[37] to further improve the predictive potential. This provides new opportunities for follow-up studies.

This study has several limitations. First, the number of patients was limited, and the study used an experimental methodology. In the future, performing a larger-scale and more accurate patient selection study to affirm the results would be worthwhile. Second, the type of all involved tumors was rectal adenocarcinoma, and whether other types of rectal tumors can be staged using this method should be verified in future. Third, the placement of ROI was subjective and could only avoid obvious large blood vessels; however, interaction with some small vessels may have caused inflammation of connective tissue, increasing the false positive rate of the study. Fourth, this study did not measure other quantitative parameters of DECT. A combination of other DECT parameters could enhance the accuracy of predicting the pathological indicators of RC. Fifth, the present study did not measure the size of the primary tumor or locate the position of the tumor, especially the accurate location of the supra- or sub-peritoneal layer, which are critical factors for the RC treatment plan. Sixth, comparisons between DECT and

other imaging techniques, such as MRI and TRUS, were not performed. Finally, this study was a single-center study and did not involve samples from other medical centers. Therefore, a complicated analysis using DECT parameters will be performed in future studies.

In conclusion, this study found that the quantitative determination of NIC in tumors can predict LVI. Furthermore, NIC in PAT via DECT can accurately, sensitively, and specifically distinguish whether serosa invasion has occurred in RC. In addition, the study first utilized NIC to evaluate the invasion of PAT and effectively reduce the difference of individual factors among patients. The DECT quantitative IC measurement was a useful clinical tool for the preoperative prediction of pathological indicators of RC.

Conflict of interest disclosure

The authors declared no conflicts of interest.

References

1. Siegel RL, Miller KD, Fuchs HE, Jemal A. Cancer statistics, 2022. *CA Cancer J Clin*. 2022;72(1):7-33. [Crossref]

2. Burt JR, Waltz J, Ramirez A, et al. Predictive value of initial imaging and staging with long-term outcomes in young adults diagnosed with colorectal cancer. *Abdom Radiol (NY)*. 2021;46(3):909-918. [Crossref]

3. Amin MB, Greene FL, Edge SB, et al. The Eighth Edition AJCC Cancer Staging Manual: Continuing to build a bridge from a population-based to a more "personalized" approach to cancer staging. *CA Cancer J Clin*. 2017;67(2):93-99. [Crossref]

4. Foxtrot Collaborative Group. Feasibility of preoperative chemotherapy for locally advanced, operable colon cancer: the pilot phase of a randomised controlled trial. *Lancet Oncol*. 2012;13(11):1152-1160. [Crossref]

5. Monson JR, Weiser MR, Buie WD, et al. Practice parameters for the management of rectal cancer (revised). *Dis Colon Rectum*. 2013;56(5):535-550. [Crossref]

6. Nicum S, Midgley R, Kerr DJ. Colorectal cancer. *Acta Oncol*. 2003;42(4):263-275. [Crossref]

7. Le DT, Kim TW, Van Cutsem E, et al. Phase II open-label study of pembrolizumab in treatment-refractory, microsatellite instability-high/mismatch repair-deficient metastatic colorectal cancer: KEYNOTE-164. *J Clin Oncol*. 2020;38(1):11-19. [Crossref]

8. Opara CO, Khan FY, Kabiraj DG, Kauser H, Palakeel JJ, Ali M, Chaduvula P, Chhabra S, Lamsal Lamichhane S, Ramesh V, Mohammed L. The value of magnetic resonance imaging and endorectal ultrasound for the accurate preoperative T-staging of rectal cancer. *Cureus*. 2022;14(10):e30499. [Crossref]

9. Xia Q, Cheng W, Bi J, Ren AP, Chen X, Li T. Value of biplane transrectal ultrasonography plus micro-flow imaging in preoperative T staging and rectal cancer diagnosis in combination with CEA/CA199 and MRI. *BMC Cancer*. 2023;23(1):860. [Crossref]

10. Boot J, Gomez-Munoz F, Beets-Tan RGH. Imaging of rectal cancer. *Radiologe*. 2019;59(Suppl 1):46-50. [Crossref]

11. Beets-Tan RG, Beets GL. Rectal cancer: review with emphasis on MR imaging. *Radiology*. 2004;232(2):335-346. [Crossref]

12. Horvat N, Carlos Tavares Rocha C, Clemente Oliveira B, Petkovska I, Gollub MJ. MRI of Rectal Cancer: Tumor Staging, Imaging Techniques, and Management. *Radiographics*. 2019;39(2):367-387. [Crossref]

13. Napp AE, Enders J, Roehle R, et al. Analysis and prediction of claustrophobia during MR imaging with the claustrophobia questionnaire: an observational prospective 18-month single-center study of 6500 patients. *Radiology*. 2017;283(1):148-157. [Crossref]

14. Kijima S, Sasaki T, Nagata K, Utano K, Lefor AT, Sugimoto H. Preoperative evaluation of colorectal cancer using CT colonography, MRI, and PET/CT. *World J Gastroenterol*. 2014;20(45):16964-16975. [Crossref]

15. Xu JJ, Taudorf M, Ulriksen PS, et al. Gastrointestinal applications of iodine quantification using dual-energy CT: a systematic review. *Diagnostics (Basel)*. 2020;10(10):814. [Crossref]

16. Karcaaltincaba M, Karaosmanoglu D, Akata D, Sentürk S, Ozmen M, Alibek S. Dual energy virtual CT colonoscopy with dual source computed tomography: initial experience. *Rofo*. 2009;181(9):859-862. [Crossref]

17. Kang HJ, Kim SH, Bae JS, Jeon SK, Han JK. Can quantitative iodine parameters on DECT replace perfusion CT parameters in colorectal cancers? *Eur Radiol*. 2018;28(11):4775-4782. [Crossref]

18. Ascenti G, Mazziotti S, Lamberto S, et al. Dual-energy CT for detection of endoleaks after endovascular abdominal aneurysm repair: usefulness of colored iodine overlay. *AJR Am J Roentgenol*. 2011;196(6):1408-1414. [Crossref]

19. Chuang-Bo Y, Tai-Ping H, Hai-Feng D, et al. Quantitative assessment of the degree of differentiation in colon cancer with dual-energy spectral CT. *Abdom Radiol (NY)*. 2017;42(11):2591-2596. [Crossref]

20. Yang L, Shi G, Zhou T, Li Y, Li Y. Quantification of the iodine content of perigastric adipose tissue by dual-energy CT: a novel method for preoperative diagnosis of T4-stage gastric cancer. *PLoS One*. 2015;10(9):e0136871. [Crossref]

21. Kato T, Uehara K, Ishigaki S, et al. Clinical significance of dual-energy CT-derived iodine quantification in the diagnosis of metastatic LN in colorectal cancer. *Eur J Surg Oncol*. 2015;41(11):1464-1470. [Crossref]

22. Wang D, Zhuang Z, Wu S, et al. A dual-energy CT radiomics of the regional largest short-axis lymph node can improve the prediction of lymph node metastasis in patients with rectal cancer. *Front Oncol*. 2022;12:846840. [Crossref]

23. Altenbernd J, Forsting M, Lauenstein T, Wetter A. Improved image quality and detectability of hypovascular liver metastases on DECT with different adjusted window settings. *Rofo*. 2017;189(3):228-232. [Crossref]

24. Lenga L, Czwikla R, Wichmann JL, et al. Dual-energy CT in patients with colorectal cancer: Improved assessment of hypoattenuating liver metastases using noise-optimized virtual monoenergetic imaging. *Eur J Radiol*. 2018;106:184-191. [Crossref]

25. Ratajczak P, Serafin Z, Sławińska A, Słupski M, Leszczyński W. Improved imaging of colorectal liver metastases using single-source, fast kVp-switching, dual-energy CT: preliminary results. *Pol J Radiol*. 2018;83:e643-e649. [Crossref]

26. Al-Najami I, Lahaye MJ, Beets-Tan RGH, Baatrup G. Dual-energy CT can detect malignant lymph nodes in rectal cancer. *Eur J Radiol*. 2017;90:81-88. [Crossref]

27. Li Y, Li X, Ren X, Ye Z. Assessment of the aggressiveness of rectal cancer using quantitative parameters derived from dual-energy computed tomography. *Clin Imaging*. 2020;68:136-142. [Crossref]

28. Zhou X, Yi Y, Liu Z, et al. Radiomics-based preoperative prediction of lymph node status following neoadjuvant therapy in locally advanced rectal cancer. *Front Oncol*. 2020;10:604. [Crossref]

29. Lim SB, Yu CS, Jang SJ, Kim TW, Kim JH, Kim JC. Prognostic significance of lymphovascular invasion in sporadic colorectal cancer. *Dis Colon Rectum*. 2010;53(4):377-384. [Crossref]

30. Stacker SA, Achen MG, Jussila L, Baldwin ME, Alitalo K. Lymphangiogenesis and cancer metastasis. *Nat Rev Cancer*. 2002;2(8):573-583. [Crossref]

31. Zhang Y, He K, Guo Y, et al. A novel multimodal radiomics model for preoperative prediction of lymphovascular invasion in rectal cancer. *Front Oncol*. 2020;10:457. [Crossref]

32. Wu ZJ, Hippe DS, Zamora DA, et al. Accuracy of dual-energy computed tomography

techniques for fat quantification in comparison with magnetic resonance proton density fat fraction and single-energy computed tomography in an anthropomorphic phantom environment. *J Comput Assist Tomogr*. 2021;45(6):877-887. [Crossref]

33. Peng W, Wan L, Zhao R, et al. Novel biomarkers based on dual-energy computed tomography for risk stratification of very early distant metastasis in colorectal cancer after surgery. *Quant Imaging Med Surg*. 2024;14(1):618-632. [Crossref]

34. Wang X, Cao Y, Ding M, et al. Oncological and prognostic impact of lymphovascular invasion in Colorectal Cancer patients. *Int J Med Sci*. 2021;18(7):1721-1729. [Crossref]

35. Jia Z, Guo L, Yuan W, et al. Performance of dual-layer spectrum CT virtual monoenergetic images to assess early rectal adenocarcinoma T-stage: comparison with MR. *Insights Imaging*. 2024;15(1):11. [Crossref]

36. Qin M, Liu M, Huang R, et al. Preoperative T-staging of colorectal cancer by dual-energy computed tomography: a retrospective study. *Currt Med Imaging*. 2024;20:1-7. [Crossref]

37. Chen M, Jiang Y, Zhou X, Wu D, Xie Q. Dual-energy computed tomography in detecting and predicting lymph node metastasis in malignant tumor patients: a comprehensive review. *Diagnostics (Basel)*. 2024;14(4):377. [Crossref]

38. Sato K, Morohashi H, Tsushima F, et al. Dual energy CT is useful for the prediction of mesenteric and lateral pelvic lymph node metastasis in rectal cancer. *Mol Clin Oncol*. 2019;10(6):625-630. [Crossref]

Computed tomography-based contrast features for distinguishing extra-gastrointestinal stromal tumors from intra-abdominal fibromatosis

Lijing Zhang[1]
Yongbo Li[1]
Xinxin Luo[1]
Deqi Li[1]
Linlin Yin[2]
Jiayue Li[3]
Li Zhang[1]

[1]Cangzhou Central Hospital, Department of Radiology, Cangzhou, China

[2]Cangzhou Central Hospital, Department of Laboratory, Cangzhou, China

[3]Cangzhou Renmin Hospital, Department of Radiology, Cangzhou, China

PURPOSE

This study aims to define the computed tomography (CT) criteria that distinguish extra-gastrointestinal stromal tumors (eGISTs) from intra-abdominal fibromatosis (IAF).

METHODS

Retrospective analysis was conducted on CT images obtained from 31 pathologically confirmed cases, including 17 cases of eGISTs and 14 of IAF. Various parameters [e.g., lesion location, contour characteristics, border delineation, enhancement patterns, presence of intralesional necrosis, vessels, air, fat, and hemorrhage, the long diameter (LD), LD/short diameter (SD) ratio, and volume (LD × SD × height diameter)] were meticulously evaluated. In addition, the degree of enhancement during arterial and portal venous phases and the lesion-to-aorta CT attenuation ratio during both phases were quantified. Statistical analysis was performed using Fisher's exact test, the Student's t-test, and the receiver operating characteristic curve to identify significant CT criteria. Sensitivity and specificity assessments were conducted for single and combined CT criteria.

RESULTS

Significant differentiators between eGISTs and IAF include non-mesenteric localization, irregular contour, well-defined borders, heterogeneous enhancement, presence of intralesional necrosis and vessels, and absence of intralesional fat, with LD exceeding 9.6 cm, an LD/SD ratio >1.22, and volume surpassing 603.3 cm^3 ($P < 0.05$). A combination of seven or more of these criteria yielded a specificity of 100%.

CONCLUSION

Ten distinct CT criteria have been identified to distinguish eGISTs from IAF, notably encompassing non-mesenteric localization, irregular contour, well-defined borders, heterogeneous enhancement, presence of intralesional necrosis and vessels, absence of intralesional fat, LD >9.6 cm, an LD/SD ratio >1.22, and volume surpassing 603.3 cm^3.

CLINICAL SIGNIFICANCE

The current findings establish CT criteria to distinguish eGISTs from IAF in a clinical setting.

KEYWORDS

Diagnosis, computed tomography criteria, non-mesenteric localization, intralesional necrosis, heterogeneous enhancement

Corresponding author: Li Zhang

E-mail: 18031792007@163.com

Extra-gastrointestinal stromal tumors (eGISTs) are a rare type of gastrointestinal stromal tumor (GIST). They occur outside the gastrointestinal tract and are not associated with the intestinal wall.[1] Approximately 80% (26/32) of eGISTs are intra-abdominal, primarily in the mesentery and omentum, with some detected in the retroperitoneum.[2] A pioneering report in 1999, documenting 26 cases originating from the omentum and mesentery, highlighted their clinicopathological and immunohistochemical similarities to GISTs, leading to their classification as eGISTs.[3] Most reported eGISTs present as large lesions (>10 cm) or exhibit high mitotic activity (>10/50 high-power field), placing them in a high-risk category with an unfavorable prognosis.[2,4,5] Diagnosis typically involves preoperative identification using

radiological imaging modalities such as contrast-enhanced computed tomography (CT) or magnetic resonance imaging, followed by confirmation through postoperative histopathological and immunohistochemical analyses. Histologically, eGISTs are characterized by spindle, epithelioid, and/or pleomorphic cell morphology and are associated with positive immunostaining for CD117 (c-kit receptor) and CD34 biomarkers.[5]

A subtype of aggressive fibromatosis (AF), intra-abdominal fibromatosis (IAF) has the lowest incidence rate, representing a rare benign monoclonal fibroblastic proliferation that primarily originates from the mesentery or retroperitoneum within the abdomen.[6] Despite its benign classification, IAF is notable for its high recurrence rate post-surgical resection, with no propensity for metastasis.[7] Although IAF and eGISTs are distinct entities, they are prone to misidentification.[7-10] As a widely employed non-invasive medical imaging modality, CT plays a pivotal role in examining abdominal structures to detect lesions.[7] Consequently, differentiating between eGISTs and IAF on CT images is crucial because of their distinct prognoses and treatment modalities. However, accurate diagnosis remains challenging for personalized treatment and prognosis evaluation given the rarity of both intra-abdominal eGISTs and IAF.

Considering the scarcity of literature clarifying the distinctive CT features and clinical attributes of both eGISTs and IAF, we conducted a retrospective analysis of clinical data and CT images from 31 patients observed at a single center. Among these patients, 17 were diagnosed with intra-abdominal eGISTs and 14 with IAF. We aimed to provide a comprehensive synthesis of their clinical profiles and CT characteristics, thereby enhancing our understanding of their inherent behaviors. By identifying unique features on contrast-enhanced CT scans, we sought to mitigate the risk of inappropriate or subpar treatment strategies.

Methods

Patient characteristics

This retrospective study received approval from the Institutional Review Board at Cangzhou Central Hospital (decision no: #2021-266-02, date: 09.05.2021), which waived the requirement for informed consent. We screened 224 patients with GISTs who underwent surgical procedures at our hospital between July 2013 and December 2021. Among them, 19 cases were confirmed as eGISTs (Figure 1). Additionally, all 15 cases of IAF included in our institutional database were compiled from routine clinical practice during the same period. The inclusion criteria were as follows: surgical excision of the tumor, complete clinicopathological data, and preoperative contrast-enhanced CT scans of good image quality. The exclusion criteria were irresectable tumors (one case caused by multiple focal lesions for eGISTs and one case caused by liver metastasis) or the absence of preoperative contrast-enhanced CT scans (one case with only plain CT for IAF). Ultimately, 31 patients (17 with intra-abdominal eGISTs and 14 with IAF) were included in this study. Clinical data, including age, sex, presence of abdominal mass, and abdominal pain, were carefully reviewed.

Computed tomography image acquisition

All 31 patients underwent comprehensive abdominal and/or pelvic contrast-enhanced CT examinations covering the entire tumor, using a 320-detector row scanner (Toshiba Medical Systems, Otawara, Japan) at our institution. The CT imaging parameters were standardized as follows: tube voltage was set at 120 kV, tube current ranged from 100 to 450 mA, rotation time was 0.5 s, detector collimation was set at 64×0.625 mm, matrix size was 512×512, pitch ratio was 0.6–1.2:1, and slice thickness was 5 mm. For dynamic contrast-enhanced CT imaging, an intravenous non-ionic contrast agent (1 mL/kg) was administered using an automatic power injector at a rate of 3.5 mL/s. Images of the arterial and portal venous phases were acquired at 25–30 and 60 s post-injection, respectively. It is important to note that delayed-phase imaging was omitted in this retrospective study due to its absence in routine abdominal CT protocols. The reconstruction of CT images from both phases was performed with a slice thickness of 2 mm. Additionally, coronal and sagittal multiplanar reformatted (MPR) images were generated to ascertain the lesions' origin relative to the gastrointestinal tract wall.

Image analysis

The contrast-enhanced CT images were independently reviewed by two seasoned abdominal radiologists (with 11 and 9 years of experience, respectively), following a randomized sequence using a picture archiving and communication system. Both readers conducted evaluations without any knowledge of the clinical findings or pathological results. Qualitative analysis of the CT criteria included evaluating lesion location, contours, borders, enhancement pattern, and the presence of intralesional necrosis, vessels, air, fat, and hemorrhage. Lesion locations were validated using MPR CT images and surgical records and were stratified as either mesenteric or non-mesenteric regions. Lesion contours were categorized as round, ovoid, lobulated, or irregular, with round and ovoid shapes classified as regular and lobulated and irregular shapes as irregular. Lesion

---

Main points

- The computed tomography (CT) images of patients with extra-gastrointestinal stromal tumors (eGISTs) and intra-abdominal fibromatosis (IAF) have crucial differences.

- The 10 discerning CT criteria to distinguish eGISTs from IAF are non-mesenteric localization, irregular contour, well-defined borders, heterogeneous enhancement, presence of intralesional necrosis and vessels, absence of intralesional fat, long diameter (LD) >9.6 cm, an LD/ short diameter ratio >1.22, and volume exceeding 603.3 cm³.

- These 10 CT criteria can be utilized in clinical practice to distinguish eGISTs from IAF before surgery.
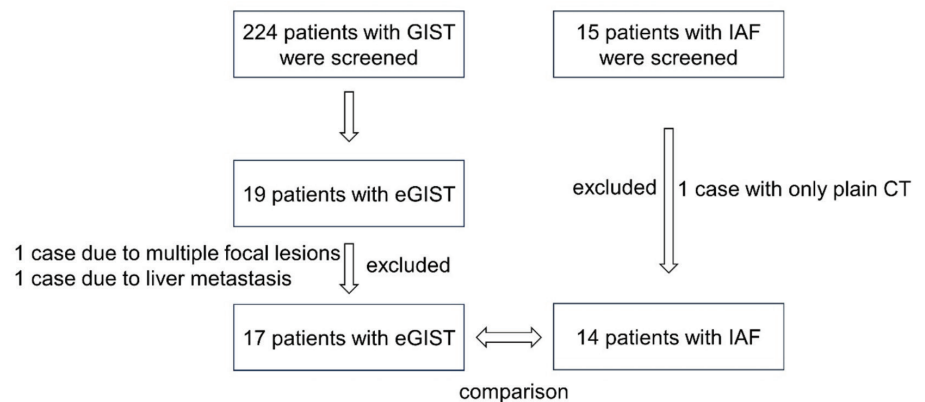
Figure 1. Study flowchart. GIST, gastrointestinal stromal tumor; eGIST, extra-gastrointestinal stromal tumors; CT, computed tomography; IAF, intra-abdominal fibromatosis.

borders were delineated as ill-defined or well-defined in relation to the adjacent soft tissue. Enhancement patterns, characterized as homogeneous or heterogeneous, were assessed during the portal venous phase. Homogeneous enhancement was identified by a difference of <10 HU between the most strongly and weakly enhanced regions, whereas >10 HU signified heterogeneous enhancement. Intralesional low attenuation, suggesting necrosis, was designated by a CT attenuation value of <20 HU on the portal venous phase. Intralesional vessel identification was based on feeding vessels observed in MPR images during the arterial phase. Intralesional low attenuation, indicating gas, was identified by a CT attenuation value similar to the gas density in the stomach or intestine during the arterial–venous phase. Similarly, intralesional low attenuation, suggesting fat, was delineated by a CT attenuation value similar to subcutaneous fat during the arterial–venous phase. Intralesional hyperattenuation, indicating hemorrhage, was recognized by a CT attenuation value of >70 HU, persisting across both arterial and portal venous phases. In cases of disagreement, the radiologists engaged in a discussion to achieve consensus. The quantitative analysis included assessing the long diameter (LD), LD/short diameter (SD) ratio, volume [LD × SD × height diameter (HD)], degree of enhancement (DE) during both arterial and portal venous phases, and lesion/aorta (L/A) CT attenuation ratio. Consensus was reached by averaging measurements from the two readers to determine the final result for qualitative data analysis.

Statistical analysis

All statistical analyses were conducted using the SPSS statistical package (version 26.0, SPSS, Chicago, IL, USA). The required sample size was determined using PS software (version 3.0.12). A P value of <0.05 was considered statistically significant. Fisher's exact test was used to compare qualitative data between the eGIST and IAF groups, and the Student's t-test was utilized for comparing quantitative data. After statistical analysis, sensitivity and specificity values were calculated for each CT criterion that showed a significant difference between eGISTs and IAF. Sensitivity and specificity values were computed for the LD, LD/SD ratio, and volume (LD × SD × HD) to generate receiver operating characteristic (ROC) curves. These curves helped determine the optimal cut-off points for distinguishing IAF from eGISTs. The optimal cut-off point was identified as the

value that maximized the sum of sensitivity and specificity.

Results

Clinical characteristics

This study involved a cohort of 31 patients, 17 individuals diagnosed with intra-abdominal eGISTs and 14 with IAF, to outline distinctive clinical characteristics and CT features observed on contrast-enhanced CT images. The cohort consisted of 10 men and 7 women in the eGISTs group, with a mean age of 60.94 ± 2.90 years, and 6 men and 8 women in the IAF group, with a mean age of 54.29 ± 4.03 years. The clinical characteristics of the patients with are summarized in Table 1. The analysis revealed no significant differences in age, sex, or the presence of abdominal pain and abdominal mass between the two tumor types (all $P > 0.05$).

Qualitative analysis of computed tomography features

The qualitative analysis of CT features comparing eGISTs and IAF is summarized in Table 2. The distribution of tumor location differed significantly between the two tumor types ($P = 0.021$). Furthermore, eGISTs were more commonly found in the non-mesenteric region, whereas IAF occurred more frequently in the mesenteric region. In terms of lesion contour, most eGISTs exhibited a lobulated or irregular shape, whereas most IAF cases presented with an ovoid or round contour ($P = 0.001$). Moreover, eGISTs tended to have well-defined borders, whereas most IAF lesions demonstrated ill-defined borders ($P = 0.001$). The enhancement pattern significantly differentiated between eGISTs and IAF ($P < 0.001$), with heterogeneous enhancement observed more frequently in eGISTs. In addition, eGISTs exhibited a higher tendency toward intralesional necrosis compared with IAF ($P < 0.001$), whereas IAF

lesions showed less frequent intralesional necrosis. Regarding intralesional vessels, eGISTs displayed a higher tendency, whereas IAF had less frequent intralesional vessels ($P < 0.001$). By contrast, IAF demonstrated a greater tendency toward intralesional fat, whereas eGISTs had less frequent intralesional fat ($P = 0.004$). However, intralesional hemorrhage and intralesional air did not significantly differentiate between eGISTs and IAF. Representative images illustrating these qualitative CT features are presented in Figures 2a-c. These findings emphasize the utility of qualitative CT analysis in distinguishing between eGISTs and IAF, providing valuable insights for accurate diagnosis and treatment planning.

Quantitative analysis of computed tomography features

Table 2 provides a summary of the quantitative analysis of CT features comparing eGISTs and IAF. eGISTs exhibited a larger LD and volume compared with IAF ($P < 0.001$) and displayed a higher LD/SD ratio than IAF ($P = 0.003$). However, the DE during the arterial phase and venous phase and the L/A ratio (arterial phase, portal venous phase) did not reveal significant differences between eGISTs and IAF in this study. Representative images are presented in Figure 2a-c.

Based on the ROC analysis results, the LD had a cut-off value of 9.6 cm for the differential diagnosis of eGISTs and IAF, achieving a sensitivity of 82.4%, a specificity of 82.9%, and an area under the ROC curve of 0.912. Similarly, the volume had a cut-off value that resulted in 94.1% sensitivity, 85.7% specificity, and an area under the ROC curve of 0.903. Additionally, the LD/SD ratio had a cut-off value that led to 82.4% sensitivity, 71.4% specificity, and an area under the ROC curve of 0.826. The LD exhibited similar performance compared with volume and LD/SD ratio (DeLong test, $P < 0.05$); the ROC curves are displayed in Figure 3.

Table 1. Clinical characteristics analysis results for eGISTs versus IAF

Clinical characteristics		eGISTs (n = 17)	IAF (n = 14)	P value
Age (mean ± SD)		60.94 ± 2.90	54.29 ± 4.03	0.181[b]
Sex	Man	10 (58.8%)	6 (42.9%)	0.479[a]
	Woman	7 (41.2%)	8 (57.1%)	
Abdominal mass	Present	8 (47.1%)	6 (42.9%)	1.000[a]
	Absent	9 (52.1%)	8 (57.1%)	
Abdominal pain	Present	7 (41.2%)	11 (78.6%)	0.067[a]
	Absent	10 (58.8%)	3 (21.4%)	

P < 0.05 indicates that the difference is statistically significant. [a]: Between eGISTs and IAF compared with Fisher's exact test. [b]: Between eGISTs and IAF compared with the Student's t-test. SD, standard deviation; eGISTs, extra-gastrointestinal stromal tumors; IAF, intra-abdominal fibromatosis.

Sensitivity and specificity values for computed tomography diagnosis

Table 3 displays the sensitivity and specificity values of each significant CT criterion for distinguishing eGISTs from IAF. The combination of any 5 of these 10 criteria resulted in a sensitivity of 100% (17 of 17) and a specificity of 92.9% (13 of 14). When employing any seven or more of these criteria, a specificity of 100% was achieved, as indicated in Table 4.

Discussion

eGISTs constitute a rare subset of malignant mesenchymal tumors that share clinicopathological and immunohistochemical features with GISTs.[3] Although reports suggest eGISTs can appear in various anatomical sites such as the neck,[11] liver,[12,13] and prostate,[14] the abdomen remains the predominant location,[15] often involving the mesentery, omentum, and retroperitoneum.[16] It is widely acknowledged that eGISTs demonstrate aggressive behavior and have an unfavorable prognosis.[2,5,15] Despite being distinct entities, eGISTs and IAF are frequently confused.[7-10] The differentiation between these entities carries significant clinical implications, as the diagnostic criteria for malignancy in eGISTs do not apply to IAF. Unlike eGISTs, which are prone to metastasis and exhibit aggressive behavior, IAF represents benign tumors with no metastatic potential, although they can be locally aggressive. Therefore, clarifying the distinction between eGISTs and IAF is crucial for appropriate treatment planning and prognostic assessment.

For both eGISTs and IAF, abdominal pain and a palpable mass are the most common clinical symptoms.[6,17] In this study, we observed no significant differences in the presence of abdominal pain, abdominal mass, age, or sex between the tumor types ($P > 0.05$). However, we encountered two intriguing cases of IAF where a palpable mass was distinctly observed in the initial plain CT scan, subsequently shifting to another location within the abdomen in the contrast-enhanced CT scan. This observation suggests that the mass exhibited mobility along the mesentery, originating from the mesenteric region.

Our study identified 10 CT criteria as statistically significant indicators for distinguishing between eGISTs and IAF: non-mesenteric location, irregular contour, well-defined border, heterogeneous enhancement, presence of intralesional necrosis and vessels, absence of intralesional fat, LD >9.6 cm, volume >603.3 cm^3, and an LD/SD ratio >1.22. Moreover, combining positive CT criteria improved the diagnostic performance for distinguishing eGISTs from IAF, thereby facilitating accurate diagnosis and appropriate treatment selection.

In our study, eGISTs exhibited a significantly larger LD and volume compared with IAF ($P < 0.001$), as well as a higher LD/SD ratio than IAF ($P = 0.003$). These findings are consistent with previous literature, which suggests that patients with eGISTs often remain asymptomatic until the lesion progresses to a palpable mass.[18] Given the demands of our routine workflow and heavy reporting load, measuring the LD in axial CT images proves to be a practical and cost-effective approach. Our analysis identified a 9.6-cm cut-off value for the LD in axial images as an effective discriminator between eGISTs and IAF, yielding a sensitivity of 82.4%, a specificity of 82.9%, and an area under the ROC curve of 0.912. Notably, this performance was comparable with that of volume and LD/SD ratio ($P > 0.05$ for the DeLong test). In contrast to previous reports that encompassed all GIST cases, our study focused specifically on eGISTs because of their fundamental differences from GISTs.[16] Interestingly, in our analysis, both DE (arterial and venous phases) and L/A ra-
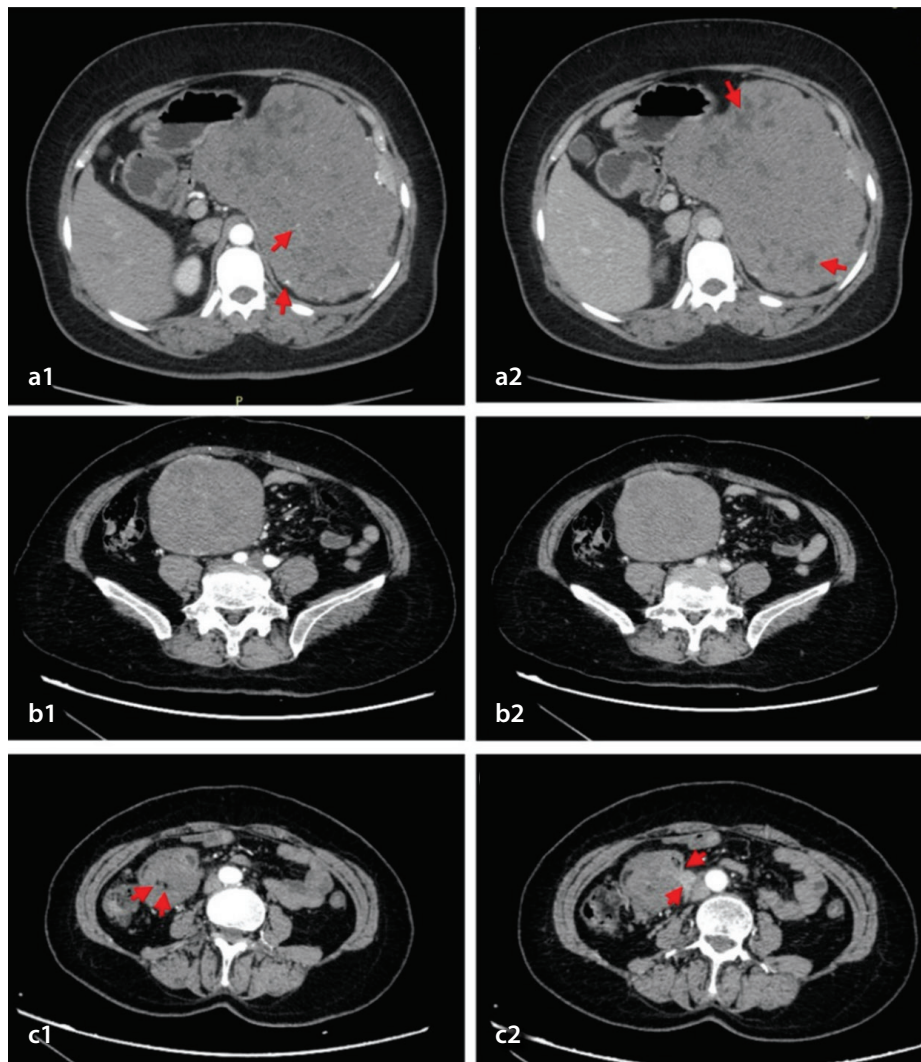
Figure 2. (a) A 50-year-old woman with a 17.1-cm-long diameter extra-gastrointestinal stromal tumor in the space between the stomach and spleen. **(a1)** Axial arterial phase computed tomography (CT) image revealing an irregular mass with a well-defined border and intralesional vessels (arrows). **(a2)** Portal venous phase axial contrast-enhanced CT images revealing a heterogeneously enhanced mass with intralesional necrosis (arrows). **(b)** A 57-year-old woman with a 9.4-cm-long diameter intra-abdominal fibromatosis (IAF) arising from transverse colon mesentery. **(b1)** Axial arterial phase CT image revealing a regular mass with a well-defined border without intralesional vessels. **(b2)** Portal venous phase axial contrast-enhanced CT images revealing a homogeneously enhanced mass without intralesional necrosis. **(c)** A 53-year-old woman with a 5.3-cm-long diameter IAF arising from duodenal mesentery. **(c1)** Axial arterial phase CT image revealing punctate intralesional fat (arrows). **(c2)** Axial arterial phase CT image displaying an involved descending duodenal segment (arrow).

tio (arterial and portal venous phases) for eGISTs and IAF did not exhibit significant differences, diverging from previous findings. We observed that eGISTs tended to have a larger average volume (1,840.68 cm^3) compared with IAF (459.74 cm^3), potentially resulting in the dispersion of intra-tumor vessels and subsequent reduction in CT attenuation values. However, significant factors for distinguishing eGISTs from IAF included the enhancement pattern and the presence of intralesional necrosis and vessels. Our results indicated that eGISTs predominantly exhibited heterogeneous enhancement (94.1% of cases), intralesional necrosis (94.1% of cases), and intralesional vessels (94.1% of cases) on contrast CT. These findings align with previous reports, underscoring the characteristic features of eGISTs, including heterogeneous contrast enhancement, prominent intralesional vessels, and inner low attenuation changes attributed to necrosis, hemorrhage, or cystic degeneration, which contrast with the CT features observed in IAF in our study.

In this study, IAF was more frequently located in the mesenteric region (92.9%, 13/14) compared with eGISTs (52.9%, 9/17), a finding consistent with prior research.[6] Intra-abdominal AF, a rare and locally aggressive mass, originates from benign fibrous tissue proliferation[7] and represents the most common primary tumor of the mesentery.[19] In our series, 70.6% (12/17) of eGIST cases exhibited lobulated or irregular contours, whereas 92.9% (13/14) of IAF cases demonstrated ovoid or round shapes, deviating from typical pathological descriptions of eGISTs.[17] Intra-abdominal AF is characterized by a highly collagenous stroma, often homogenous and with soft-tissue attenuation.[20] In our study, 50% (7/14) of IAF cases displayed ill-defined margins on contrast CT, indicative of its locally aggressive growth pattern, a distinct CT feature from eGISTs. We propose that the ill-defined mass represents an aggressive phenotype for IAF, necessitating pathological confirmation in future studies. Another distinguishing CT feature is the presence of intralesional fat, observed in 42.9% (6/14) of IAF cases compared with 0% (0/17) of eGIST cases, which is consistent with previous findings.[9] As IAF gradually enlarges, it infiltrates mesenteric fat, signaling a locally aggressive growth pattern distinct from eGISTs. This unique growth pattern underscores the differential diagnosis between IAF and eGISTs and highlights the importance of considering both clinical and radiological features in making an accurate diagnosis.

The treatment approach for both eGISTs and IAF involves multidisciplinary team management, which is paramount for optimizing patient outcomes.[7] The standard treatment

Figure 3. Receiver operating characteristic (ROC) curve. Graph displaying four ROC curves for long diameter (LD), volume, and LD/short diameter (SD) ratio to differentiate eGISTs from IAF. The areas under the ROC curve are 0.816 (LD), 0.861 (volume), and 0.888 (LD/SD ratio). eGISTs, extra-gastrointestinal stromal tumors, IAF, intra-abdominal fibromatosis.

Table 2. Qualitative and quantitative CT image analyses results for eGISTs versus IAF

CT criteria		eGISTs (n = 17)	IAF (n = 14)	P value
Location	Mesenteric region	9 (52.9%)	13 (92.9%)	0.021[a]
	Non-mesenteric region	8 (47.1%)	1 (7.1%)	
Contour	Regular	5 (29.4%)	13 (92.9%)	0.001[a]
	Irregular	12 (70.6%)	1 (7.1%)	
Border	Well-defined	17 (100%)	7 (50%)	0.001[a]
	Ill-defined	0 (0%)	7 (50%)	
Enhancement pattern	Homogeneous	1 (5.9%)	12 (85.7%)	<0.001[a]
	Heterogeneous	16 (94.1%)	2 (14.3%)	
Intralesional necrosis	Present	16 (94.1%)	0 (0%)	<0.001[a]
	Absent	1 (5.9%)	14 (100%)	
Intralesional vessels	Present	16	4	<0.001[a]
	Absent	1	10	
Intralesional air	Present	2 (11.8%)	2 (14.3%)	1.000[a]
	Absent	15 (88.2%)	12 (85.7%)	
Intralesional fat	Present	0 (0%)	6 (42.9%)	0.004[a]
	Absent	17 (100%)	8 (57.1%)	
Intralesional hemorrhage	Present	2 (11.8%)	0 (0%)	0.488[a]
	Absent	15 (88.2%)	14 (100%)	
LD		13.50 ± 1.01	6.74 ± 0.82	<0.001[b]
LD/SD ratio		1.56 ± 0.11	1.17 ± 0.03	0.003[b]
Volume (LD × SD × HD)		1840.68 ± 264.46	459.74 ± 196.43	<0.001[b]
DE (AP, HU)		49.10 ± 3.24	48.37 ± 2.19	0.860[b]
DE (PP, HU)		65.67 ± 4.46	61.77 ± 2.65	0.482[b]
L/A ratio (AP)		0.17 ± 0.01	0.17 ± 0.01	0.856[b]
L/A ratio (PP)		0.46 ± 0.02	0.45 ± 0.03	0.780[b]

Data are presented as means ± standard deviations. [a]: Between eGISTs and IAF compared with Fisher's exact test. [b]: Between eGISTs and IAF compared with the Student's t-test. CT, computed tomography; eGISTs, extra-gastrointestinal stromal tumors; IAF, intra-abdominal fibromatosis; LD, long diameter; SD, short diameter; HD, height diameter; DE, degree of enhancement; L/A ratio, lesion/aorta CT attenuation ratio; AP, arterial phase; PP, portal venous phase.

Table 3. PPV, NPV, sensitivity, and specificity values of each significant CT criteria for differentiating eGISTs from IAF

CT criteria	PPV	NPV	Sensitivity (%)	Specificity (%)
Non-mesenteric region	88.9 (8/9)	59.1 (13/22)	47.1 (8/17)	92.9 (13/14)
Irregular contour	92.3 (12/13)	72.2 (13/18)	70.6 (12/17)	92.9 (13/14)
Well-defined border	70.8 (17/24)	100 (7/7)	100 (17/17)	50 (7/14)
Heterogeneous enhancement	88.9 (16/18)	92.3 (12/13)	94.1 (16/17)	85.7 (12/14)
Intralesional necrosis presence	100 (16/16)	93.3 (14/15)	94.1 (16/17)	100 (14/14)
Intralesional vessels presence	80 (16/20)	90.9 (10/11)	94.1 (16/17)	71.4 (10/14)
Intralesional fat absence	68 (17/25)	100 (6/6)	100 (17/17)	42.9 (6/14)
LD >9.6 cm	93.3 (14/15)	81.3 (13/16)	82.4 (14/17)	92.9 (13/14)
Volume >603.3 cm^3	88.9 (16/18)	92.3 (12/13)	94.1 (16/17)	85.7 (12/14)
LD/SD ratio >1.22	77.8 (14/18)	76.9 (10/13)	82.4 (14/17)	71.4 (10/14)

PPV, positive predictive value; NPV, negative predictive value; CT, computed tomography; eGISTs, extra-gastrointestinal stromal tumors; IAF, intra-abdominal fibromatosis; LD, long diameter; SD, short diameter.

Table 4. Combined CT criteria in differentiating eGISTs from IAF

CT criteria	eGISTs (n = 17)	IAF (n = 14)	Sensitivity (%)	Specificity (%)
≥1	17	12	100	14.3
≥2	17	9	100	35.7
≥3	17	4	100	71.4
≥4	17	2	100	85.7
≥5	17	1	100	92.9
≥6	16	1	94.1	92.9
≥7	16	0	94.1	100
≥8	15	0	88.2	100
≥9	14	0	82.3	100
≥10	10	0	58.8	100

CT, computed tomography; eGISTs, extra-gastrointestinal stromal tumors; IAF, intra-abdominal fibromatosis.

for GIST involves radical surgical resection, often combined with adjuvant imatinib therapy for cases classified as medium or high risk according to National Institutes of Health criteria.[21] Unfortunately, eGISTs have an unfavorable prognosis despite treatment strategies mirroring those of GISTs. Common treatment modalities for managing IAF include surgery alone or in combination with radiotherapy.[6] In certain cases, a multidisciplinary approach encompassing surgery, chemotherapy, and radiation therapy is advocated.[22]

Several limitations were encountered in our study. First, due to the low incidence rates of both eGISTs and IAF, our sample size was limited. Future research with larger sample sizes is warranted to provide a more comprehensive understanding of the biological behavior of both tumor entities. Second, immunohistochemical markers are crucial in delineating the distinct characteristics of eGISTs and IAF. Further investigation and correlation studies between these two tumors are warranted. Third, the routine abdominal CT protocols

utilized in our study did not include delayed phase imaging to minimize unnecessary radiation exposure.

In conclusion, this study identifies effective CT criteria to differentiate eGISTs from IAF. A total of 10 main parameters were determined, and the 3 CT parameters with the highest diagnostic accuracy were LD >9.6 cm, heterogeneous enhancement, and well-defined borders.

Conflict of interest disclosure

The authors declared no conflicts of interest.

References

1. Ambrosio M, Testa AC, Moro F, et al. Imaging in gynecological disease (19): clinical and ultrasound features of extragastrointestinal stromal tumors (eGIST). *Ultrasound Obstet Gynecol*. 2020;56(5):749-758. [Crossref]

2. Reith JD, Goldblum JR, Lyles RH, Weiss SW. Extragastrointestinal (soft tissue) stromal tumors: an analysis of 48 cases with emphasis on histologic predictors of outcome. *Mod Pathol*. 2000;13(5):577-585. [CrossRef]

3. Miettinen M, Monihan JM, Sarlomo-Rikala M, et al. Gastrointestinal stromal tumors/smooth muscle tumors (GISTs) primary in the omentum and mesentery: clinicopathologic and immunohistochemical study of 26 cases. *Am J Surg Pathol*. 1999;23(9):1109-1118. [CrossRef]

4. Acar T, Efe D, Okuş A, Öcal İ, Harman M. A rare solid tumor of the retroperitoneum with venous extension and lung metastasis: extra-gastrointestinal stromal tumor. *Turk J Gastroenterol*. 2015;26(4):358-359. [CrossRef]

5. Hu W, Zheng C, Li R, et al. Retroperitoneal extragastrointestinal stromal tumors have a poor survival outcome: a multicenter observational study. *Cancer Manag Res*. 2020;12(10):10491-10504. [CrossRef]

6. Xiao J, Mao J, Li B. Clinical characteristics and treatment of intra-abdominal aggressive fibromatosis: a retrospective study of 16 patients. *Front Med (Lausanne)*. 2020;7(1):2. [CrossRef]

7. Zhu H, Chen H, Zhang S, Peng W. Intra-abdominal fibromatosis: differentiation from gastrointestinal stromal tumour based on biphasic contrast-enhanced CT findings. *Clin Radiol*. 2013;68(11):1133-1139. [CrossRef]

8. Kim JH, Ryu MH, Park YS, Kim HJ, Park H, Kang YK. Intra-abdominal desmoid tumors mimicking gastrointestinal stromal tumors - 8 cases: a case report. *World J Gastroenterol*. 2019;25(16):2010-2018. [CrossRef]

9. Yantiss RK, Spiro IJ, Compton CC, Rosenberg AE. Gastrointestinal stromal tumor versus intra-abdominal fibromatosis of the bowel wall: a clinically important differential diagnosis. *Am J Surg Pathol*. 2000;24(7):947-957. [CrossRef]

10. Rodriguez JA, Guarda LA, Rosai J. Mesenteric fibromatosis with involvement of the gastrointestinal tract. A GIST simulator: a study of 25 cases. *Am J Clin Pathol*. 2004;121(1):93-98. [CrossRef]

11. Zhang Y, Zhang A, Song L, Li X, Zhang W. Primary extragastrointestinal stromal tumor

on FDG PET/CT. *Clin Nucl Med*. 2018;43(9):705-706. [CrossRef]

12. Joyon N, Dumortier J, Aline-Fardin A, et al. Gastrointestinal stromal tumors (GIST) presenting in the liver: diagnostic, prognostic and therapeutic issues. *Clin Res Hepatol Gastroenterol*. 2018;42(2):23-28. [CrossRef]

13. Qian XH, Yan YC, Gao BQ, Wang WL. Prevalence, diagnosis, and treatment of primary hepatic gastrointestinal stromal tumors. *World J Gastroenterol*. 2020;26(40):6195-6206. [CrossRef]

14. Li L, Hu ZQ, Yang CG, et al. Current knowledge of primary prostatic extra-gastrointestinal stromal tumor: a case report and review of the literature. *J Int Med Res*. 2021;49(5):3000605211013172. [CrossRef]

15. Uzunoglu H, Tosun Y. Primary extra gastrointestinal stromal tumors of the abdomen. *North Clin Istanb*. 2021;8(5):464-471. [CrossRef]

16. Yi JH, Park BB, Kang JH, et al. Retrospective analysis of extra-gastrointestinal stromal tumors. *World J Gastroenterol*. 2015;21(6):1845-1850. [CrossRef]

17. Zhu J, Yang Z, Tang G, Wang Z. Extragastrointestinal stromal tumors: computed tomography and magnetic resonance imaging findings. *Oncol Lett*. 2015;9(1):201-208. [CrossRef]

18. Iqbal N, Sharma A, Iqbal N. Clinicopathological and treatment analysis of 13 extragastrointestinal stromal tumors of mesentery and retroperitoneum. *Ann Gastroenterol*. 2015;28(1):105-108. [CrossRef]

19. Levy AD, Rimola J, Mehrotra AK, Sobin LH. From the archives of the AFIP: benign fibrous tumors and tumorlike lesions of the mesentery: radiologic-pathologic correlation. *Radiographics*. 2006;26(1):245-264. [CrossRef]

20. Einstein DM, Tagliabue JR, Desai RK. Abdominal desmoids: CT findings in 25 patients. *AJR Am J Roentgenol*. 1991;157(2):275-279. [CrossRef]

21. Gold JS, Gönen M, Gutiérrez A, et al. Development and validation of a prognostic nomogram for recurrence-free survival after complete surgical resection of localised primary gastrointestinal stromal tumour: a retrospective analysis. *Lancet Oncol*. 2009;10(11):1045-1052. [CrossRef]

22. Rampone B, Pedrazzani C, Marrelli D, Pinto E, Roviello F. Updates on abdominal desmoid tumors. *World J Gastroenterol*. 2007;13(45):5985-5988. [CrossRef]

ARTIFICIAL INTELLIGENCE AND INFORMATICS

COMMENTARY

Reporting checklists as compulsory supplements to artificial intelligence manuscript submissions

 Michail E. Klontzas[1,2,3]

[1]Department of Radiology, School of Medicine, University of Crete, Heraklion, Greece

[2]Computational Biomedicine Laboratory, Institute of Computer Science, Foundation for Research and Technology (FORTH), Heraklion, Greece

[3]Division of Radiology, Department for Clinical Science Intervention and Technology (CLINTEC), Karolinska Institutet, Stockholm, Sweden

Research on artificial intelligence (AI) for radiology is rapidly expanding, with an exponentially increasing number of AI submissions being accepted for publication in radiology journals. The quality of these publications significantly depends on the information included in the text or accompanying it (e.g., code and data), which allows for the accurate evaluation of the proposed work and the reproduction of the results. Reporting checklists can be instrumental in assisting authors in including all required information; they also help reviewers to comprehensively evaluate the manuscripts before publication. Journals in medical imaging have an available arsenal of reporting checklists and guidelines that can be used to ensure a minimum standard of reporting quality in any published paper.[1]

The work by Koçak et al.[2] indicated that, unfortunately, only a small minority of journals encourage authors to use these reporting guidelines. In their well-designed analysis, the authors clearly point out that only 5 out of 98 journals encouraged using reporting guidelines, and only 3 out of these 5 mandated uploading the filled checklist together with the manuscript files.

Journals were considered to encourage the use of a guideline if they mentioned the name of the guideline, had a direct reference to it, or explicitly recommended its use, adherence, or referral, even if the authors were not asked to upload a completed version of the guideline with the manuscript. The authors looked for a series of AI-specific guidelines, including the Checklist for AI in Medical Imaging (CLAIM),[3,4] the Consolidated Standards of Reporting Trials-AI (CONSORT-AI),[5] the Fairness, Universality, Traceability, Usability, Robustness, and Explainability-AI (FUTURE-AI) checklist,[6] the CheckList for EvaluAtion of Radiomics Research (CLEAR),[7] and the Transparent Reporting of a multivariable prediction model for Individual Prognosis Or Diagnosis-AI (TRIPOD+AI).[8]

Some guidelines cover any AI application (e.g., CLAIM, FUTURE-AI, minimum information about clinical AI modeling, and TRIPOD+AI), and others are intended for specific AI applications related to clinical trials (e.g., CONSORT-AI and Standard Protocol Items: Recommendations for Interventional Trials-AI) and radiomics (e.g., CLEAR guidelines and the METhodological RadiomiCs Score (METRICS).[9] Despite the wide variety of purpose-specific checklists and their importance in increasing manuscript quality, most journals do not encourage authors to use them.

Even though the use of checklists is not encouraged by all journals, the peer review process aims to filter out low-quality or flawed articles and provide reviewer suggestions to enhance the quality of published research. Reviewers should use checklists while evaluating AI papers and should require authors to use and include, as a supplementary file, the completed checklist document, indicating how the manuscript covers each point of the checklist. According to Koçak et al.[2] only 6% of journals included instructions for reviewers that encouraged the use of AI-related checklists. This does not necessarily mean that individual reviewers neglect the use of these checklists; however, journals should prompt their reviewers to ensure that the points of the relevant checklist are discussed in the manuscript. In cases where a manuscript fails to include important information, the reason for this should be mentioned in the text or the accompanying checklist document.

Corresponding author: Michail E. Klontzas

E-mail: miklontzas@gmail.com, miklontzas@uoc.gr

In addition, caution needs to be exercised when authors provide self-filled checklists. This has become evident in another publication by Kocak et al.[10] Their study shows that almost 60% of publications asserting the adherence to CLAIM did not provide a completed checklist. Moreover, most papers that provided a filled-out checklist contained errors. Therefore, the proper use of these checklists should be assessed to avoid misuse or misinterpretation of individual points. Common mistakes include the omission of explanations in case one of the requirements is not fulfilled or false claims that all requirements have been fulfilled.

Appropriate use of checklists should ideally be evaluated at multiple stages (Figure 1). At the pre-submission stage, journals should mandate the selection of a checklist related to the topic of the paper (e.g., medical imaging, clinical trials, and generic AI applications), and authors should prepare the manuscript in accordance with the requirements of the checklist. Subsequently, authors should submit a completed, detailed version of the checklist at the submission stage. The submission of this completed version should be obligatory to proceed to the review stage. During the review stage, reviewers should ensure the inclusion of all necessary information outlined in the checklist, and any missing data or discrepancies should be addressed in subsequent review rounds.

In conclusion, reporting checklists can enhance the quality of manuscripts, ease the work of reviewers, and increase the reproducibility of published work. Nonetheless, their proper use requires: (i) adoption by journals as a mandatory requirement for submission, (ii) author adherence to checklist points, (iii) meticulous evaluation by reviewers to ensure that all checklist requirements are fulfilled prior to submission. This pipeline will ensure a smooth review process, without surprises to authors, leading to high quality publications.
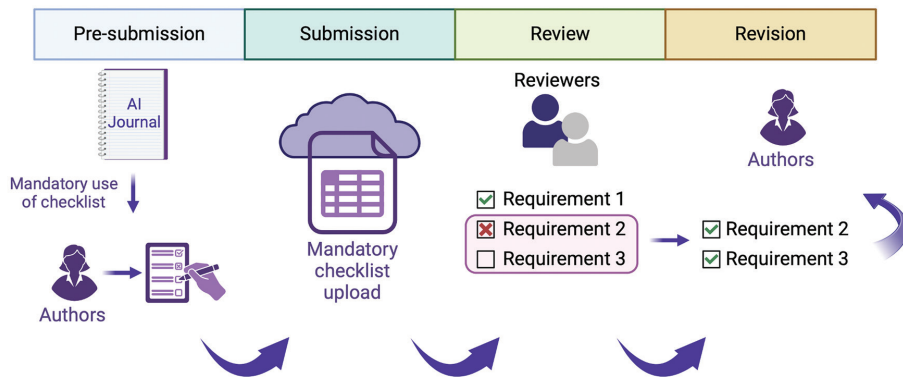
Figure 1. Proposed use of reporting checklists throughout the manuscript review and publication process. AI, artificial intelligence.

Conflict of interest disclosure

The author declared no conflicts of interest.

References

1. Klontzas ME, Gatti AA, Tejani AS, Kahn CE Jr. AI Reporting Guidelines: how to select the best one for your research. *Radiol Artif Intell*. 2023;5(3):e230055. [CrossRef]

2. Koçak B, Keleş A, Köse F. Meta-research on reporting guidelines for artificial intelligence: are authors and reviewers encouraged enough in radiology, nuclear medicine, and medical imaging journals? *Diagn Interv Radiol*. 2024. [CrossRef]

3. Tejani AS, Klontzas ME, Gatti AA, et al. Updating the Checklist for Artificial Intelligence in Medical Imaging (CLAIM) for reporting AI research. *Nat Mach Intell*. 2023;5(9):950-951. [CrossRef]

4. Tejani AS, Klontzas ME, Gatti AA, et al. Checklist for Artificial Intelligence in Medical Imaging (CLAIM): 2024 Update. *Radiol Artif Intell*. 2024:e240300. [CrossRef]

5. Liu X, Cruz Rivera S, Moher D, Calvert MJ, Denniston AK; SPIRIT-AI and CONSORT-AI Working Group. Reporting guidelines for clinical trial reports for interventions involving artificial intelligence: the CONSORT-AI extension. *Nat Med*. 2020;26(9):1364-1374. [CrossRef]

6. Lekadir K, Osuala R, Gallin C, et al. FUTURE-AI: Guiding Principles and Consensus Recommendations for Trustworthy Artificial Intelligence in Medical Imaging. *arXiv [cs.CV]*. 2021. [CrossRef]

7. Kocak B, Baessler B, Bakas S, et al. CheckList for EvaluAtion of Radiomics research (CLEAR): a step-by-step reporting guideline for authors and reviewers endorsed by ESR and EuSoMII. *Insights Imaging*. 2023;14(1):75. [CrossRef]

8. Collins GS, Moons KGM, Dhiman P, et al. TRIPOD+AI statement: updated guidance for reporting clinical prediction models that use regression or machine learning methods. *BMJ*. 2024;385:e078378. Erratum in: *BMJ*. 2024;385:q902. [CrossRef]

9. Kocak B, Akinci D'Antonoli T, Mercaldo N, et al. METhodological RadiomICs Score (METRICS): a quality scoring tool for radiomics research endorsed by EuSoMII. *Insights Imaging*. 2024;15(1):8. [CrossRef]

10. Kocak B, Keles A, Akinci D'Antonoli T. Self-reporting with checklists in artificial intelligence research on medical imaging: a systematic review based on citations of CLAIM. *Eur Radiol*. 2024;34(4):2805-2815. [CrossRef]

Evaluation of guided reporting: quality and reading time of automatically generated radiology report in breast magnetic resonance imaging using a dedicated software solution

 Martin H. Maurer[1]
 Daniel Lorenz[2]
 Maximilian Clemens Otterbach[1]
 Igor Toker[2]
 Alexander Huppertz[2,3]

[1]Universitätsinstitut für Diagnostische und Interventionelle Radiologie, Klinikum Oldenburg AöR, Department of Diagnostic and Interventional Radiology, Oldenburg, Germany

[2]Neo Q Quality in Imaging GmbH, Berlin, Germany

[3]University of Potsdam, Center of Sports Medicine, University Outpatient Clinic, Potsdam, Germany

PURPOSE

Unstructured, free-text dictation (FT), the current standard in breast magnetic resonance imaging (MRI) reporting, is considered time-consuming and prone to error. The purpose of this study is to assess the usability and performance of a novel, software-based guided reporting (GR) strategy in breast MRI.

METHODS

Eighty examinations previously evaluated for a clinical indication (e.g., mass and focus/non-mass enhancement) with FT were reevaluated by three specialized radiologists using GR. Each radiologist had a different number of cases (R1, n = 24; R2, n = 20; R3, n = 36). Usability was assessed by subjective feedback, and quality was assessed by comparing the completeness of automatically generated GR reports with that of their FT counterparts. Errors in GR were categorized and analyzed for debugging with a final software version. Combined reading and reporting times and learning curves were analyzed.

RESULTS

Usability was rated high by all readers. No non-sense, omission/commission, or translational errors were detected with the GR method. Spelling and grammar errors were observed in 3/80 patient reports (3.8%) with GR (exclusively in the discussion section) and in 36/80 patient reports (45%) with FT. Between FT and GR, 41 patient reports revealed no content differences, 33 revealed minor differences, and 6 revealed major differences that resulted in changes in treatment. The errors in all patient reports with major content differences were categorized as content omission errors caused by improper software operation (n = 2) or by missing content in software v. 0.8 displayable with v. 1.7 (n = 4). The mean combined reading and reporting time was 576 s (standard deviation: 327 s; min: 155 s; max: 1,517 s). The mean times for each reader were 485, 557, and 754 s, and the respective learning curves evaluated by regression models revealed statistically significant slopes (P = 0.002; P = 0.0002; P < 0.0001). Overall times were shorter compared with external references that used FT. The mean combined reading and reporting time of MRI examinations using FT was 1,043 s and decreased by 44.8% with GR.

CONCLUSION

GR allows for complete reporting with minimized error rates and reduced combined reading and reporting times. The streamlining of the process (evidenced by lower reading times) for the readers in this study proves that GR can be learned quickly. Reducing reporting errors leads to fewer therapeutic faults and lawsuits against radiologists. It is known that delays in radiology reporting hinder early treatment and lead to poorer patient outcomes.

CLINICAL SIGNIFICANCE

While the number of scans and images per examination is continuously rising, staff shortages create a bottleneck in radiology departments. The IT-based GR method can be a major boon, improving radiologist efficiency, report quality, and the quality of simultaneously generated data.

KEYWORDS

Breast magnetic resonance imaging, clinical informatics, quality, radiology report, radiology workflow, software-based reporting, structured reporting, workflows, human interactions

Corresponding author: Martin H. Maurer

E-mail: mhm.maurer@gmx.net

R adiology reporting has not changed significantly since the beginning of the 20th century. By general consensus, radiologists should communicate unambiguously with referring physicians according to the six C's of communication: clarity, correctness, concision, completeness, consistency, and a high level of confidence.[1] Few linguistic guidelines exist for the structure of radiological findings.[2,3] Most radiology reports are crafted by free-text dictation (FT), whereby individual styles of speech may not meet the expectations of a referring physician.[4,5] In addition, a high percentage of reports contain errors,[6] with the amount of radiology errors recently assessed as 3%–5%.[7] Errors can occur before, during, or after the reporting period, may cause direct, indirect, permanent, or temporary harm to patients,[8] and can be classified into 12 subgroups.[9] Contrary to the low incidence of "poor communication-related error" reported by Kim and Mansfield[9] 2014, Brady[7] concludes that poorly written or incoherent reports are a significant source of potential harm to patients.

Additionally, the time it takes radiologists to generate reports[10,11] creates a bottleneck. Waiting for imaging and its accompanying report affects length of hospital stay and the quality of patient care. In a Canadian evaluation, each additional hour spent waiting for magnetic resonance imaging (MRI) increased acute length of hospital stay by 1.2 h.[12] Modern MRI scanners produce increasingly detailed images in ever shorter times, often making image acquisition faster than analysis and reporting.

Modern radiology reporting systems are expected to reduce error rates, increase comprehensibility, and shorten report generation times. Templates and structured reporting (SR) methods do not meet all these requirements and have been applied in clinical routine only to a limited extent.[13-15] Guided reporting (GR) is a new strategy for radiology reporting. To the best of our knowledge, this study is the first to investigate and evaluate the performance of GR in breast MRI. Our purpose is to overcome the known disadvantages of SR, which include greater time investment and effort, inconsistencies in interpretation, and poor user experiences (UX).[16]

Methods

Study design

The Ethics Committee of Carl von Ossietzky University in Oldenburg, Germany approved the protocol for this retrospective study (project no: 2023-217, date: 20.11.2023). This is an experimental retrospective study conducted to assess the usability, report quality, and reading time of GR software (RadioReport®) in breast MRI (Figure 1). The study used a pre-market version (v. 0.8) of the MR mammography module to validate the usability of the software and identify further areas for improvement needed for the finalization of a market version. Eighty MRI examinations covering the full spectrum of clinical breast MRI findings [mass (n = 57), focus or non-focus enhancement (NME) (n = 8), and exclusion of a mass (n = 15)] were selected from the department of radiology at University Hospital Oldenburg (Oldenburg, Germany). Broad consent for retrospective evaluation is routinely obtained at the study hospital. These cases had been reported more than 8 weeks prior using FT and were reevaluated by the same radiologist.

The GR evaluation in this study was completed by three radiologists specialized in breast diagnostics with 16, 13, and 11 years of experience in breast MRI. The three radiologists completed a 90-min online training session on how to use the software. Application support was available by phone. Readers were instructed to begin the image reading and reporting processes simultaneously. Reader 1 had 24 cases, Reader 2 had 20 cases, and Reader 3 had 36 cases. The number of orthographic errors in the FT and GR reports was evaluated.

Guided reporting software

The pre-market v. 0.8 of the GR software was used as a stand-alone web tool. The software automatically generates radiological reports based on decoded complex radiological decision trees. A comprehensive query system (Figure 2) guides the user through the reporting process, and a dedicated module for breast MRI is available. The program includes mandatory fields, predefined paths for information input, and plausibility checks, thus guaranteeing completeness in

---

Main points

- The software-based guided reporting (GR) strategy is a novel technology for structured reporting in medicine.

- GR allows for complete radiology reporting with minimized error rates and reduced reading times.

- The shortening of reporting times is key for successful implementation of GR into the clinical workflow.

- Differences in content between GR and unstructured, free-text dictation are not caused by limitations of the software itself but by insufficient, user-dependent operation of the software. Thus, the introduction of this disruptive technology requires intensive training and adjustment to the process.

- The great potential of structured datasets will open doors for the future of radiology with respect to big data analysis, automatic, real-time International Statistical Classification of Diseases and Related Health Problems 10 coding, and the efficient integration of artificial intelligence.
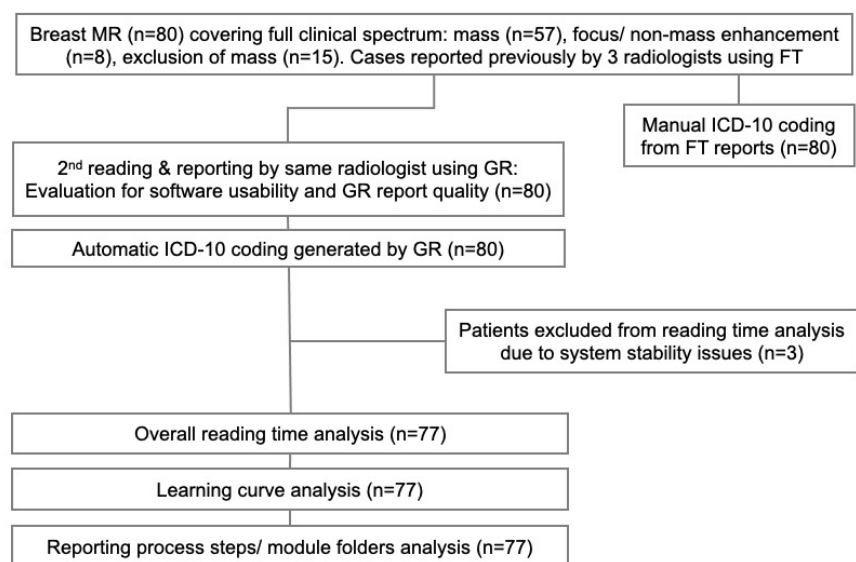
Figure 1. Study flowchart. FT, free-text dictation; GR, guided reporting; ICD-10, International Statistical Classification of Diseases and Related Health Problems.

reporting. The radiologist is guided through 10 folders (patient/indication, anamnesis, technique, anatomy, background parenchymal enhancement, findings, lymph nodes/organs, bones, summary, and report). A key difference between GR and SR is the former's anatomy-based approach: every body region and modality is covered in a single module [e.g., thorax computed tomography (CT), abdomen MRI, breast MRI]. Each module covers all relevant pathologies for its specific anatomical region (e.g., tumors, inflammation, post-surgery pathologies), and a combination of different pathologies can be easily reported (rather than having to combine different templates for a single body region).[17]

Instead of having to offer and continuously update hundreds of templates, almost all MRI, CT, and breast imaging indications can be reported using 23 modules.

Each folder (e.g., "axillary lymphadenopathy" in the lymph nodes/organs folder; Figure 2b) opens with a mouse click and displays further items on the next level of depth (e.g., right/left). Each sub-item consists of several subordinated levels (e.g., level I/II/III). Detailed descriptions can be added (e.g., max. short-axis diameter in mm). Moreover, the software features information files. By selecting different items and sub-items, the software concomitantly generates semantic sentences from predefined and approved text phrases stored in its database.

Additional information can be entered manually in the Discussion section (using speech recognition or keyboard entry) to enable a hybrid approach,[18] wherein GR with fully machine-readable data and individual information entries are combined to enhance flexibility and acceptance. The commercial and European conformity (CE)-certified version (v. 1.7) of the software includes an add-on of bullet points in the Impression section (i.e., to highlight the exclusion of suspected pathologies) (Figure 3).

With a final click, a fully automated text structured in standard compliant sections (e.g., patient data, indication, anamnesis, technique, findings, impression, and recommendations; Figures 3, 4) is generated. Diagnoses are automatically coded according to the 10th revision of the International Statistical Classification of Diseases and Related Health Problems (ICD-10).[19]

For the second phase of the study, v. 1.7 of the software was used. Here, technical and medical feedback was implemented, and the complexity of the breast MRI module was increased from 33,756 lines of code in v. 0.8 to 57,213 in v. 1.7 (front- and backend). Five hundred-thirteen logic lines were used in v. 1.7.

Evaluation

Usability and guided reporting quality

Usability was evaluated based on feedback from every reader along three parameters: intuitive operation, the practicability of simultaneous image analysis and reporting, and user confidence in the automatically generated report compared with FT (assessed on a 4-point scale: very good, good, medium, and poor). Readers were asked if they experienced a change in confidence while operating the software and if they would specifically recommend GR for certain subgroups.

Report quality was evaluated by comparing the completeness of the automatically generated GR product with its FT counterpart, as well as noting any differences between the two strategies. This evaluation was performed by consensus by two senior radiologists who organized the reports into three scores. A report received a score of A if there were no differences in content between FT and GR, a score of B if there were only minor differences in content that did not result in differences in treatment, and a score of C if there were major differences in content that resulted in differences in treat-
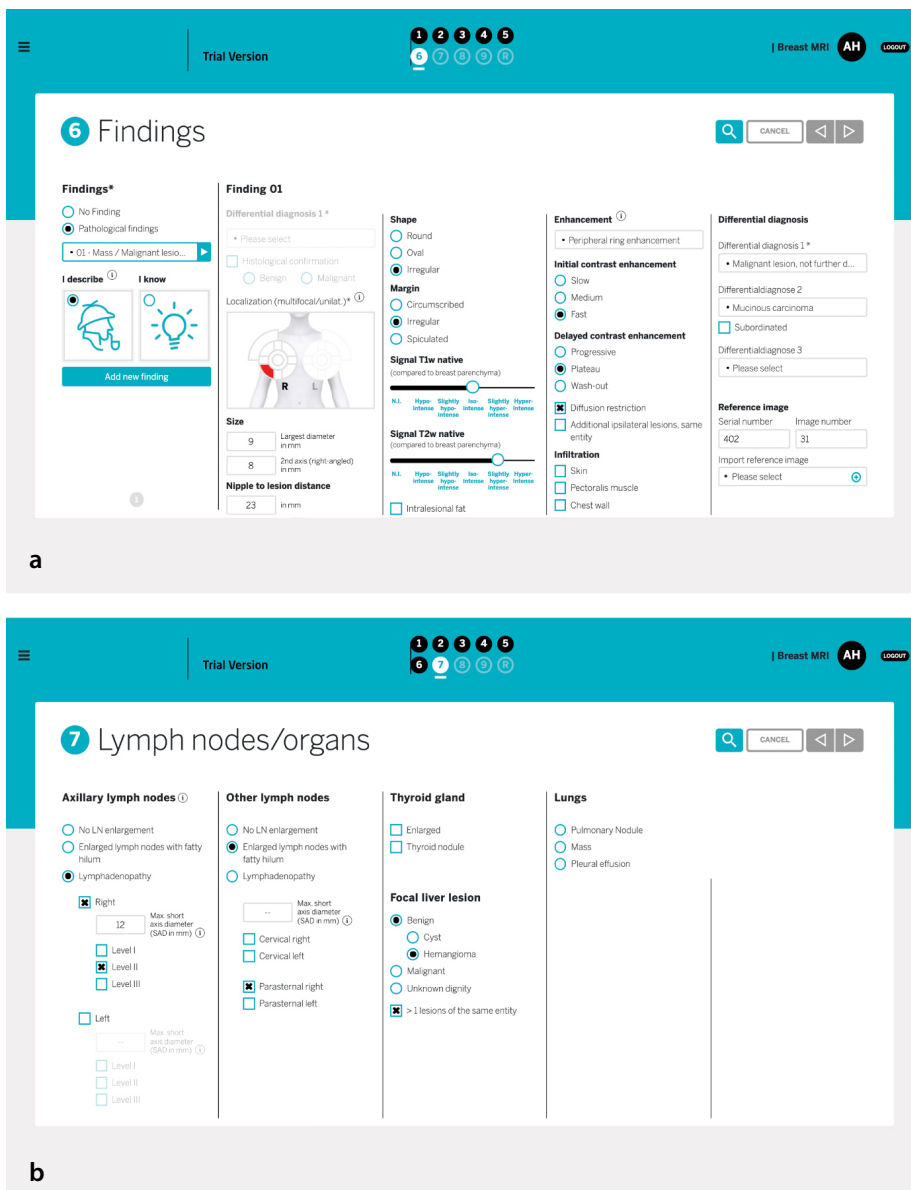
Figure 2. Screenshots of guided reporting software graphic interface. **(a)** Folder 6, featuring the reporting of a finding (a mass in the right lower outer quadrant). The complex query system, with selections on different levels and entry for embedded reference images is depicted. **(b)** Folder 7, featuring the reporting of right axillary lymphadenopathy. The query system, with selections on four levels (score, site, size, and level) is depicted.

ment. Entries in the Discussion section were not included in this evaluation.

Content omission errors (COEs) in GR, v. 0.8, for patient reports receiving a score of B or C were further evaluated and categorized as follows: category 1 errors were caused by insufficient operation of the software; category 2 errors were caused by missing content in the v. 0.8 software displayable with v. 1.7; and category 3 errors were caused by missing content in the v. 0.8 software that was not displayable with v. 1.7. Errors in reporting were further categorized according to a modified classification system proposed by Hawkins et al.[6] as follows: (a) non-sense; (b) spelling/grammar; (c) omission/commission; and (d) translation (Table 1).

Reporting process and time

Reading time (s) was defined as the overall combined image reading time and report creation time, evaluated based on the implemented tracking option. Individual use of information files was tracked automatically. Overall reading times were compared between different readers as well as different lesions. The learning curve for reading time over the study period was evaluated for every reader using a multiple regression analysis. The reporting process was additionally analyzed on a segmental (folder) level and compared on an interindividual basis. FT was not evaluated in this portion of the study; however, benchmark data from large radiological information system (RIS) evaluations (n = 170,901 reports, including 5,622 MRI reports) were used as reference.[10] These benchmark data were extracted from two large teaching hospitals with 23 full-time radiologists in New Zealand. Outliers with exceptionally long reporting times (>60 min for MRI) were culled, removing 9.5% of the total. Automatically generated GR ICD-10 codes[19] were compared with manual FT coding by a senior radiologist (A.H.).

Statistical analysis

Differences in reading duration by number of cases per reader were assessed using a trend test. A regression analysis was used to assess trends, first by reader and then using a mixed model for repeated measures (MMRM). In the MMRM, the data of all three readers were used within the same model, with the factor, "reader", used to indicate repeated measures. For sensitivity analysis in case of abnormality, a non-parametric Jonckheere–Terpstra trend test was used. Analyses were performed using SAS v. 9.4 software (SAS Institute Inc., Cary, NC, USA).

Results

Usability was rated high by all readers. Intuitive operation was rated very good by two readers and good by one reader. The coworking of image analysis and reporting was rated very good by all readers, and confidence in the automatically generated report compared with its FT counterpart was rated good. All readers reported increasing confidence during the study.

With respect to content differences between GR and FT, 41 patient reports (51.3%) received an A score (no differences in content), 33 patient reports (41.3%) received a B score (minor differences in content not resulting in differences in treatment), and 6 patient reports (7.5%) received a C score (major differences in content resulting in differences in treatment) (Table 2).

Of the 39 patient reports scoring B or C, 26 (66.7%) involved category 1 errors (COEs in v. 0.8 caused by insufficient operation of the software), and 13 (33.3%) involved category 2 errors (COEs caused by missing content in v. 0.8 of the software but displayable with v. 1.7). No category 3 errors (COEs caused by missing content in the v. 0.8 software and not displayable with v. 1.7) were identified.

No non-sense, omission/commission, or translation errors were observed in the GR reports. Spelling/grammar errors were observed in 3/80 (3.8%) GR patient reports (exclusively in the free-text discussion section), compared with 36/80 (45%) in FT patient reports.

Figure 3. Breast magnetic resonance imaging (MRI) of a 37-year-old woman with suspected cancer in the right breast. **(a)** Subtracted, early dynamic phase from contrast-enhanced MRI. **(b)** Screenshot of folder 10: report preview (the highlighted blue text in the Impression section was entered with free-text dictation).

Report Breast MRI. Pat-ID 080, born #
Patient data: The patient is 37 years old.
Indication: Lump/hardening in the right breast.
Anamnesis: Aunt (paternal) has a history of breast cancer.
Technique: Breast MRI with i.v. contrast agent (12.0 ml Gadobenic acid). Field strength: 3 T.

Findings:
Isomastia. No cutis thickening. Breast tissue: scattered fibroglandular tissue. Breast parenchyma has an inconspicuous appearance on T1w and T2w. Parenchyma with minimal contrast enhancement. Inconspicuous nipple on both sides.
Detection of a round mass right lower inter-quadrant.
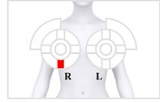
Reference image: series 14/image 87. Diameter: 9 mm. Contrast enhancement: Peripheral ring. Initially fast contrast uptake. Subsequently detection of a plateau in the contrast dynamic. Recognition of restricted diffusion. Differential diagnosis: breast carcinoma, not further specified.

Detection of a non-mass enhancement. Localisation: right upper outer quadrant.
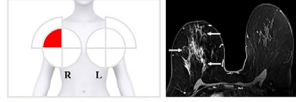
Segmental distribution. Differential diagnosis: breast carcinoma, not further specified.

No pathologic enlargement of axillary LN. No suspicious bone lesion.

Impression:
First breast MRI. No former MRI of the breast. Previous imaging: Former Mammography.

1. Detection of a round mass right lower inter-quadrant. Differential diagnosis: breast carcinoma, not further specified.
2. Detection of a non-mass enhancement. Localisation: right upper outer quadrant. Differential diagnosis: breast carcinoma, not further specified.
3. Not typical for a malignant phylloid tumor or granulomatous mastitis in asymptomatic patient.
4. No suspicious lesion in the left breast.
5. No suspicious lymph node.

Classification based on BI-RADS Version 4.0.
Amount of fibroglandular tissue: 2. BI-RADS (right side): 5. BI-RADS (left side): 1.
Recommendations:
Recommendation for ultrasound-guided biopsy of the right breast.

Discussion:

Question: The lump was detected in the right upper outer quadrant, scored BIRADS 0. Differential mastopathy or breast carcinoma?
Additional info: Distance between mass and NRE 10 mm. Direct contact between NRE and pectoralis muscle.

a

Report breast MRI, Pat-ID 080, Patient's date of birth: #

Question/indication
Palpable rigid lump in upper outer quadrant right breast, mammography BIRADS 0. Mastopathy, differential breast CA? Breast cancer aunt paternal side.

Technique: Breast MRI at 3 Tesla. Injection of 12 ml Multihance.

Findings
Initial examination.

Little-medium background activity.
Isomastia and symmetric nipples. Regular presentation of cutis and subcutis on both sides. Round lesion of 9 mm with ring enhancement in the right caudal breast at 6 o'clock. With a distance of approx. 10 mm normal mammary gland tissue of this extensive non-mass enhancement latero-cranially reaching far into the upper outer quadrant. The round lesion as well as the non-mass lesion mammary right show a rapid KM enhancement with plateau or an implied washout. Some small satellite-like lesions in addition, exemplified by 5 mm lesion series 14, Figure 87. Moderate diffusion restriction of these lesions. In depth, the lesion extends immediately to the pectoralis muscle.
The left breast shows no suspicious contrast enhancement or suspicious diffusion restriction. No pathologically enlarged axillary or mammaria interna lymph nodes.
No evidence of larger round foci in the partially imaged lung.
Regular bone marrow signal of the rib thorax. Regarding the upper abdominal organs, as far as included, no major pathological changes.

Impression
1. Malignant round lesion as well as a large non-mass lesion of the right breast with pathological contrast dynamics although with only moderate quantitative diffusion restriction. Close demarcation to the skin short-stretched and more distinct to musculus pectoralis.
   Biopsy/biopsies are strongly recommended to confirm the diagnosis, primarily sonographic.
2. Not typical for a malignant phylloid tumor or granulomatous mastitis in asymptomatic patient.
4. No suspicious lesion in the left breast.
5. No suspicious lymph node.

Right: MRM-BIRADS 5
Left: MRM-BIRADS 1

b

Figure 4. Depiction of two reports of the same patient in (a) was created with guided reporting (GR) technology. (b) was created with free-text dictation (FT). Major differences include GR's form, which includes embedded key images and localizers, and the absence of spelling/grammar errors. The short and to-the-point phrases of GR are much easier to understand (especially compared with sentences 5 and 6 in the FT findings section: "Round lesion…outer quadrant", which correspond to sentences 6 and 7 in the GR Findings section: "Detection of …not further specified"). The standardized GR glossary corresponds exactly to the recommendation of the state-of-the art BI-RADS Atlas,[38] whereas FT uses terms that are not exactly defined (such as "lesion") and unclear classifications [such as "little-medium activity", which corresponds to "parenchyma with minimal contrast enhancement" (sentence 4 in the GR Findings section)]. Free-text dictation reveals additional differences. For example, in FT, the phrase, "…extends immediately to the pectoralis muscle", differs from its GR counterpart, where the choice for the pectoralis muscle is a facultative radio button with the phrase, "bilaterally circumscribed margin" or "muscle invasion." The radio button is a graphical control element that allows the user to choose only one of a predefined set of mutually exclusive options. Guided reporting fulfills BI-RADS recommendations exactly,[38] with the decision about "pectoralis muscle invasion" included in the section of associated features. The relative description, "suspicion of," is not possible. Other minor differences are the phrase, "plateau or an implied washout" in FT, as opposed to the GR facultative radio button for delayed contrast enhancement choice between "progressive," "plateau," or "wash-out." BI-RADS, Breast Imaging Reporting and Data System.

Error category	Error type	Definition	Intended phrase example	Transcribed phrase example
Table 1. Error categorization according to a modified segmentation from Hawkins et al.[6]				
a	Non-sense	Passages, words, or phrases that make no sense or have no sensible meaning	No suspicious lesion in the breast	No suspension in the breast
b	Spelling/grammar (typographical and grammatical errors, homonyms, improper period usage)	Typographical errors, word misuse, duplicate periods, or lack of a period at the end of a sentence	There is a lesion in the left breast	There is a lesion in the light breast
c	c1: Omission (other)	Omitted words/phrases that do not result in a missense or non-sense error	There is no lesion in the left breast	There is no lesion left breast
	c2: Commission	A statement retained from a standardized template that contradicts dictated findings or impression	There is no lesion in the left breast	There is no lesion in the left breast. Mass in the left upper inner quadrant
d	Translational (other)	A translation error that does not result in a non-sense/missense error. The resulting sentence still has sensible meaning (as opposed to non-sense errors)	Breast parenchyma has an inconspicuous appearance	Breast parenchyma has an unobtrusive appearance

**Table 2.** Patient reports with a score of C: major differences in content resulting in differences in treatment

Patient; reader; case no.	MRM category; no. of lesions; lateralization	FT report content & MRM BI-RADS	GR report content & MRM BI-RADS	Difference FT vs. GR	Resulting difference in treatment	Error category	Change in GR b/t v. 0.8 and v. 1.7
34 y/o F; R3; case 5/36	Mass; 1; R	Large, centrally necrotic BC @ 12:00; diffuse, strongly enhancing parenchyma on the upper outer Q @ 9.00–10:00. Diffuse infiltration/ DCIS cannot be ruled out. BI-RADS (r/l): 6/2	Detection of mass in R upper interQ. Diagnosis: breast CA NOS. BIRADS (r/l): 6/2	Additional NME in R upper outer Q not described in GR (included in free-text "discussion").	Planning of more extended surgical resection due to additionally ipsilateral, NME.	2	Extended teaching of "loop function" (i.e., a software fxn to describe multiple lesions) during online training.
39 y/o F; R3; case 27/36	Mass; >3; R	MRM–BI-RADS 5 (or 6, if histological diagnosis available): malignant lesions, multicentric/ multifocal involvement of at least the two lower Qs. BI-RADS (l): 2	Detection of mass in R outer interQ, R lower outer Q, and R lower inner Q. Diagnosis: breast CA NOS. BI-RADS (r/l): 5/2	Explicit wording "multifocal" and "multicentric" missing in GR.	Multicentricity/ multi-focality have a (–) impact on prognosis, and more aggressive treatment options were used.[35]	2	Extended teaching of additional independent checkboxes, "multifoca" and "multicentric".
56 y/o F; R3; case 17/36	Exclusion of mass; 0; N/A	No malignant lesions on either side; no implant rupture of breast implants; no capsular fibrosis. BI-RADS (r/l): 1/1	Exclusion of a mass. BI-RADS (r/l): 1/1	Exclusion of implant rupture not explicitly expressed in GR (the automatically generated report would mention a rupture in case of a [+] finding).	Additional diagnostic examination(s) might be performed to check integrity of implants	1	In the chapter, "silicone implant", an additional radio button, "in-tact bilateral implants" added in v. 1.7
34 y/o F; R3; case 23/36	Mass; >4; bilateral	BRCA2 mutation. R: biopsy-confirmed, poorly differentiated breast CA w/ extension in all Qs; axillary lymph node metastases. L: three malignant areas. BI-RADS (r/l): 6/4	1. Detection of mass in R upper outer; R upper inner; R lower outer; and R lower inner Qs. Diagnosis: breast CA NOS; 2. Pathologic enlargement of R axillary lymph nodes; 3. Detection of mass in L lower interQ and L upper outer Q. Diagnosis: breast CA NOS. BI-RADS (r/l): 6/4	Information on BRCA mutation missing in GR.	The surgical treatment of patients with a genetic germline variant might be different from patients who are not carriers of BRCA.[36]	1	In the "indication" drop-down list, an additional criterion, "BRCA mutation/ genetically high risk", added in v. 1.7.
72 y/o F; R2; case 11/20	Mass; 2; R	Recurrence of moderately differentiated invasive breast CA 8 y after ipsilateral carcinoma. Two lesions: first lesion @ 10:00, max: 10 mm, irregular shape, margin spiculated, fast initial enhancement; second lesion @ 12:00; max: 4 mm; fast initial enhancement. BI-RADS (r/l): 6/1	1. Detection of mass in R upper outer Q. Diagnosis: invasive breast CA. 2. Detection of mass in R upper interQ. Diagnosis: invasive breast CA. BI-RADS (r/l): 6/1	Histological confirmation already available not explicitly covered in the wording of GR (though anticipated by categorization, BI-RADS 6 = known biopsy).	Next clinical step with FT would be surgery; next step with GR might be biopsy.	1	Checkbox "histological confirmation" added in v. 1.7.
77 y/o F; R3; case 35/36	NME; 1; L	Status after lobular breast CA on R with ablation, 2014; suspicion of mediastinal lymph node metastasis. L breast: newly developed, pronounced malignancy; suspicious contrast enhancement w/ suspicion of upper outer Q lobular CA. BI-RADS (r/l): 0/4	1. Detection of a NME L upper outer Q. Differential diagnosis: breast CA NOS. 2. Mediastinal lymph node metastasis. BI-RADS (r/l): 0/4	(Highly probable, from patient history) specific histology (= invasive lobular CA) of malignant lesion missing in GR.	Differences in clinical mgmt b/t invasive lobular and invasive ductal BC.[37]	1	Checkbox "histological confirmation" added/differential diagnoses of NME further extended to provide specific histology. In v. 1.7, different, more specific lesion types, including invasive lobular and invasive ductal breast CA, added to the drop-down list.

BRCA2, breast cancer gene 2; MRM, magnetic resonance mammography; BI-RADS, Breast Imaging Reporting and Data System; BC, breast cancer; CA, carcinoma; FT, free-text dictation; GR, guided reporting; Q, quadrant; NOS, not otherwise specified; DCIS, ductal carcinoma in situ; NME, non-mass enhancement.
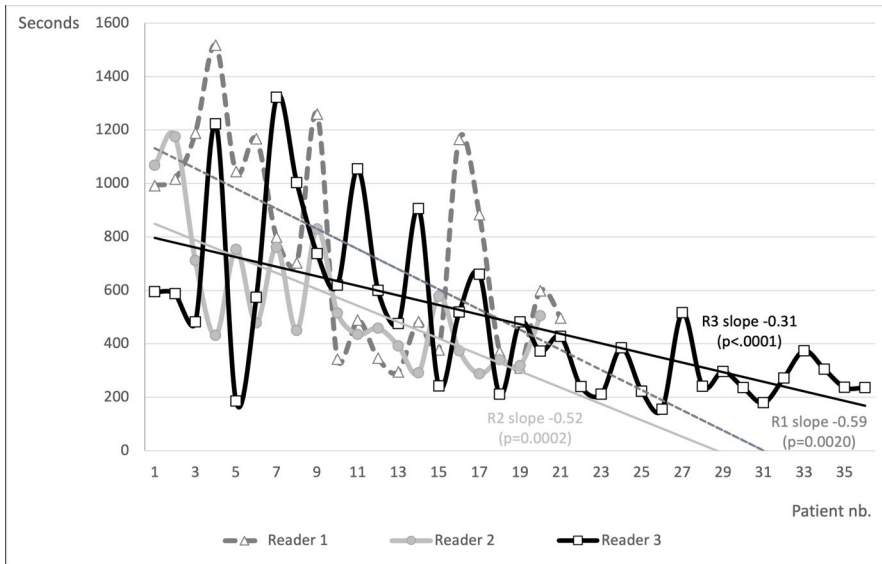
Figure 5. Reading duration for Readers 1, 2, and 3 with trend lines (number of cases per reader differed). The most significant learning curve occurred with Reader 1: with 21 reports, reading time decreased from 992–1,517 s for each of the first five reports to a minimum of 295 s by the 13th.

Three patients were excluded from the overall reading time analysis due to software issues (system instability resolved by remote maintenance). The mean reading time was 9 min 36 s (standard deviation: 5 min 27 s; min: 2 min 35 s; max: 25 min 17 s). The mean reading time per reader was 12 min 34 s (Reader 1), 9 min 17 s (Reader 2), and 8 min 5 s (Reader 3). The mean reading time for reports on patients without lesions was 11 min 16 s, 9 min 31 s for reports on patients with mass(es), and 7 min 31 s for reports on patients with focus/NME. The overall reading time was significantly shorter than FT radiology report reference values. The mean reading time for MRI examinations in general was 17 min 23 s (assessed from 1,629 h for 5,622 examinations).[10] Thus, compared with MRI examinations in general, reading time was shortened by 44.8%. More specifically, for breast MRI, a study-ascribable time (SAT) of 35 min was reported.[11] In contrast to the reading time analyzed in,[10] the SAT includes additional steps to reading and reporting, such as interpretation and clarification of request, prescription of the examination protocol, and communication with the referrer.[11]

The information fields in the software were unsurprisingly limited to two uses for one reader, as the users were highly specialized in breast imaging.

A learning curve with significant streamlining of the reading process (assessed by time to completion) during the training course was observed for all readers

(Figure 5). Regression models show reading time learning curve slopes of –0.59 (*P* = 0.002) for Reader 1, –0.52 (*P* = 0.0002) for Reader 2, and –0.31 (*P* < 0.0001) for Reader 3, with an average slope of –0.36 (*P* < 0.0001). As a certain deviance from normality was found in the data, a sensitivity analysis was performed using a non-parametric Jonckheere–Terpstra trend test. This test supported the results of the parametric regression analyses (Reader 1: *P* = 0.0157; Reader 2: *P* = 0.0015; Reader 3: *P* < 0.0001). A detailed analysis of the steps in the reporting process revealed differences between the readers (Figure 6). Reader 2 invested the greatest time allotment (38.4%) (Figure 6b) to folders 1 and 2 (patient/indication and anamnesis) of the GR process (compared with 33.3% and 27.9%, for Readers 1 and 3, respectively) (Figure 6a, c), suggesting that Reader 2 analyzed the image dataset in detail before beginning the reporting process. The relative time allotment for folder 6 (findings, which is the crux of a MR mammography report) was longer for Reader 3 (28.8%) compared with Readers 1 and 2 (21.9% and 21.0%, respectively). For folder 10 (report), the relative time allotment was longer for Reader 2 (17.6%) compared with Readers 1 and 3 (9.0% and 9.3%, respectively). This folder is used to check the text of the automatically generated report and the free-text entry of the discussion section, meaning that Readers 1 and 3 spent objectively less time in the acceptance or modification of the report text generated by the software than Reader 2.

The ICD-10 coding of the automatically generated GR reports was identical to manual FT coding and included the following codes: C22.9 (malignant neoplasm of the liver, not specified as primary or secondary; n = 1), C50.11 (malignant neoplasm of the central portion of the breast, n = 2), C50.21 (malignant neoplasm of the upper, inner quadrant; n = 2), C50.31 (malignant neoplasm of the lower, inner quadrant; n = 1), C50.41 (malignant neoplasm of the upper, outer quadrant; n = 7), C50.51 (malignant neoplasm of the lower, outer quadrant; n = 4), C50.81 (malignant neoplasm of overlapping sites of the breast; n = 34), C50.9 (malignant neoplasm of unspecified site of the breast; n = 1), D13.4 (benign neoplasm of the liver; n = 1), D24 (benign neoplasm of the breast; n = 1), N60.1 (diffuse cystic mastopathy; n = 3), N62 (hypertrophy of the breast; n = 2), N63 (unspecified lump in the breast; n = 15), R59.0 (enlarged lymph nodes; n = 17), T85.4 (mechanical complication of breast prosthesis and implant; n = 4), Z80.3 (family history of malignant neoplasm of the breast; n = 7), and Z85.3 (personal history of malignant neoplasm of the breast; n = 20). In total, 122 ICD-10 codes were generated.

Discussion

Differences between guided and structured reporting and the clinical need for guided reporting technology

GR is a modern, information technology (IT)-based solution developed to improve the workflow and quality of radiology reports. A standalone version of the software was used in this study, as opposed to integration into existing IT that occurs in clinical routine (e.g., picture archiving and communication systems and RIS. The benefits of SR have been reported in several publications.[20,21] Traditional narrative reporting is associated with high variability and is prone to error. According to Hawkins et al.[6], 41% of radiology reports contain errors, and 33% contain non-grammatical errors that can lead to quality issues in patient care (e.g., errors in electronic patient records) and poor-quality routine data for research. SR allows for a significant improvement in the quality of written reports. Text is generated automatically based on information input and is edited in a concise and standardized language. SR may be easy to implement into clinical workflow for uncomplicated cases; however, patients with complex pathologies involving different diseases (e.g., breast carcinoma combined with a benign bone tumor in the humerus)

with a wide range of findings require greater flexibility. Thus, percentages of unstructured free-text reporting in clinical settings will remain comparatively high.[20,21]

GR is a further development of SR. Major differences include reporting by anatomi-cal region, rather than by pathology, with a manageable number of 23 modules covering the whole spectrum of clinical MRI and CT examinations (plus X-ray mammography and breast ultrasound); the mapping of a complex cognitive decision tree developed by imaging specialists with a predefined point-by-point approach guiding radiologists through the reporting process, and the conscious exclusion of free text in the findings section and in the core components of the Impression section. The software provides error-free report texts: non-grammatical omission errors are reduced by the implementation of mandatory fields in the most relevant parts of the decision tree; plausibility checks reduce the risk of missense errors due to human failure; an intuitive and clear UX design focuses on risk reduction of commission errors; and intrinsic contradictions within the imaging report (e.g., between the findings and the impression sections) are prevented by waiving free-text entries. Digumarthy et al.[22] reported that 33 of 47876 radiology reports (876; 0.0007%) contained side discrepancies between the findings and impression sections. These discrepancies were revealed to be uncommon but quantifiable. Most discrepancies occurred in complex radiology reports involving multiple bilateral lesions with numerous citations of lateralization used to describe lesion distribution and location.[22]

Usability and performance of guided reporting: learning how to use the technology

Our starting hypothesis that the usability of GR software is intuitive and enables radiologists to produce high-quality breast MRI reports was confirmed by the high ratings of all readers. Of the 80 reports, 51.3% revealed no content differences between FT and GR, 41.3% contained minor differences in content between FT and GR not resulting in differences in treatment, and 7.5% contained major differences in content resulting in differences in treatment. All those reports containing major differences were COEs caused either by insufficient operation of the software or by an omission in the v. 0.8 software prototype displayable with the commercially available v. 1.7. Analysis revealed the need for extended training in 2/6 cases with the lowest score C (major differences in content, resulting in differences in treatment) and for additions to the decision tree in 4/6 cases. The importance of intensive training in the novel technology was clear from our study results. In conclusion, GR reports are complete, error-free, and without contradictions between the Findings and Impression sections. The error rate of 45% (mostly spelling and grammatical) in our evaluation of free-text narrative reporting by dictation can be lowered with the use of GR. Attached images and localizers within the GR system increase
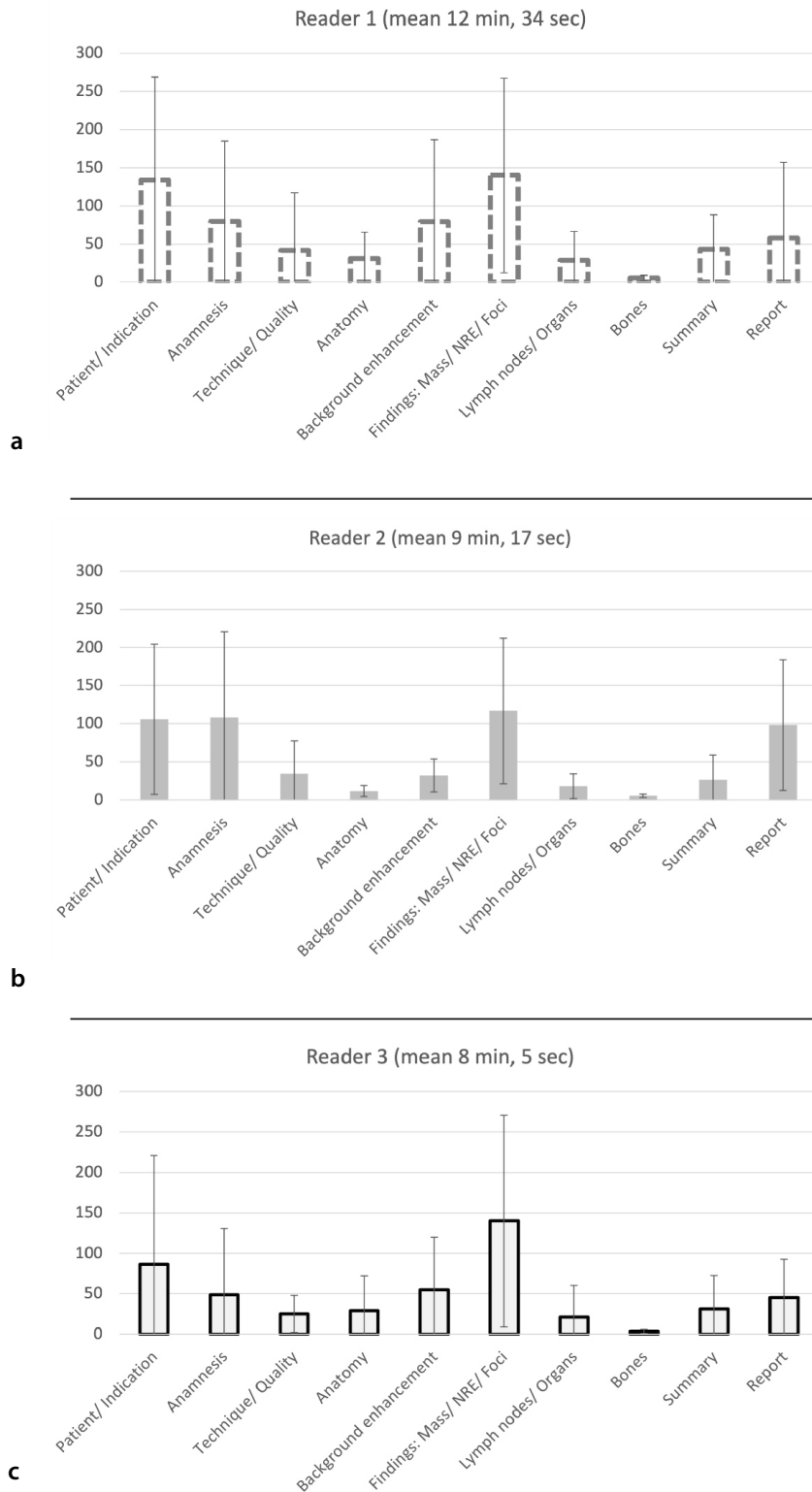
a

b

c

Figure 6. Evaluation times on a folder level; representations of means and standard deviations.

comprehensibility for referring physicians. It had been shown previously that reports with embedded images save time, increase physician confidence in treatment decisions, and may influence patient management.[23,24]

Increased reporting speed

The major attraction for radiologists in the use of GR in their daily routines is the reduction in reporting time. Staff shortages are a current bane in radiology; the number of scans and images per examination are rapidly rising, while the number of specialist radiologists remains more or less stagnant. In the U.S., MRI and CT rates increased by 124% and 110%, respectively, between 2000 and 2016.[25] In contrast, the total number of radiologists increased by only 39% between 1995 and 2011.[26] Our study was able to demonstrate a shortening of the combined reading and reporting time with GR compared with reference values from a narrative reporting process. The mean reading time for general MRI examinations was 17 min 39 s[10] and 35 min for breast MRI specifically.[11] Radiologist reporting times are a key component of radiology department workload assessment. Although of pivotal importance for management decisions, reliable measurements remain challenging.[27] Different methods have been described. Site-specific median reporting times (MRTs) are considered more precise than the SATs[27] introduced by Pitman et al.[11] in 2018. As the MRT described by Cowan et al.[10,27] was very similar to our site-specific method, it was selected as a comparator. Reading time was decreased by 44.8% (general MRI). The learning curve for all readers promises great time and cost savings potential.

The necessity of leaving prosaic radiology reporting

Numerous studies have found that structured, disease-focused dictation templates improve the comprehensiveness and appropriateness of radiologist reports.[18,20,21,28,29] Structure in reporting can help reduce errors (particularly typographical errors), train residents in the evaluation of complex examinations, and assist residents in recalling critical findings.[29] Structure in reporting is recommended in many MRI indications.[30,31]

In accordance, the following recommendation was published by the European Society of Radiology in 2018: "moving from conventional prose reports to SR is endorsed as a positive development, and must be an international effort, with international design and adoption of SR templates that can be translated and adapted in local environments as needed. Industry involvement is key to success, based on international data standards and guidelines".[32] In addition, IT-based reporting tools, and especially novel GR technology, are the basis for additional export formats of structured data (i.e., direct ICD-10 coding), as used in our study. Patient-friendly reporting, created with a single click, is essential to providing patient-centered and value-based care in the radiology of tomorrow.[33]

The limitations of our study include the setting of FT as the gold standard, preventing intra-individual comparison between FT and GR regarding reporting time, as well as its relatively small sample size and single-institution, retrospective design. Future studies with double reading and reporting in a randomized order using the commercial, CE-certified version of GR software are needed to validate the reduced combined reading and reporting time and to quantify reduced radiology turnaround times. An international multicenter design with a wider range of reader experiences would provide further insight into workflow improvements in different regional and education settings. An evaluation of all readers reading all to assess intra- and inter-reader reliability and variability was not performed and should be conducted in future studies to confirm the robustness of the advantages of GR technology. In addition, testing for missense errors in GR reports, and how they compare with those in FT reports, would need direct comparative analysis, with the images as a gold standard. Missense errors as defined by Hawkins et al.[6] (including their subclassifications into E1: translation errors, E2: errors of omission, and E3: human error, any of which could change the meaning of a phrase/sentence) could not be detected in our evaluation because FT was used as the gold standard.

In conclusion, GR allows for complete radiology reporting with a minimized error rate and a reduced combined reading and reporting time. Introducing this disruptive reporting strategy into clinical workflow requires management adjustments and intensive training, as has been emphasized by reports showing minor differences between GR and FT that are not caused by limitations of the software itself but by user-dependent operation. Shortening of reporting time is key for successful implementation into the clinical workflow. The great potential of structured datasets will open the doors for the future of radiology with respect to big data analysis, automatic ICD coding, and efficient artificial intelligence development. SR, and GR even more so, has the potential to facilitate developments in machine learning for radiological applications.[34]

Conflict of interest disclosure

Authors Igor Toker, Daniel Lorenz, and Alexander Huppertz declared that they are full-time or part-time employees of Neo Q Quality in Imaging GmbH. The other authors declared no conflict of interest.

References

1. Armas RR. Letter: qualities of a good radiology report. *AJR Am J Roentgenol*. 1998;170(4):1110. [CrossRef]

2. ACR Practice parameter for communication of diagnostic imaging findings. Accessed May 9, 2024. [CrossRef]

3. Hartung MP, Bickle IC, Gaillard F, Kanne JP. How to create a great radiology report. *Radiographics*. 2020;40(6):1658-1670. [CrossRef]

4. Ignácio FCGR, de Souza LRMF, D'Ippolito G, Garcia MM. Radiology report: what is the opinion of the referring physician? *Radiol Bras*. 2018;51(5):308-312. [CrossRef]

5. Gunn AJ, Alabre CI, Bennett SE, et al. Structured feedback from referring physicians: a novel approach to quality improvement in radiology reporting. *AJR Am J Roentgenol*. 2013;201(4):853-857. [CrossRef]

6. Hawkins CM, Hall S, Zhang B, Towbin AJ. Creation and implementation of department-wide structured reports: an analysis of the impact on error rate in radiology reports. *J Digit Imaging*. 2014;27(5):581-587. [CrossRef]

7. Brady AP. Error and discrepancy in radiology: inevitable or avoidable?. *Insights Imaging*. 2017;8(1):171-182. [CrossRef]

8. Onder O, Yarasir Y, Azizova A, Durhan G, Onur MR, Ariyurek OM. Errors, discrepancies and underlying bias in radiology with case examples: a pictorial review. *Insights Imaging*. 2021;12(1):51. [CrossRef]

9. Kim YW, Mansfield LT. Fool me twice: delayed diagnoses in radiology with emphasis on perpetuated errors. *AJR Am J Roentgenol*. 2014;202(3):465-470. [CrossRef]

10. Cowan IA, MacDonald SL, Floyd RA. Measuring and managing radiologist workload: measuring radiologist reporting times using data from a radiology information system. *J Med Imaging Radiat Oncol*. 2013;57(5):558-566. [CrossRef]

11. Pitman A, Cowan IA, Floyd RA, Munro PL. Measuring radiologist workload: progressing from RVUs to study ascribable times. *J Med Imaging Radiat Oncol*. 2018;62(5):605-618. [CrossRef]

12. Bartsch E, Shin S, Roberts S, et al. Imaging delays among medical inpatients in Toronto, Ontario: A cohort study. *PLoS One*. 2023;18(2):e0281327. [CrossRef]

13. Sistrom CL. Conceptual approach for the design of radiology reporting interfaces: the talking template. *J Digit Imag*. 2005;18(3):176-187. [CrossRef]

14. Jorg T, Kämpgen B, Feiler D, et al. Efficient structured reporting in radiology using an intelligent dialogue system based on speech recognition and natural language processing. *Insights Imaging*. 2023;14(1):47. [CrossRef]

15. European Society of Radiology (ESR). ESR paper on structured reporting in radiology-update 2023. *Insights Imaging*. 2023;14(1):199. [CrossRef]

16. Pesapane F, Tantrige P, De Marco P, et al. Advancements in standardizing radiological reports: a comprehensive review. *Medicina (Kaunas)*. 2023;59(9):1679. [CrossRef]

17. Nobel JM, van Geel K, Robben SGF. Structured reporting in radiology: a systematic review to explore its potential. *Eur Radiol*. 2022;32(4):2837-2854. [CrossRef]

18. Larson DB, Towbin AJ, Pryor RM, Donnelly LF. Improving consistency in radiology reporting through the use of department-wide standardized structured reporting. *Radiology*. 2013;267(1):240-250. [CrossRef]

19. ICD-10-CM Official Guidelines for Coding and Reporting. FY 2021 – UPDATED January 1, 2021. assessed May 9, 2024. [CrossRef]

20. Pinto Dos Santos D, Hempel JM, Mildenberger P, Klöckner R, Persigehl T. Structured Reporting in Clinical Routine. *Rofo*. 2019;191(1):33-39. [CrossRef]

21. Ganeshan D, Duong PT, Probyn L, et al. Structured reporting in radiology. *Acad Radiol*. 2018;25(1):66-73. [CrossRef]

22. Digumarthy SR, Vining R, Tabari A, et al. Process improvement for reducing side discrepancies in radiology reports. *Acta Radiol Open*. 2018;7(7-8):2058460118794727. [CrossRef]

23. Iyer VR, Hahn PF, Blaszkowsky LS, Thayer SP, Halpern EF, Harisinghani MG. Added value of selected images embedded into radiology reports to referring clinicians. *J Am Coll Radiol*. 2010;7(3):205-210. [CrossRef]

24. Patel BN, Lopez JM, Jiang BG, Roth CJ, Nelson RC. Image-Rich radiology reports: a value-based model to improve clinical workflow. *J Am Coll Radiol*. 2017;14(1):57-64. [CrossRef]

25. Radiology Business News, September 04, 2019. Imaging utilization continues to rise-should that be viewed as a negative? [CrossRef]

26. Rosenkrantz AB, Hughes DR, Duszak R Jr. The U.S. Radiologist workforce: an analysis of temporal and geographic variation by using large national datasets. *Radiology*. 2016;279(1):175-184. [CrossRef]

27. Cowan IA, Floyd RA. Measurement of radiologist reporting times: assessment of precision, comparison of three different measurement techniques and review of potential applications. *J Med Imaging Radiat Oncol*. 2023;67(7):734-741. [CrossRef]

28. Dickerson E, Davenport MS, Syed F, et al. Effect of template reporting of brain MR imagings for multiple sclerosis on report thoroughness and neurologist-rated quality: results of a prospective quality improvement project. *J Am Coll Radiol*. 2017;14(3):371-379. [CrossRef]

29. Johnson TF, Brinjikji W, Doolittle DA, Nagelschneider AA, Welch BT, Kotsenas AL. Structured head and neck CT angiography reporting reduces resident revision rates. *Curr Probl Diagn Radiol*. 2019;48(2):114-116. [CrossRef]

30. Beets-Tan RGH, Lambregts DMJ, Maas M, et al. MR imaging for clinical management of rectal cancer: Updated recommendations from the 2016 European Society of Gastrointestinal and Abdominal Radiology (ESGAR) consensus meeting. *Eur Radiol*. 2018;28(4):1465-1475. [CrossRef]

31. Maas M, Dijkhoff RAP, Beets-Tan R. Rectal cancer: assessing response to neoadjuvant therapy. *Magn Reson Imaging Clin N Am*. 2020;28:117-126. [CrossRef]

32. European Society of Radiology (ESR). ESR paper on structured reporting in radiology. *Insights Imaging*. 2018;9(1):1-7. [CrossRef]

33. Rockall AG, Justich C, Helbich T, Vilgrain V. Patient communication in radiology: moving up the agenda. *Eur J Radiol*. 2022;155:110464. [CrossRef]

34. Pinto Dos Santos D, Baeßler B. Big data, artificial intelligence, and structured reporting. *Eur Radiol Exp*. 2018;2(1):42. [CrossRef]

35. Neri A, Marrelli D, Megha T, et al. Clinical significance of multifocal and multicentric breast cancers and choice of surgical treatment: a retrospective study on a series of 1158 cases. *BMC Surg*. 2015;15(1):1. [CrossRef]

36. Tung NM, Boughey JC, Pierce LJ, et al. Management of hereditary breast cancer: American Society of Clinical Oncology, American Society for Radiation Oncology, and Society of Surgical Oncology Guideline. *J Clin Oncol*. 2020;38(18):2080-2106. [CrossRef]

37. Barroso-Sousa R, Metzger-Filho O. Differences between invasive lobular and invasive ductal carcinoma of the breast: results and therapeutic implications. *Ther Adv Med Oncol*. 2016;8(4):261-266. [CrossRef]

38. ACR BI-RADS Atlas. Breast Imaging Reporting and Data System. 5th ed. 2014. *American College of Radiology*. ISBN 9781559030168. [CrossRef]

CARDIOVASCULAR IMAGING

ORIGINAL ARTICLE

Evaluating small coronary stents with dual-source photon-counting computed tomography: effect of different scan modes on image quality and performance in a phantom

🄳 Thomas Stein[1]
🄳 Constantin von zur Muhlen[2]
🄳 Niklas Verloh[1]
🄳 Till Schürmann[1]
🄳 Tobias Krauss[1]
🄳 Martin Soschynski[1]
🄳 Dirk Westermann[2]
🄳 Jana Taron[1]
🄳 Elif Can[1]
🄳 Christopher L. Schlett[1]
🄳 Fabian Bamberg[1]
🄳 Christopher Schuppert[1]
🄳 Muhammad Taha Hagar[1]

[1]Medical Center-University of Freiburg Faculty of Medicine, Department of Diagnostic and Interventional Radiology, Freiburg, Germany

[2]Medical Center-University of Freiburg Faculty of Medicine, Department of Cardiology and Angiology, Freiburg, Germany

Corresponding author: Muhammad Taha Hagar

E-mail: taha.hagar@uniklinik-freiburg.de

PURPOSE

The study aimed to assess the feasibility and image quality of dual-source photon-counting detector computed tomography (PCD-CT) in evaluating small-sized coronary artery stents with respect to different acquisition modes in a phantom model.

METHODS

Utilizing a phantom setup mimicking the average patient's water-equivalent diameter, we examined six distinct coronary stents inflated in a silicon tube, with stent sizes ranging from 2.0 to 3.5 mm, applying four different CT acquisition modes of a dual-source PCD-CT scanner: "high-pitch," "sequential," "spiral" (each with collimation of 144 × 0.4 mm and full spectral information), and "ultra-high-resolution (UHR)" (collimation of 120 × 0.2 mm and no spectral information). Image quality and diagnostic confidence were assessed using subjective measures, including a 4-point visual grading scale (4 = excellent; 1 = non-diagnostic) utilized by two independent radiologists, and objective measures, including the full width at half maximum (FWHM).

RESULTS

A total of 24 scans were acquired, and all were included in the analysis. Among all CT acquisition modes, the highest image quality was obtained for the UHR mode [median score: 4 (interquartile range (IQR): 3.67–4.00)] ($P = 0.0015$, with 37.5% rated as "excellent"), followed by the sequential mode [median score: 3.5 (IQR: 2.84–4.00)], $P = 0.0326$ and the spiral mode [median score: 3.0 (IQR: 2.53–3.47), $P > 0.05$]. The lowest image quality was observed for the high-pitch mode [median score: 2 (IQR: 1– 3), $P = 0.028$]. Similarly, diagnostic confidence for evaluating stent patency was highest for UHR and lowest for high-pitch ($P < 0.001$, respectively). Measurement of stent dimensions was accurate for all acquisition modes, with the UHR mode showing highest robustness (FWHM for sequential: 0.926 ± 0.061 vs. high-pitch: 0.990 ± 0.083 vs. spiral: 0.962 ± 0.085 vs. UHR: 0.941 ± 0.036, P = non-significant, respectively).

CONCLUSION

Assessing small-sized coronary stents using PCD-CT technology is feasible. The UHR mode offers superior image quality and diagnostic confidence, while all modes show consistent and accurate measurements.

CLINICAL SIGNIFICANCE

These findings highlight the potential of PCD-CT technology, particularly the UHR mode, to enhance non-invasive coronary stent evaluation. Confirmatory research is necessary to influence the guidelines, which recommend cardiac CT only for stents of 3 mm or larger.

KEYWORDS

Computed tomography, coronary artery, stents, technology

Coronary computed tomography (CT) computed tomography angiography (CTA) is an indispensable diagnostic tool for ruling out obstructive coronary artery disease (CAD) in patients with a low to intermediate risk profile.[1] While its use in patients with pre-existing CAD is generally more restrained, recent guidelines have acknowledged its reasonable use in assessing stent patency for patients experiencing symptomatic changes and if stents with an internal diameter of 3 mm or greater are present.[2,3] This is attributed to the diagnostic difficulties introduced by blooming artifacts, which originate from stent materials and consequently restrict the effectiveness of CTA-hence the restraint regarding larger stent diameters.[4,5]

With the clinical introduction of novel photon-counting detector (PCD) CT technology, there is a potential advancement in overcoming these challenges. This technology eliminates the need for septa within the detector elements and allows improvement in geometrical dose efficiency and electrocardiogram (ECG)-synchronized CTA at ultra-high resolution (UHR) by utilizing a direct conversion process for incoming X-ray photons and semiconductor plate technology.[6] ECG-synchronized CTA is a special imaging procedure that is primarily used to examine the structure and function of the heart. In this method, the CT scanner is synchronized with the patient's ECG signal, allowing the scanner to acquire images at specific points in the cardiac function. This synchronization helps to reduce the motion artifacts caused by the beating heart, resulting in better and more detailed images of the heart and its vessels, which is crucial for the accurate diagnosis of heart diseases and conditions. More-

over, a dual-source CT system using PCD-CT technology is clinically available. Recent studies have demonstrated the potential of PCD-CT to reduce artifacts significantly and improve image quality in non-invasive stent assessment, compared with traditional energy-integrating detector (EID) CT.[7] Photon-CT utilizes detectors that do not require septa for lightning photons, unlike EID-CT. The PCD design incorporates application-specific integrated circuits instead of photodiodes, facilitating the construction of smaller detector pixels. As a result, PCD-CT achieves higher spatial resolution, better delineation of structure edges, and reduces the spread of signals from high-density objects, effectively mitigating blooming artifacts. Additionally, PCD-CT's capability to directly count and measure the energy of individual photons allows for precise material differentiation, minimizing the impact of overlapping densities. Moreover, PCD-CT reduces image noise by directly converting X-ray photons into electrical signals, enhancing image clarity and reducing blooming artifacts. Initial human and phantom studies have shown promising results for PCD-CT in stent evaluation, particularly when employing a sharp vascular convolution kernel.[8,9] This approach has facilitated excellent *in vivo* visualization of stent lumens, with a recent study achieving a 100% negative predictive value for stent patency evaluation against invasive angiography as the reference standard.[10]

However, a dedicated analysis of PCD-CT's performance in evaluating coronary artery stents with an internal diameter of 3 mm or less is lacking. Therefore, our study aims to evaluate the feasibility and assess the image quality of PCD-CT in evaluating small-sized coronary artery stents. Furthermore, we seek to investigate which specific scan mode provides the highest performance and image quality.

Methods

Ethical statement

This study used an *ex vivo* phantom model; therefore, ethical approval and the Dec-

laration of Helsinki were not applicable. The additionally presented *in vivo* case is part of a larger study sanctioned by the Institutional Review Board of University Medical Center, Freiburg (approval no: 21-2469, date: 09/21/2021), investigating the functionalities and properties of photon-counting CT in various clinical scenarios. Patient consent was not required.

Phantom setup

The experimental setup utilized in this current study was previously published.[11] A phantom mimicking the average (avg) patient's water-equivalent diameter (D_w) value was constructed based on the analysis of 457 consecutive patients (189 women, 268 men; age 61.15 ± 12.95 years; median body mass index 27.2; range 17.2–58.8) undergoing cardiac CT. The D_w value was calculated using a dose management system (DoseM, Infinitt EU, Frankfurt, Germany) according to AAPM TG220,[12] with an avg D_w of 27.5 cm determined. The phantom, comprising a polymethyl-methacrylate frame (36.0 × 24.5 cm) filled with tap water, achieved a D_w of 28.0 cm. For CT measurements, various stents were inflated within silicone tubes at pressures specified by the manufacturer's *in vitro* compliance table and mounted at the phantom's isocenter. Silicone tubes were chosen for their minimal interference in image quality.

Coronary stents

Six distinct coronary stents with small diameters were examined, each differing in size and from various manufacturers. The sizes of these stents ranged from 2.0 to 3.5 mm. The characteristics of each stent are shown in Table 1.

Contrast media

The stent-containing silicon tubes were filled with an iodinated contrast medium (Imeron 400, Bracco Imaging, Italy) and diluted to achieve a radiodensity of 800 Hounsfield units (HU) at a tube voltage of

Main points

- Evaluating small coronary stents with conventional computed tomography (CT) is challenging due to blooming artifacts.

- This study assessed dual-source photon-counting detector (PCD) CT using different acquisition modes in a phantom model.

- The ultra-high-resolution (UHR) mode provided the best image quality, with an excellent median score of 4.0, and the highest diagnostic confidence ($P < 0.001$).

- All scan modes showed consistent and accurate stent measurements, with the UHR mode scoring a full width at half maximum of 0.941 ± 0.036 mm.

- The use of PCD-CT technology is promising for non-invasive small-sized stent evaluation; further clinical validation is needed to initiate guideline revision.

Table 1. Characteristics of coronary stents used in the study, including size, length, and properties

Manufacturer	Name	Size (mm)	Length (mm)	Properties
Monorail	Synergy	3.50	8.00	Everolimus-eluting
Synsiro	Biotronik	3.00	26.00	Sirolimus-eluting
Monrail	Promus Elite	2.75	8.00	Everolimus-eluting
Monrail	Promus Elite	2.50	8.00	Everolimus-eluting
Monrail	Promus Elite	2.25	32.00	Everolimus-eluting
Medtronic	Resolute Onyx	2.00	12.00	Zotarolimus-eluting

120 kVp. To ensure an even distribution of the contrast agent and to prevent any sedimentation, a flow-simulating pump was incorporated into the phantom setup. This device was used to simulate a blood flow rate of 2.0 mL/s, mirroring physiological conditions. Details of the contrast medium specifications are presented in Table 2.

Computed tomography scan parameters and image reconstruction

All scans were performed on a 1st generation, dual-source PCD CT scanner (NAEOTOM Alpha, Siemens Healthineers AG, software version VA50). In total, four different scans were performed for each stent: 1) a prospectively ECG-synchronized high-pitch spiral CT ("flash"), 2) a prospectively ECG-triggered sequential scan ("sequential"), 3) a retrospectively ECG-gated spiral CT ("spiral"); all featured full spectral sensitivity and a collimation of 144 × 0.4 mm. Last, a retrospective spiral CT employing the ultrahigh-spatial-resolution scan mode ("UHR") without

spectral information and a collimation of 120 × 0.2 mm was acquired. The tube voltage was set at 120 kVp, and a constant effective tube current of 32 mAs was maintained across all scans to standardize image quality and ensure consistent diagnostic accuracy, in line with the manufacturer's recommendations for the CT scanner used. To mimic a typical z-axis extension of cardiac CT, the scan length was set at 120 mm each.[13,14] Images were reconstructed to a field of view of 140 × 140 mm and a matrix size of 512 × 512 pixels. Axial images were reconstructed employing an intermediate sharp vascular convolution kernel (Bv60) and Quantum Iterative Reconstruction at level 3. Detailed CT scan and reconstruction parameters are outlined in Table 3.

Computed tomography data analysis

All CT scans were evaluated by two independent board-certified radiologists (MTH, CS; 5 and 6 years of experience in cardiac CT, respectively) on a dedicated and clinically approved workstation (Dedalus HealthCare, Bonn, Germany). Images were provided in the transversal orientation, with a default window level of 850 HU and a window width of 2.200 HU. The readers were permitted to adjust the window settings as desired and to perform multiplanar reconstructions for their analysis.

Visual and subjective image quality assessment

The overall subjective image quality of the stented lumen was evaluated using a four-point visual grading scale, considering sharpness, noise, blooming artifact interference, and diagnostic confidence for assessing stent patency. The grading scale for each parameter was defined as follows: For overall image quality, a score of 1 indicated non-diagnostic quality, characterized by poor lumen attenuation with significant artifact interference from stent struts; a score of 2 indicated fair quality, with moderate interference from stent struts but interpretable lumen attenuation; a score of 3 represented good quality, with mild interference from stent struts and generally clear lumen attenuation; and a score of 4 indicated excellent quality, marked by clear lumen attenuation without artifact interference from stent struts.

Noise levels and blooming were scored inversely, with minimal noise or blooming receiving a score of 1 and extensive noise or blooming receiving a score of 4. Specifically, for noise levels, a score of 1 indicated minimal noise with a homogenous lumen appearance; a score of 2 indicated mild noise that did not significantly affect image interpretation; a score of 3 indicated moderate noise that may impact image clarity; and a score of

Table 2. Contrast medium specifications

Iodine concentration (mgI/mL)	400
Volume (mL)	70
Flow rate (mL/s)	2.0
Iodine flux (g/s)	0.8
Total iodine dose (g)	28

Table 3. Computed tomography scan and reconstruction parameters

	Flash	Sequential	Spiral	UHR
ECG-synchronization	Prospective	Prospective	Retrospective	Retrospective
Scan length (mm)	120	120	120	120
Scan direction	Cranio-caudal	Cranio-caudal	Cranio-caudal	Cranio-caudal
Tube voltage (kV)	120	120	120	120
Effective mAs	32	32	32	32
CARE IQ level	135	135	135	82
CTDI$_{vol}$ (mGy)	2.33	11.8	28.2	35.0
DLP (mGy x cm)	40.7	146	428	485
Rotation time (ms)	250	250	250	250
Pitch	3.2	N/A	0.2	0.2
Slice collimation (mm)	144 × 0.4	144 × 0.4	144 × 0.4	120 × 0.2
Slice width (mm)	0.4	0.4	0.4	0.2
Increment (mm)	0.2	0.2	0.2	0.1
Matrix size (pixels)	512 × 512	512 × 512	512 × 512	512 × 512
Field of view (mm)	140 × 140	140 × 140	140 × 140	140 × 140
Reconstruction kernel	Bv60	Bv60	Bv60	Bv60
Iterative reconstruction	QIR level 3	QIR level 3	QIR level 3	QIR level 3
Spectral reconstruction	Monoenergetic + 67 keV	Monoenergetic + 67 keV	Monoenergetic + 67 keV	Polychromatic (T3D)

ECG, electrocardiogram; CTDI$_{vol}$, computed tomography dose index volume; DLP, dose-length-product; N/A, not-applicable; QIR, quantum iterative reconstruction; UHR, ultra-high-resolution.

4 indicated extensive noise that made image interpretation difficult. For blooming artifact interference, a score of 1 indicated minimal blooming with clear visualization of stent struts; a score of 2 indicated mild blooming that did not significantly obscure stent struts; a score of 3 indicated moderate blooming that partially obscured stent struts; and a score of 4 indicated extensive blooming that significantly obscured stent struts.

Diagnostic confidence for evaluating in-stent lumen patency ranged from non-diagnostic (score of 1), where lumen patency could not be assessed, to reduced confidence (score of 2), where lumen patency assessment was possible but with reduced confidence, to good confidence (score of 3), where lumen patency could be assessed with good confidence, and ultimately to excellent confidence (score of 4), where lumen patency could be assessed with high confidence.

Quantitative objective image quality assessment

Full width at half maximum

Two readers measured coronary stent length and internal and external diameters on reformatted CT images, focusing on the axial slice that best-represented stent geometry. To quantify blooming systematically, sagittal cross-sectional images along the phantom's axis were first reconstructed. Subsequently, attenuation profiles were avg over multiple voxels perpendicular to the longitudinal axis of the stent, establishing an avg attenuation profile. Utilizing these attenuation profiles, the full width at half maximum (FWHM) for both intensity peaks was calculated for all stents under each acquisition mode. The mean of these two FWHM values was then used to derive measurement consistency for the stent corresponding to each acquisition mode, as depicted in Figure 1.

Effect on in-stent lumen attenuation, contrast-to-noise ratio, and signal-to-noise ratio

Three manually drawn regions of interest (ROIs) were performed: an in-stent ROI (ROI_{in_stent}), carefully avoiding stent struts with a minimum 4 mm^2 area, and two identical-sized ROIs at the adjacent vessel lumen relative to the stent ($ROI_{proximal\ vessel}$ and $ROI_{distal\ vessel}$), placed within 10 mm of the stent's ends. The avg HU and standard deviation (SD) were noted for every ROI. The following equation was applied to evaluate the attenuation changes caused by the stent in the lumen ($HU_{In-stent}$):

$$HU_{In\_stent} = avgHU_{in\_stent} - \frac{avgHU_{proximal\ vessel} + avgHU_{distal\ vessel}}{2}$$

Two circular ROIs of 250 mm^2 were placed within the water around the stent, and the avg, as well as SD and HU, were noted. The signal-to-noise ratio (SNR) and contrast-to-noise ratio (CNR) were calculated as follows:

$$SNR = \frac{avgHU\ vessel}{SD\ HU\ water} \qquad CNR = \frac{avgHU\ vessel - avg\ HU\ water}{SD\ HU\ water}$$
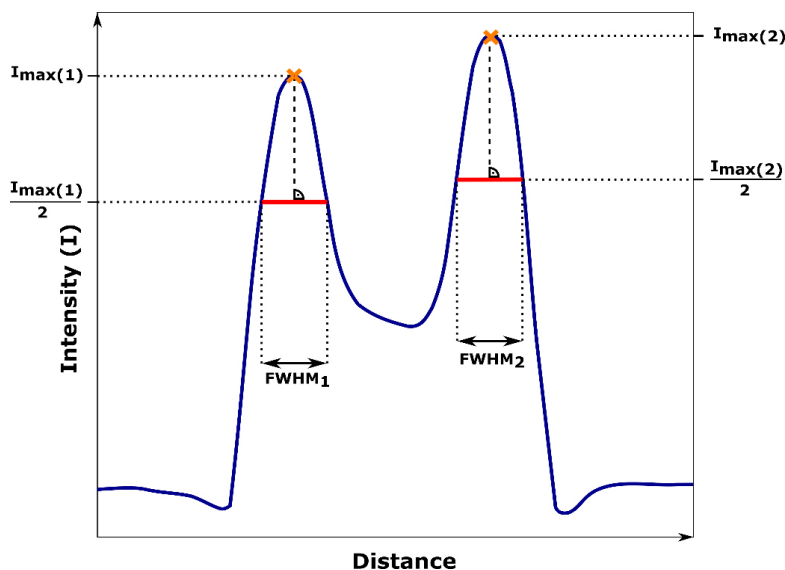
Figure 1. Displays the mean intensity profile of an entire stent. For every acquisition mode and each stent, the full width at half diameter was calculated to account objectively for stent-induced blooming artifact interference. FWHM, full width at half maximum.

Statistical analysis

Statistical analyses were performed using open-source Python (version 3.9.13) and Jupyter Notebooks. The Shapiro–Wilk test was used to check for the presumption of normal distribution. Quantitative variables with normal distribution were expressed as mean ± SD. Categorical variables were presented as frequencies and percentages in parentheses. Non-normally distributed variables, such as subjective image quality scores or attenuation, were expressed as the median and interquartile range (IQR), and their comparisons across different acquisition modes were analyzed using the Kruskal–Wallis test. Analysis of variance (ANOVA) was performed to determine the statistical significance of the differences in FWHM measurements across the four CT acquisition modes. Following a significant ANOVA result, post-hoc pairwise comparisons were conducted using Tukey's honestly significant difference (HSD) test to identify which specific acquisition modes differed from one another. To account for the increased risk of type I error due to multiple comparisons, the Bonferroni correction was applied to all P values. A P value of <0.05 was considered statistically significant. For testing diagnostic accuracy, 95% confidence intervals (CIs) were reported. All statistical measurements were performed by TS (4 years of experience).

Results

For all six small-sized stents, four consecutive scans using different acquisition methods were performed. Representative images for a stent measuring 2.0 mm in diameter are presented in Figure 2. Figure 3 summarizes the overall subjective assessments of diagnostic confidence for evaluating stent patency, sharpness, blooming artifact interference, and noise; Table 3 outlines the overall image quality and objective quality evaluation metrics.

Visual and subjective image quality assessment

The UHR mode provided the highest subjective image quality across all stent sizes, with a median score of 4 (CI: 3.67–4.00), categorizing 18 (37.5%) of the images as "excellent." Sequential and spiral modes showed slightly lower subjective image quality, with median values of 3.5 (CI: 2.84–4.00) and 3.0 (CI: 2.53–3.47), respectively. The flash mode provided the lowest subjective image quality, with a median value of 2.25 (CI: 1.66–2.84)) and was considered "non-diagnostic"

in 3 (6.3%) stents. Subjective and objective image qualities relative to the acquisition mode are displayed in Table 4.

When analyzing the acquisition modes in detail for different stent sizes, the UHR mode provided the highest performance in terms of image quality across various stent diameters, with statistically significant differences identified when compared with the flash mode (CI: 1.31–2.85, P = 0.0015) and when compared with the spiral mode (CI: 2.38-3.69, P = 0.0284). The sequential mode did not differ significantly from the UHR-spiral mode in pairwise comparisons (CI: 2.47–4.11, P = 0.3236). Details on subjective image quality distribution relative to stent size are provided in Table 5.

Visual and subjective sharpness analysis

The analysis of stent sharpness revealed that the UHR mode was significantly associated with the highest mean sharpness scores across all stent sizes, achieving a value of 4.00 (CI: 3.67–4.33), whereas the flash mode achieved a median value of 2.00 (CI: 1.97–2.21). The sequential mode showed moderate performance, with a score of 3.00 (CI: 2.53–3.47), whereas the spiral mode showed a median of 2.50 (CI: 1.8–3.20), with P = 0.0349 compared with the UHR mode. Stent sizes did not affect overall sharpness (Tukey HSD P > 0.05). Overall, the statistical analysis emphasizes the superior performance of the UHR mode regarding sharpness across the range of stent diameters. Significant differences were found in comparisons with the flash mode (P = 0.0007) and spiral mode (P = 0.0349), and again, the sequential mode's differences were not significant (P = 0.2279).

Visual and subjective noise analysis

The analysis of noise levels across different stent sizes and acquisition modes revealed that the UHR-spiral mode was associated with the highest mean noise level of 3.00 (CI: 2.67–3.33), indicating it produced the most noise among the acquisition modes tested. In contrast, the flash mode showed improved noise performance with 2.25 (CI: 1.34–2.66), with significant differences compared with UHR (P = 0.0217). Sequential and spiral modes demonstrated intermediate noise levels with 2.50 (CI: 1.84–3.16) and 2.25 (CI: 1.70–2.80), respectively. Analysis of noise levels in relation to stent diameters did not show significant variation (Tukey HSD P > 0.05, respectively).

Visual and subjective diagnostic confidence for evaluating stent patency

In evaluating coronary stents using the different cardiac CT scan modes-sequential, spiral, UHR, and flash-the results showed a median "good" diagnostic confidence of 3.0 (IQR, 2.0–4.0) for sequential, for spiral a "good" median score of 3.0 (IQR, 3.0–4.0), and for flash a "reduced" median score of 2.0 (IQR, 2.0–3.0). The UHR mode provided the highest diagnostic confidence median of 3.5, with an IQR of 1.0 (3.0–4.0). The UHR mode demonstrated superior performance by achieving "good" or "excellent" diagnostic confidence in all readings (n = 12), which corresponds to 100.00% of its evaluations. The spiral scan mode followed, achieving "good" or "excellent" diagnostic confidence in 9 out of 12 readings (75%). The sequential scan mode reported "good" or "excellent" confidence levels in 9 out of 12 readings, translating to 75% of the time, while the flash scan mode achieved these levels of confidence in 3 instances or 25% of cases. Detailed metrics on diagnostic confidence are presented in Table 6, and an *in vivo* imaging example is provided in Figure 4.

Full width at half maximum measurements

The inner stent diameters were consistently measured across all modes, averaging 1.8 ± 0.4 mm; the outer diameter measurements showed a slight variation, with an overall avg of 3.1 ± 0.5 mm. The FWHM values were uniformly distributed, with a mean of 0.947 ± 0.067 mm across all scans.

The most stable mean FWHM was found to be 0.941 mm (CI: 0.912–0.971) in the UHR mode, followed by the sequential mode (FWHM of 0.926, CI: 0.876–0.975), indicating the least amount of blooming artifact interference. The flash mode displayed the highest mean FWHM of 0.990 mm (CI: 0.924–1.057), potentially indicating more blooming susceptibility. However, the differences across acquisition modes did not reach statistical significance (ANOVA P = 0.386). The sequential and spiral modes yielded similar mean FWHM results of 0.926 mm (CI: 0.877–0.975) and 0.932 mm (CI: 0.863–1.000), respectively, with no significant differences compared with the UHR-spiral mode (Bonferroni corrected P > 0.05).
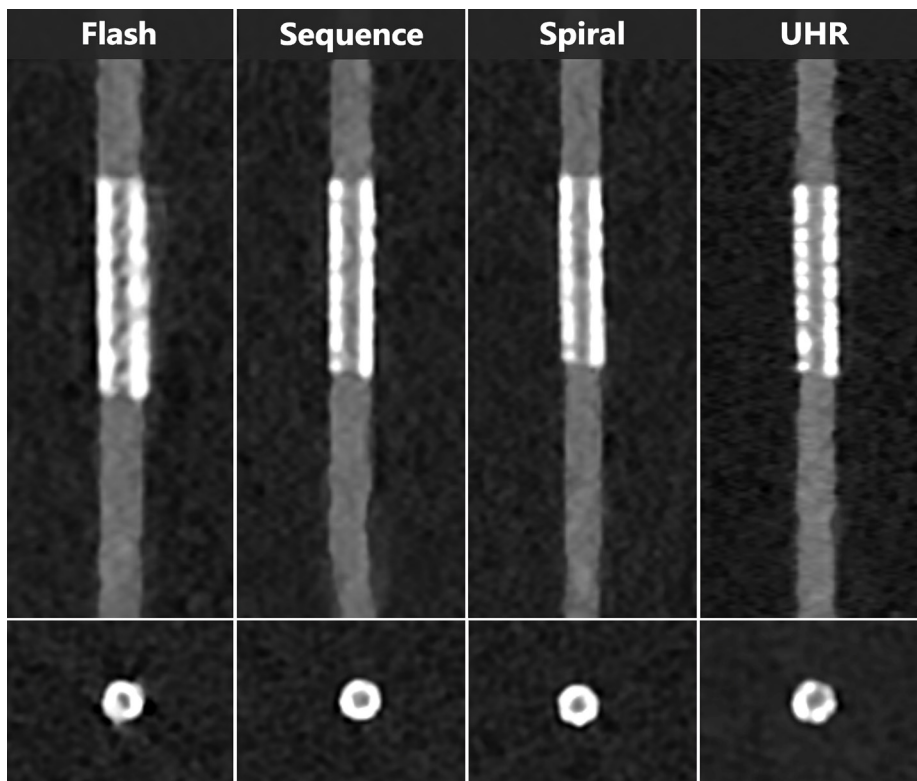
Figure 2. Presents a longitudinal multiparametric reconstruction alongside a transversal section through a stent of 2.00 mm, with a window level of 850 Hounsfield units (HU) and a window width of 2,200 HU. Displayed are, from left to right, four distinct computed tomography (CT) acquisition modes: high-pitch helical CT ("flash"), sequential CT, spiral CT, and ultra-high-resolution (UHR) CT. Image quality was assessed by two independent radiologists, who found the flash CT quality poor due to compromised clarity and artifact interference of the stented lumen. Both sequential and spiral CT images were deemed to have reduced quality, with some loss of detail within the stent lumen. In contrast, the UHR CT image was rated independently as excellent, showcasing exceptional detail and clarity in stent structure and lumen visualization.
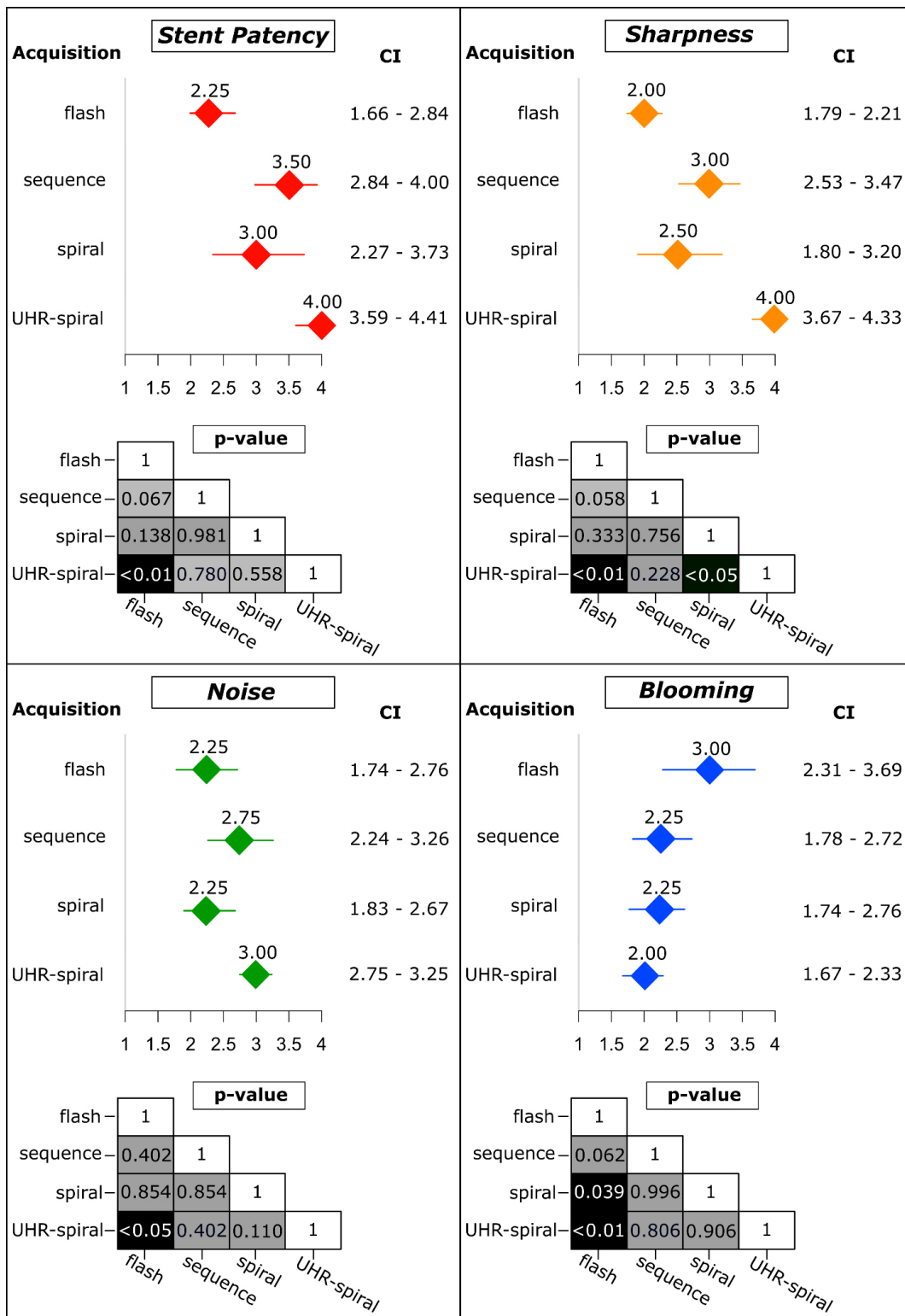
Figure 3. Displays the result of the qualitative analysis for diagnostic confidence of stent patency (upper left), sharpness (upper right), noise (lower left), and blooming artifact interference (lower right). Values were presented as mean and 95% confidence interval ranges (CI). The *P* values were corrected for multiple comparisons using the Bonferroni method. The ultra-high-resolution (UHR)-spiral mode received the highest ratings for stent patency with a mean of 4.00 (CI: 3.59–4.41), and flash mode showed the lowest with a mean of 2.25 (CI: 1.66–2.84). Similarly, sharpness was rated highest in the UHR-spiral mode with a mean of 4.00 (CI: 3.67–4.33). Flash mode registered the lowest sharpness ratings with a mean of 2.00 (CI: 1.79–2.21). Regarding noise, the UHR-spiral mode exhibited the lowest perceived noise levels with a mean of 3.00 (CI: 2.75–3.25), while the sequential mode also displayed comparatively low noise levels with a mean of 2.75 (CI: 2.24–3.26). For blooming effects, the flash mode exhibited the highest with a mean of 3.00 (CI: 2.31–3.69), and the lowest blooming effects were noted in the UHR-spiral mode with a mean of 2.00 (CI: 1.67–2.33).

Table 4. Image quality analysis with analysis of overall image quality, diagnostic confidence, and objective measurements across different computed tomography acquisition modes: overall image quality (median [IQR]), diagnostic confidence (median [IQR]), inner diameter (mm, mean ± SD), outer diameter (mm, mean ± SD), FWHM (mm, mean ± SD), SNR (mean ± SD) and CNR (mean ± SD)

	Flash	Sequential	Spiral	UHR	Overall
Subjective image quality					
Overall image quality†	2 [1–3]	3 [2–4]	3 [2–4]	4 [3–4]	3 [2–4]
Excellent		3	6	9	18 (37.5%)
Good	4	7	3	3	17 (35.4%)
Reduced	5	2	3		10 (20.8%)
Non-diagnostic	3				3 (6.3%)
Objective image quality					
Measured inner diameter (mm)	1.79 ± 0.33	1.81 ± 0.31	1.77 ± 0.35	1.71 ± 0.27	1.8 ± 0.4
Measured outer diameter (mm)	3.02 ± 0.47	3.17 ± 0.38	3.15 ± 0.39	3.15 ± 0.35	3.1 ± 0.5
FWHM (mm)	0.990 ± 0.083	0.926 ± 0.061	0.962 ± 0.085	0.941 ± 0.036	0.947 ± 0.067
Attenuation (avg HU)					
Water*	5.23 ± 57.0	4.64 ± 52.5	6.26 ± 51.5	3.43 ± 43.6	4.89 ± 51.2
Adjacent vessel*	863.5 ± 56.1	857.4 ± 58.5	853.5 ± 59.0	750.7 ± 49.95	831.3 ± 55.9
In-stent lumen*	991.5 ± 140.1	923.1 ± 95.1	928.0 ± 82.5	817.4 ± 83.5	915.0 ± 100.3
Noise (SD HU)					
Water	50.1	49.4	53.4	51.8	51.2 ± 6.6
SNR	11.6 ± 1.8	13.6 ± 1.9	14.0 ± 2.1	13.4 ± 1.7	13.2 ± 2.1
CNR	11.6 ± 1.9	13.5 ± 1.9	13.9 ± 2.1	13.4 ± 1.7	13.1 ± 2.1

†Values correspond to median and interquartile range in square brackets; *Values are presented as mean and standard deviation.
FWHM, full width at half maximum; SNR, signal-to-noise ratio; CNR, contrast-to-noise ratio; avg, average; HU, Hounsfield units; SD, standard deviation; IQR, interquartile range; UHR, ultra-high-resolution.

Table 5. Image quality relative to acquisition mode and stent size

		Stent size (mm)						Image quality
		2.00	2.25	2.50	2.75	3.00	3.50	
Scan mode	Flash							Excellent (n = 18)
	Sequential					1	2	
	Spiral		1	1		2	2	
	UHR	2		2	1	2	2	
	Flash		1		2	1		Good (n = 17)
	Sequential	1	2	1	2	1		
	Spiral		1	1	1			
	UHR		2		1			
	Flash		1	2		1	1	Reduced (n = 10)
	Sequential	1		1				
	Spiral	2			1			
	UHR							
	Flash	2					1	Non-diagnostic (n = 3)
	Sequential							
	Spiral							
	UHR							

Two readers assessed the image quality for various stent sizes across different imaging acquisition protocols. The stents ranged in size from 2.00 to 3.50 mm, with protocols including flash, sequential, spiral, and UHR scan modes. Image quality was rated on a four-point scale from "excellent" to "non-diagnostic." Each entry represents the number of stents that were assigned a particular image quality level by the readers under each protocol and stent size combination. The far-right column denotes the total counts of ratings for each image quality category. UHR, ultra-high resolution.

Table 6. Diagnostic confidence relative to acquisition mode and stent size

		Stent size (mm)						Diagnostic confidence
		2.00	2.25	2.50	2.75	3.00	3.50	
Scan mode	Flash							Excellent (n = 19)
	Sequential		1		2	1	2	
	Spiral			1		2	2	
	UHR	2		2		2	2	
	Flash		1		2	1		Good (n = 15)
	Sequential		1	1		1		
	Spiral		2		2			
	UHR		2		2			
	Flash		1	2		1	1	Reduced (n = 10)
	Sequential	2		1				
	Spiral	1		1				
	UHR							
	Flash	2					1	Poor (n = 4)
	Sequential							
	Spiral	1						
	UHR							

Two readers assessed the diagnostic confidence for various stent sizes across different imaging acquisition protocols. The stents ranged in size from 2.0 to 3.50 mm, with protocols including flash, sequential, spiral, and UHR mode. Diagnostic confidence was rated on a four-point scale from "excellent" to "poor." Each entry represents the number of stents that were assigned a particular confidence level by the readers under each protocol and stent size combination. The far-right column denotes the total counts of ratings for each diagnostic confidence category. UHR, ultra-high resolution.

Signal-to-noise ratio and contrast-to-noise ratio

The SNR values spanned from 11.6 ± 1.8 in flash mode to 14.0 ± 2.1 in spiral mode. Similarly, CNR evaluations illustrated a marginal preference for the spiral mode at 13.9 ± 2.1 over the flash mode, which presented a CNR of 11.6 ± 1.9.

Discussion

Our *ex vivo* phantom study assessed the feasibility and image quality of PCD-CT for evaluating small-sized coronary stents (2.0–3.5 mm internal diameter). We found that PCD-CT is effective for stent imaging, particularly in the UHR mode, which provided superior image quality and diagnostic confidence compared with standard dual-source PCD-CT scan modes. The high-pitch spiral mode was deemed unsuitable for small stent imaging.

A study by Mannil et al.[15], which analyzed larger stents using a dual-source prototype scanner with one detector being an energy-integrating CT and the other using PCD technology, found that PCD technology enhanced stent lumen visibility. In comparative *in vitro* analysis between PCD-CT and EID-scanner systems, superior stent lumen visibility was achieved, particularly in the UHR mode.[16,17] The results of all these studies corroborate our findings.

The objective measures of the FWHM for the sequential and UHR modes underscored its superior robustness, while all acquisition modes provided measurement consistency. In that regard, our study results are in agreement with those of a recent study performed by Koons et al.[18], which shows the least amount of blooming for UHR mode and the use of a sharp kernel. This has been confirmed in a recent clinical study highlighting improved diagnostic performance of coronary stents with optimal in-stent lumen at Bv72 kernels.[19] Subjective assessments of image quality and diagnostic confidence further reinforced the advantages of the UHR mode, with it receiving the highest proportion of "excellent" ratings across all evaluated parameters. Conversely, the high-pitch helical scan mode displayed limitations in accurately depicting smaller stents, suggesting that although it may offer reduced radiation dose,[20] it is not suitable for small-sized stent assessment. This is confirmatory to results reported by Ochs et al.[21], where a noticeable deterioration in image quality was observed in patients with increased coronary calcifications.

While our results indicate a significant potential of UHR PCD-CT in assessing small-sized stents, the implications extend beyond stent evaluation: initial clinical studies indicate high potential in coronary stenosis of stenosis severity,[22] enhanced diagnostic accuracy in challenging cases, and pronounced plaques evaluation.[23-25] It remains to be determined how this advanced technology will impact patient management and outcomes.

This study's limitations include its *ex vivo* nature, which presents challenges for direct clinical application. We focused on different acquisition modes for small-sized stent image quality but did not evaluate the impact of different kernels or iterative reconstruction levels, which have been addressed in previous studies. Additionally, the current scanner software does not support simultaneous UHR–CTA spectral sensitivity with monoenergetic reconstruction, an area needing future research to determine the best imaging approach. In this regard, a recent study investigated the image quality of stents in various 3.00 mm stents UHR-CT with a sharp kernel, and synthetic monoenergetic reconstruction of 55 keV showed promising results.[26] Furthermore, updated scanner versions introduced sequential scanning with UHR. Here, a comparative analysis of diagnostic performance between retrospective
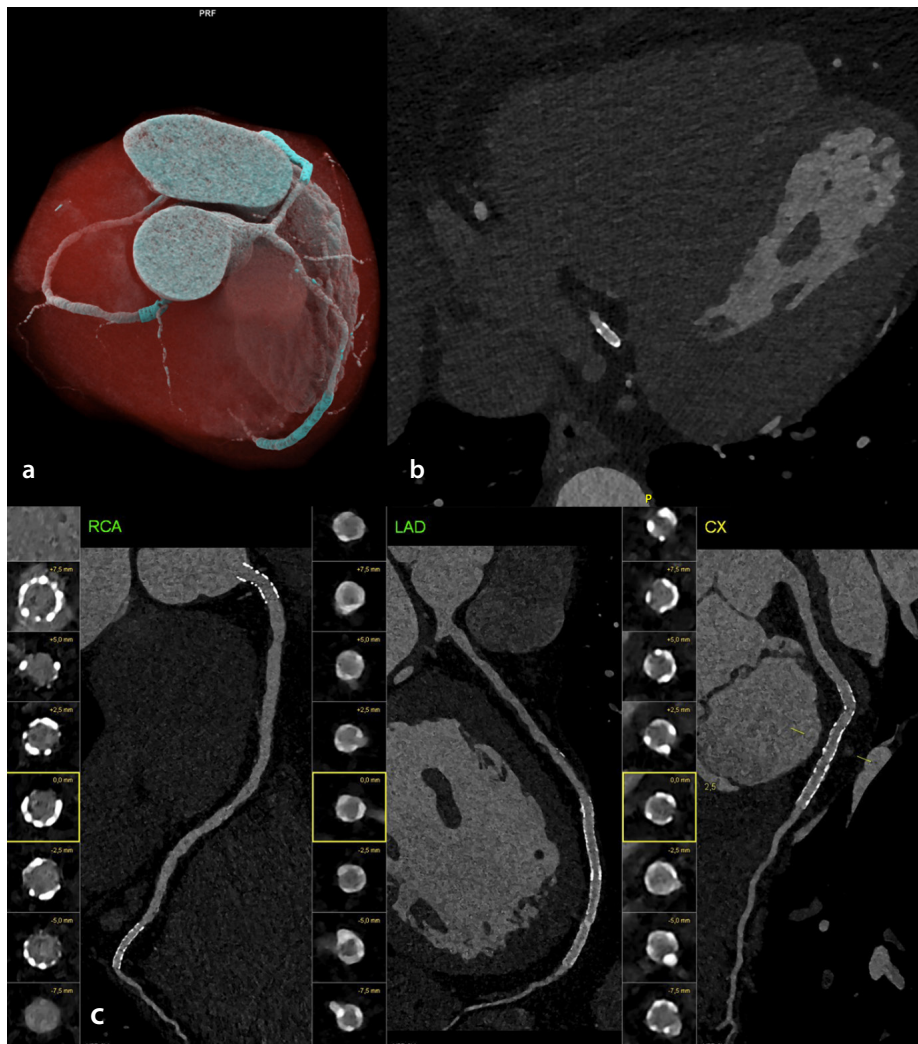
Figure 4. A practical instance of photon-counting detector computed tomography has demonstrated its successful use in a clinical setting for assessing coronary stents. The figure depicts a 48-year-old man with a clinical history of NSTEMI 2 years ago, necessitating emergent coronary stent implantations, as visualized by ultra-high-spatial resolution photon-counting coronary computed tomography angiography. **(a)** Cinematic rendering illustrates the presence of dual stents within the right coronary artery (RCA) and singular stents in the left anterior descending artery (LAD) and left circumflex coronary artery. **(b)** Transversal section depicts the stent at the posterolateral branch of the RCA with an internal diameter of 2.50 mm. **(c)** Curved multiplane reformation of each artery showcases the stent patency and provides superior visualization of the stent lumen for all stents, including the small-sized stent in the distal LAD (2.25 mm) and the posterolateral branch of the RCA (2.00 mm).

and sequential UHR PCD-CT would be insightful.

In conclusion, our *ex vivo* study demonstrates that the UHR mode of PCD-CT offers the best image quality and diagnostic confidence for evaluating small-sized coronary stents. Given that current guidelines do not recommend non-invasive modalities for stents smaller than 3 mm, our findings suggest that PCD-CT could fill this gap, pending validation through dedicated *in vivo* clinical studies.

Conflict of interest disclosure

Fabian Bamberg Siemens Healthineers AG (unrestricted research grant, speaker's bureau), Christopher L. Schlett Siemens Healthineers AG (speaker's bureau), Muhammad Taha Hagar Siemens Healthineers AG (speaker's bureau). Other authors have nothing to disclose.

References

1. Knuuti J. 2019 ESC Guidelines for the diagnosis and management of chronic coronary syndromes The Task Force for the diagnosis and management of chronic coronary syndromes of the European Society of Cardiology (ESC). *Russ J Cardiol*. 2020;25(2):3557. [CrossRef]

2. Gulati M, Levy PD, Mukherjee D, et al. 2021 AHA/ACC/ASE/CHEST/SAEM/SCCT/SCMR Guideline for the Evaluation and Diagnosis of Chest Pain: a report of the American College of Cardiology/American Heart Association Joint Committee on Clinical Practice Guidelines. *Circulation*. 2021;144(22):e368-e454. Erratum in: *Circulation*. 2023;148(24):e281. [CrossRef]

3. Narula J, Chandrashekhar Y, Ahmadi A, et al. SCCT 2021 expert consensus document on coronary computed tomographic angiography: a report of the society of cardiovascular computed tomography. *J Cardiovasc Comput Tomogr*. 2021;15(3):192-217. [CrossRef]

4. Pack JD, Xu M, Wang G, Baskaran L, Min J, De Man B. Cardiac CT blooming artifacts: clinical significance, root causes and potential solutions. *Vis Comput Ind Biomed Art*. 2022;5(1):29. [CrossRef]

5. Gilard M, Cornily JC, Pennec PY, et al. Assessment of coronary artery stents by 16 slice computed tomography. *Heart*. 2006;92(1):58-61. [CrossRef]

6. Mergen V, Sartoretti T, Baer-Beck M, et al. Ultra-High-Resolution Coronary CT angiography with photon-counting detector CT: feasibility and image characterization. *Invest Radiol*. 2022;57(12):780-788. [CrossRef]

7. Boccalini S, Si-Mohamed SA, Lacombe H, et al. First in-human results of computed tomography angiography for coronary stent assessment with a spectral photon counting computed tomography. *Invest Radiol*. 2022;57(4):212-221. [CrossRef]

8. Geering L, Sartoretti T, Mergen V, et al. First in-vivo coronary stent imaging with clinical ultra high resolution photon-counting CT. *J Cardiovasc Comput Tomogr*. 2023;17(3):233-235. [CrossRef]

9. Decker JA, O'Doherty J, Schoepf UJ, et al. Stent imaging on a clinical dual-source photon-counting detector CT system-impact of luminal attenuation and sharp kernels on lumen visibility. *Eur Radiol*. 2023;33(4):2469-2477. [CrossRef]

10. Hagar MT, Soschynski M, Saffar R, et al. Ultra-high-resolution photon-counting detector CT in evaluating coronary stent patency: a comparison to invasive coronary angiography. *Eur Radiol.* 2024;34(7):4273-4283. [CrossRef]

11. Stein T, Taron J, Verloh N, et al. Photon-counting computed tomography of coronary and peripheral artery stents: a phantom study. *Sci Rep.* 2023;13(1):14806. [CrossRef]

12. McCollough C, Bakalyar DM, Bostani M, et al. Use of water equivalent diameter for calculating patient size and size-specific dose estimates (SSDE) in CT: the report of AAPM Task Group 220. *AAPM Rep.* 2014;2014:6-23. [CrossRef]

13. Leschka S, Kim CH, Baumueller S, et al. Scan Length Adjustment of CT coronary angiography using the calcium scoring scan: effect on radiation dose. *AJR Am J Roentgenol.* 2010;194(3):272-277. [CrossRef]

14. Hagar MT, Soschynski M, Benndorf M, et al. Enhancing radiation dose efficiency in prospective ECG-triggered coronary CT angiography using calcium-scoring CT. *Diagnostics (Basel).* 2023;13(12):2062. [CrossRef]

15. Mannil M, Hickethier T, von Spiczak J, et al. Photon-counting CT: high-resolution imaging of coronary stents. *Invest Radiol.* 2018;53(3):143-149. [CrossRef]

16. Symons R, De Bruecker Y, Roosen J, et al. Quarter-millimeter spectral coronary stent imaging with photon-counting CT: Initial experience. *J Cardiovasc Comput Tomogr.* 2018;12(6):509-515. [CrossRef]

17. Petritsch B, Petri N, Weng AM, et al. Photon-counting computed tomography for coronary stent imaging: in vitro evaluation of 28 coronary stents. *Invest Radiol.* 2021;56(10):653-660. [CrossRef]

18. Koons EK, Thorne JE, Huber NR, et al. Quantifying lumen diameter in coronary artery stents with high-resolution photon counting detector CT and convolutional neural network denoising. *Med Phys.* 2023;50(7):4173-4181. [CrossRef]

19. Qin L, Zhou S, Dong H, et al. Improvement of coronary stent visualization using ultra-high-resolution photon-counting detector CT. *Eur Radiol.* 2024. [CrossRef]

20. Rajiah PS, Dunning CAS, Rajendran K, et al. High-Pitch Multienergy Coronary CT angiography in dual-source photon-counting detector CT scanner at low iodinated contrast dose. *Invest Radiol.* 2023;58(9):681-690. [CrossRef]

21. Ochs MM, Andre F, Korosoglou G, et al. Strengths and limitations of coronary angiography with turbo high-pitch third-generation dual-source CT. *Clin Radiol.* 2017;72(9):739-744. [CrossRef]

22. Halfmann MC, Bockius S, Emrich T, et al. Ultrahigh-spatial-resolution photon-counting detector CT angiography of coronary artery disease for stenosis assessment. *Radiology.* 2024;310(2):e231956. [CrossRef]

23. Mergen V, Eberhard M, Manka R, Euler A, Alkadhi H. First in-human quantitative plaque characterization with ultra-high resolution coronary photon-counting CT angiography. *Front Cardiovasc Med.* 2022;9:981012. [CrossRef]

24. Hagar MT, Soschynski M, Saffar R, et al. Accuracy of ultrahigh-resolution photon-counting CT for detecting coronary artery disease in a high-risk population. *Radiology.* 2023;307(5):e223305. [CrossRef]

25. Eberhard M, Candreva A, Rajagopal R, et al. Coronary stenosis quantification with ultra-high-resolution photon-counting detector CT angiography. *JACC Cardiovasc Imaging.* 2024;17:342-344. [CrossRef]

26. Elias Michael A, Schoenbeck D, Michael Woeltjen M. Photon counting computed tomography of in-stent-stenosis in a phantom: Optimal virtual monoenergetic imaging in ultra high resolution. *Heliyon.* 2024;10(6):e27636. [CrossRef]

INTERVENTIONAL RADIOLOGY

ORIGINAL ARTICLE

Endovascular recanalization of infra-popliteal TASC C and TASC D lesions in patients with critical limb-threatening ischemia: a single-center experience

Mehmet Koray Akkan[1]
Ali Can Yalçın[2]
Tolga Zeydanlı[3]
Fatih Öncü[1]
Erhan Turgut Ilgıt[1]
Ahmet Baran Önal[1]
Mustafa Hakan Zor[4]
Abdullah Özer[4]

[1]Gazi University Faculty of Medicine, Department of Radiology, Ankara, Turkey

[2]Konya City Hospital, Clinic of Radiology, Konya, Turkey

[3]Başkent University Ankara Hospital, Department of Radiology, Ankara, Turkey

[4]Gazi University Faculty of Medicine, Department of Cardiovascular Surgery, Ankara, Turkey

PURPOSE

The present study aims to (1) assess the technical success and limb salvage rates of endovascular therapy in patients with critical limb-threatening ischemia (CLTI) and infra-popliteal Trans-Atlantic Inter-Society Consensus (TASC) C/D lesions according to the updated 2015 TASC II classification and (2) to present our institutional experience.

METHODS

A single-center retrospective study was conducted on patients with TASC C/D CLTI who underwent endovascular treatment between 2012 and 2017. The follow-up protocol consisted of Doppler ultrasound conduction every 3 months for the first year unless patients showed symptoms of CLTI. Patients with at least 1 year of follow-up data were included in the study, and if applicable their 3-year results were evaluated in terms of primary patency, absence of amputation, amputation-free survival, and overall survival.

RESULTS

A total of 248 patients and 287 limbs (238 TASC D lesions and 49 TASC C lesions) were treated via infra-popliteal percutaneous transluminal angioplasty. The overall technical success was 87%, the primary patency rate was 41.5% in the first year, and the freedom from amputation rates were 80.8% in 1 year and 67.7% in 3 years.

CONCLUSION

In patients with infra-popliteal arterial occlusive diseases, endovascular treatment methods demonstrate a high rate of technical success and favorable outcomes in limb preservation.

KEYWORDS

Percutaneous angioplasty, infra-popliteal arteries, critical limb ischemia, TASC

Corresponding author: Tolga Zeydanlı

E-mail: tz.tolga@gmail.com

Infra-popliteal arterial disease constitutes a substantial contributor to critical limb-threatening ischemia (CLTI); it is also closely associated with elevated rates of limb amputation and mortality. CLTI is marked by (1) a presence of persistent ischemic pain at rest or (2) tissue loss, typically occurring in the distal parts of the lower extremities.[1-4] Surgical revascularization of CLTI for limb salvage is a known traditional treatment option; however, an increasing number of centers are treating patients with CLTI via endovascular procedures as the first approach. With the development of small-size stents, low profile balloon catheters, hydrophilic guidewires, support catheters, recanalization devices, and vasodilators, the endovascular approach for infra-popliteal arterial occlusive disease is becoming increasingly common.[5-7] Surgical methods carry an elevated risk of systemic and local complications attributable to the presence of multiple comorbidities.[8]

CLTI is defined as a Rutherford 4, 5 and 6 disease (ischemic rest pain; nonhealing ulcer/gangrene with minor tissue loss and major tissue loss),[9] and Trans-Atlantic Inter-Society Consensus (TASC) D lesions are characterized as occlusions within the target tibial artery, with a total lesion length of >10 cm, substantial lesion calcification, or a lack of collateral visualization. Additionally, it includes cases where the other tibial arteries are occluded or densely calcified. The TASC C lesions, on the other hand, are defined as stenoses within the target tibial artery or an occlusion with a total lesion length of 10 cm. They also encompass occlusion or stenosis of a comparable or relatively severe degree in the other tibial arteries.[10]

In the literature, significant heterogeneity is evident in studies investigating endovascular treatment outcomes of infra-popliteal artery occlusions.[11] The present study aims to share its authors' institutional experience regarding the endovascular treatment of infra-popliteal arterial occlusive disease in patients with CLTI, as per the revised TASC II classification. Furthermore, it seeks to assess the technical success and limb salvage rates specifically for TASC C and D lesions in endovascular treatment.

Methods

The present study was conducted with adherence to the principles outlined in the Declaration of Helsinki Good Clinical Practice guidelines and was approved by the Gazi University Ethical Committee (date: 12/2019, reference number: 286). Patient consent was waived.

A retrospective analysis was conducted on all consecutive patients diagnosed with CLTI who underwent an endovascular intervention for revascularization of TASC C/D infra-popliteal lesions between January 2012 and September 2017. Patients with at

---

Main points

- Infra-popliteal arterial disease is a major cause of critical limb-threatening ischemia (CLTI) and it is associated with high rates of limb loss and mortality.

- Challenging infra-popliteal arterial lesions can be treated via endovascular approaches with low complication rates.

- Endovascular treatment methods are effective and reliable in alleviating symptoms associated with CLTI and in preventing limb loss in cases involving challenging infra-popliteal arterial lesions.

---

least 1 year of follow-up data were enrolled in the study, and if applicable the 3-year outcomes of these patients were evaluated. Demographic details and follow-up data were collected from Gazi University digital medical records database. Technical success was defined as the achievement of successful revascularization, characterized by <50% residual stenosis following angioplasty and the absence of flow-limiting dissection. Baseline angiograms of the whole limb were obtained for comparison purposes.

In all patients, the preferred initial approach involved ipsilateral antegrade access through the common femoral artery and subsequent revascularization. Following the ultrasound-guided puncture of the common femoral artery, a 6-Fr peripheral guiding sheath (Destination, Terumo) was placed in the distal superficial femoral or popliteal artery to reduce contrast media administration and for better catheter support and guidewire control. The study authors tried to cross all the occluded segments with a 0.014-inch hydrophilic-tipped guide wire (V14, Boston Scientific Corporation) with a compatible support catheter (Seeker, Bard; TrailBlazer, eV3). If these methods failed, the authors tried to cross the arterial occlusion with more supportive 0,018-inch guide wires (V18, Boston Scientific Corporation) and a compatible support catheter (Seeker, Bard; TrailBlazer, eV3). In cases with failed antegrade crossing attempts, retrograde pedal artery access under ultrasound guidance with a pedal access kit (Cook Medical Inc.) or atherectomy catheter (Crosser, Bard) were used. After crossing the occlusion from retrograde pedal access, the wire was snared from or inserted into the femoral access sheath, and the procedure continued from the antegrade approach. The occluded segments crossed with a guidewire and a support catheter, and these segments were dilated with an appropriately sized low-profile balloon catheter. Balloon catheters with a diameter of 2–4.5 mm were inflated for 60 s at 6–8 atm. If there was a suboptimal result or flow-limiting dissections, further dilatation was performed for an additional 2 min or the occluded segment was dilated with a balloon 0.5 mm larger in diameter. Bail-out stenting (Ephesos II, Alvimedica) was performed in lesions due to persistent flow-limiting dissections or immediate post-angioplasty recoiling. A final angiogram was performed to reveal the result, including the pedal arteries (Figure 1).

During the procedure, 5000 IU intravenous heparin was administered to all patients except those with renal failure, who received

2500 IU heparin following the insertion of the arterial sheath. Dual antiplatelet therapy of clopidogrel (75 mg/day) and acetylsalicylic acid (ASA) (100 mg/day) were recommended 3 days before the procedure and resumed for 6 months. Lifelong treatment with ASA was continued. After the intervention, 4000 anti-Xa units of low-molecular-weight heparin were recommended twice daily for 5 days.

The authors' follow-up protocol included Doppler ultrasound (DUS) imaging at discharge at the first month and every 3 months thereafter for the first year. The first-year control interval then increased to every 6 months unless patients presented with symptoms of CLTI. Follow-up angiography and/or re-intervention was considered when the DUS findings suggested restenosis of >50% (with a Rutherford score of >4 and no wound healing).

Statistical analysis

Data analysis was performed using the Statistical Package for the Social Sciences (IBM, SPSS Statistics for Macintosh, Version 25.0, Armonk, New York). Continuous variables were represented as mean ± standard deviation, and categorical variables were de-

Figure 1. Pre-angioplasty images show occlusion of all crural arteries (arrows). Reconstitution of the tibial arteries are visible distally (arrowheads). The anterograde approach was performed, and recanalization was achieved in the posterior tibial artery (PTA) but not in the anterior tibial artery (ATA). The distal ATA was punctured, and retrograde access was gained (small arrow). Next, anterograde access was gained using the rendezvous technique, and successful recanalization and balloon angioplasty of the ATA was accomplished (star). The final angiogram shows successful recanalization and patency of both ATA and PTA.

picted as values along with their respective percentages. Each patient's demographic and comorbidity details were recorded, and patency data were calculated for each individual. Outcomes regarding major amputation and mortality rates in the patient cohort were visualized via Kaplan–Meier analysis.

Results

Between 2012 and 2017, 1,244 patients were treated at Gazi University Hospital for peripheral arterial disease. Patients with isolated infra-popliteal lesions were included in the study; among them, 380 had infra-popliteal TASC C/D lesions, and only 248 patients had complete 1-year follow-up data and were enrolled in the study.

A total of 238 TASC D and 49 TASC C lesions were treated in the 248 patients. In 95 of the patients, more than one infra-popliteal artery was treated. A total of 190 patients were men (76.6%), and the mean age was 65.3 years. Patient characteristics are given in Table 1. A total of 190 patients (76.6%) had diabetes mellitus, 183 (73.7%) had hypertension, and 39.9% had coronary artery disease.

Risk factors are also noted in Table 1. According to the Rutherford classification, 38 of the patients (13.2%) fell into category 4, 172 (59.9%) fell into category 5, and 77 (26.8%) fell into category 6. Treated occlusions were 10–30 cm long, and the average occlusion length was 15.7 ± 0.2 cm. Detailed lesion characteristics are given in Table 2.

In 203 of the lesions (71%), recanalization was successful with standard guidewires and support catheters via anterograde access. In the remaining 48 (16%) lesions, retrograde pedal access was needed to cross the occluded segment. In 29 (10%) lesions, atherectomy devices were used. A total of 7 (3%) lesions required use of both pedal access and atherectomy devices. In 33 and 23 patients, the anterior tibial artery and posterior tibial artery, respectfully, were punctured under ultrasound guidance with a pedal access set. However, in 6 of the lesions, all attempts at recanalization were unsuccessful. The overall

occlusion crossing success rate was 97.9%. After balloon dilatation, a result of suboptimal angioplasty or flow-limiting dissection was seen in 57 (19.8%) lesions. In 20 (6.9%) additional lesions, successful revascularization was achieved after repeated balloon dilatations for an additional 2 min at nominal pressure. In 6 lesions (2%) a persistent flow-limiting dissection was noticed, and bail-out stenting was performed. Despite all attempts, adequate vessel patency was not achieved in 37 (12.8%) of the lesions.

The procedure was technically successful in 87.2% of lesions. In the follow up, the Rutherford score improved to 3.3 ± 0.4 in the first year. The primary patency rate was 65.2% at 3 months and declined to 41.5% at 12 months (Figure 2). At 1 year, a total of 67 (23.3%) limbs required re-intervention; among them, 12 (4.8%) were referred for by-pass surgery. Amputations above the ankle level were accepted as major amputation,

Table 1. Baseline characteristics	
Characteristic	Value
Patients (n)	248
Limbs (n)	287
Male gender	190/248 (76.6%)
Diabetes mellitus	190/248 (76.6%)
Hypertension	183/248 (73.7%)
Smoking	184/248 (74.6%)
Hyperlipidemia	102/248 (41.1%)
CAD	99/248 (39.9%)
ESRD	21/248 (8.5%)
CAD, coronary artery disease; ESRD, end-stage renal disease.	
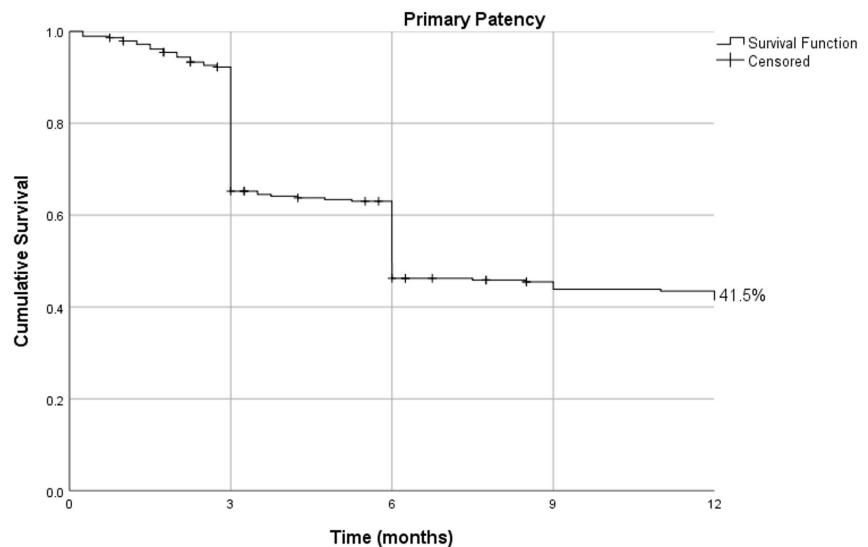
Figure 2. Kaplan–Meier curve for primary patency.

Table 2. Lesion characteristics					
		Rutherford			
		4	5	6	Total
TASC	C	28	16	5	49 (17.1%)
	D	10	156	72	238 (82.9%)
Total		38 (13.2%)	172 (59.9%)	77 (26.8%)	
Lesion length			15.7 ± 0.2		
Vessel diameter			2.92 ± 0.3		
Lesion location					
Anterior tibial artery			191		
Posterior tibial artery			130		
Peroneal artery			62		
TASC, Trans-Atlantic Inter-Society Consensus.					

and at 12 months, 25 (8.6%) limbs had undergone major amputation, and 32 (11.1%) limbs had undergone minor amputation. Over the 3-year follow-up period, 40 (13.9%) limbs had undergone major amputation, and 40 (13.9%) limbs had undergone minor amputation. The amputation-free survival rates were 70.7% at the first year and 32.9% at the third year (Figure 3). A total of 30 patients (12%) died during 12 months of the follow up, and 117 (47.1%) died over 3 years (Figure 4). Freedom from amputation was 80.8% at the first year and 67.7% at 3 years (Figure 5).

There were no procedure-related deaths in the first month after the procedure. There were 9 major complications (3.6%), including 4 pseudoaneurysms and 5 persistent flow-limiting dissections at the puncture site, which were treated accordingly. There were 21 minor complications, such as a small hematoma at the puncture site.

Discussion

This study presents the 3-year outcomes of patients diagnosed with CLTI who received endovascular interventions to address infra-popliteal lesions categorized as TASC C and TASC D. Percutaneous revascularization of infra-popliteal lesions was performed with an 87.2% technical success rate and a low major adverse events rate (3.6%).

The success of the revascularization procedure was assessed by evaluating the patency rates and clinical endpoints, including amputation-free survival. The occurrence of restenosis (>50%) poses a significant challenge. The present authors' primary approach always centered on reducing rest pain and amputation rates, coupled with vigilant post-intervention follow up to achieve these goals.

The effectiveness of the endovascular approach for treating infra-popliteal arterial lesions remains uncertain and not yet firmly established.[12] For the treatment of CLTI, both bypass surgery and endovascular revascularization are viable options, each demonstrating favorable limb salvage rates.[13] Although venous bypass surgery seems to have a higher durability, many patients with CLTI are not suitable for surgery due to comorbidities. Endovascular treatment stands as a less invasive, efficient, and secure therapeutic choice that can be carried out under local anesthesia.[14] Despite a general trend toward initially adopting the endovascular approach for all patients with CLTI, surgical revascularization for infra-popliteal lesions in CLTI cases is still commonly observed.[15]

Figure 3. Kaplan–Meier curve for amputation-free survival.

Figure 4. Kaplan–Meier curve for overall survival.

Figure 5. Kaplan–Meier curve for freedom from amputation.
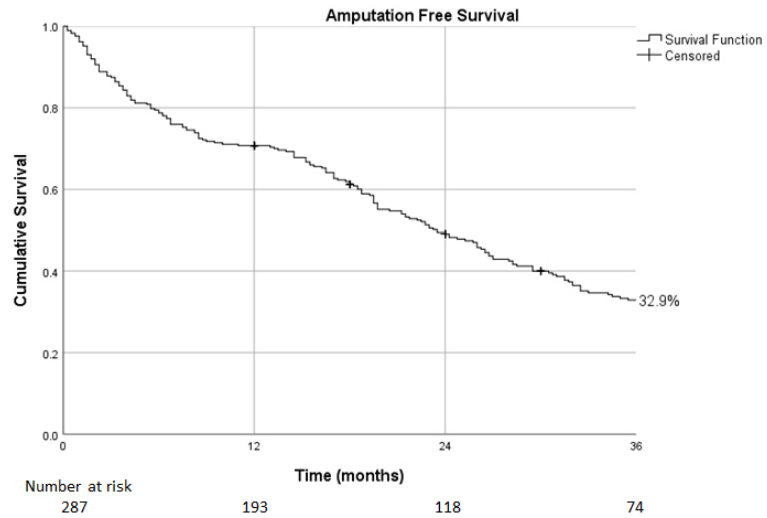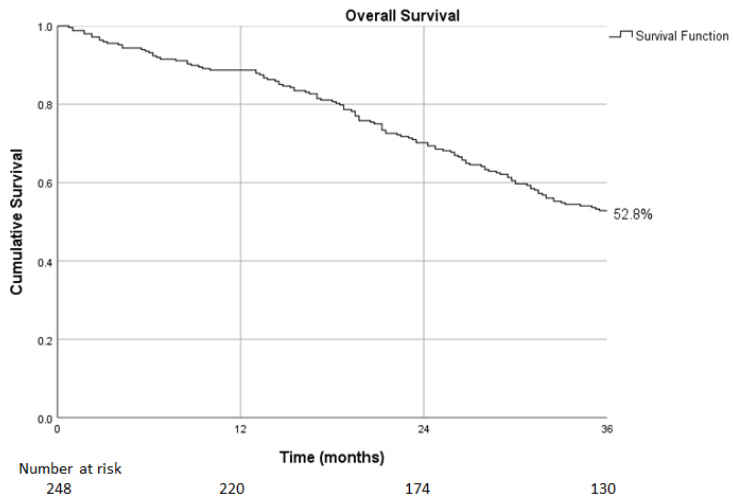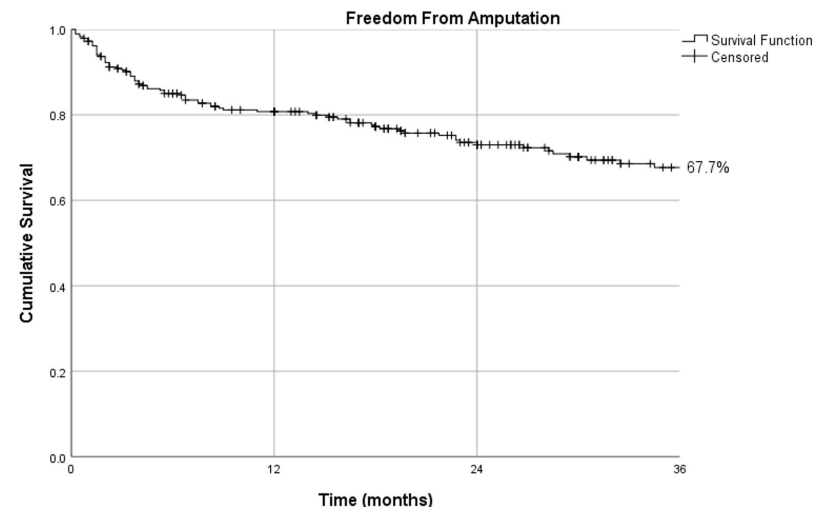
Table 3. Published endovascular treatment reports of infra-popliteal arterial disease in patients with CLI or TASC C/D lesions in the literature

Author	Number of patients	Technical success	Primary patency rate at 1 year	Limb salvage rates at 1 year	Amputation-free survival at 1 year
Present study	248	87.2%	41.5%	80.8%	70.7%
Singh et al.[17]	94	80%	51%	74%	57%
Pavé et al.[18]	139	87.9%	55%	81%	NA
Nakano et al.[19]	449	71%	NA	77%	51%
Kok et al.[20]	112	75%	NA	77%	NA

CLI, critical limb ischemia; TASC, Trans-Atlantic Inter-Society Consensus; NA, not available.

In a single-center study, complex infra-popliteal lesions had poorer outcomes compared with moderate lesions over long-term outcomes.[16] In a separate study, the TASC C/D lesions were linked with a lower rate of procedural success, higher incidence of major amputations, and poorer primary patency. This was attributed to the fact that these small vessel lesions tend to be significantly longer and are more frequently characterized as chronic occlusions.[17] While the present technical success rate of 87.2% appears comparable with the mentioned study, it is important to note that in the present study, all the lesions were occlusions with a length of >10 cm.

Recent reports for endovascular treatment of CLTI have high limb salvage rates of,[18-20] which is similar to the results of the present study. The present findings revealed high technical success rates in the treatment of infra-popliteal occlusions via balloon angioplasty following crossing with a guidewire and a compatible support catheter via the antegrade access. Furthermore, the use of pedal access safely increases the recanalization rates in infra-popliteal occlusions when the traditional antegrade approach fails.[21]

In the endovascular treatment of infra-popliteal lesions, a high rate of restenosis is expected, especially if the lesions are long-segment occlusions.[22,23] In a series of 139 patients with CLTI treated via angioplasty, the restenosis rate reached 45.3% at 1 year.[22] In another study, Schmidt et al.[23] reported 77 infra-popliteal arterial interventions with long-segment disease, where 65% of the lesions were occlusions. The 3-month angiography follow up showed >50% restenosis or re-occlusion, and despite these rates, clinical findings in 76% of the patients with CLTI had improved. In another infra-popliteal interventional revascularization study, Nakano et al.[19] investigated 449 patients with CLTI who also had end-stage renal disease, demonstrating a 77% limb salvage rate (Table 3).[24]

In the present study, the endovascular approach was used as the first-line treatment. The majority of the patients were not eligible for surgical treatment due to comorbidities or unavailability of distal vessels for bypass surgery. In the follow up, 13.9% limbs had undergone major amputation and 13.9% had undergone minor amputation. Although the prognosis for TASC C and D lesions is poor, the mean Rutherford score improved from 5.13 ± 0.6 to 3.3 ± 0.4 at the 12th month after endovascular treatment.

An improved Rutherford score and wound healing in some patients were observed even after restenosis and re-occlusion in target arteries. Infra-popliteal interventions have high rates of restenosis in patients with CLTI but less clinical importance in wound healing and rest pain, as the aim of these interventions is to provide more arterial perfusion pressure for the non-healing tissue at least for a certain time.[25] To obtain better perfusion pressure, multilevel interventions are thought to be more beneficial than only treating a target vessel or isolated lesion.[26] Thus, the authors aimed to revascularize as many vessels as possible.

The present study has some limitations. First, due to the lack of a surgical counterpart in this study, it is difficult to draw firm conclusions regarding the role of endovascular therapies in the treatment strategies of patients with CLTI. Second, given that the present paper is a retrospective study from a single center targeting only selected patients, it might not reflect the patient characteristics of the whole target population.

In conclusion, this study has shown that endovascular treatment of TASC C/D lesions can be accomplished with a high rate of technical success and a low incidence of complications. Based on this data, the authors believe that endovascular treatment can be used as a first-line treatment with high limb salvage and primary patency rates in the treatment of infra-popliteal occlusion. Further randomized cohort studies should

be performed to promote the success rates of endovascular treatment in infra-popliteal TASC C and D lesions.

Conflict of interest disclosure

The authors declared no conflicts of interest.

References

1. Murabito JM, Evans JC, Nieto K, Larson MG, Levy D, Wilson PW. Prevalence and clinical correlates of peripheral arterial disease in the Framingham Offspring Study. *Am Heart J*. 2002;143(6):961-965. [CrossRef]

2. Criqui MH, Langer RD, Fronek A, et al. Mortality over a period of 10 years in patients with peripheral arterial disease. *N Engl J Med*. 1992;326(6):381-386. [CrossRef]

3. Stoyioglou A, Jaff MR. Medical treatment of peripheral arterial disease: a comprehensive review. *J Vasc Interv Radiol*. 2004;15(11):1197-207. [CrossRef]

4. Abu Dabrh AM, Steffen MW, Undavalli C, et al. The natural history of untreated severe or critical limb ischemia. *J Vasc Surg*. 2015;62(6):1642-1651.e3. [CrossRef]

5. van Overhagen H, Spiliopoulos S, Tsetis D. Below-the-knee interventions. *Cardiovasc Intervent Radiol*. 2013;36(2):302-311. [CrossRef]

6. Hicks CW, Najafian A, Farber A, et al. Below-knee endovascular interventions have better outcomes compared to open bypass for patients with critical limb ischemia. *Vasc Med*. 2017;22(1):28-34. [CrossRef]

7. Taylor SM, Kalbaugh CA, Blackhurst DW, Kellicut DC, Langan EM 3rd, Youkey JR. A comparison of percutaneous transluminal angioplasty versus amputation for critical limb ischemia in patients unsuitable for open surgery. *J Vasc Surg*. 2007;45(2):304-310;discussion310-311. [CrossRef]

8. Norgren L, Hiatt WR, Dormandy JA, Nehler MR, Harris KA, Fowkes FG; TASC II Working Group. Inter-Society Consensus for the Management of Peripheral Arterial Disease (TASC II). *J Vasc Surg*. 2007;45(Suppl S):S5-67. [CrossRef]

9. Stoner MC, Calligaro KD, Chaer RA, et al. Reporting standards of the Society for Vascular

Surgery for endovascular treatment of chronic lower extremity peripheral artery disease. *J Vasc Surg*. 2016;64(1):e1-e21. [CrossRef]

10. Jaff MR, White CJ, Hiatt WR, et al. An update on methods for revascularization and expansion of the TASC lesion classification to include below-the-knee arteries: a supplement to the inter-society consensus for the management of peripheral arterial disease (TASC II). *Vasc Med*. 2015;20(5):465-478. [CrossRef]

11. Mustapha JA, Finton SM, Diaz-Sandoval LJ, Saab FA, Miller LE. Percutaneous transluminal angioplasty in patients with infrapopliteal arterial disease: systematic review and meta-analysis. *Circ Cardiovasc Interv*. 2016;9(5):e003468. [CrossRef]

12. Popplewell MA, Davies HOB, Narayanswami J, et al. A comparison of outcomes in patients with infrapopliteal disease randomised to vein bypass or plain balloon angioplasty in the bypass vs. angioplasty in severe ischaemia of the leg (BASIL) trial. *Eur J Vasc Endovasc Surg*. 2017;54(2):195-201. [CrossRef]

13. Adam DJ, Beard JD, Cleveland T, et al. Bypass versus angioplasty in severe ischaemia of the leg (BASIL): multicentre, randomised controlled trial. *Lancet*. 2005;366(9501):1925-1934. [CrossRef]

14. Giles KA, Pomposelli FB, Spence TL, et al. Infrapopliteal angioplasty for critical limb ischemia: relation of TransAtlantic InterSociety Consensus class to outcome in 176 limbs. *J Vasc Surg*. 2008;48(1):128-136. [CrossRef]

15. Casella IB, Brochado-Neto FC, Sandri Gde A, et al. Outcome analysis of infrapopliteal percutaneous transluminal angioplasty and bypass graft surgery with nonreversed saphenous vein for individuals with critical limb ischemia. *Vasc Endovascular Surg*. 2010;44(8):625-632. [CrossRef]

16. Müller AM, Räpple V, Bradaric C, et al. Outcomes of endovascular treatment for infrapopliteal peripheral artery disease based on the updated TASC II classification. *Vasc Med*. 2021;26(1):18-25. [CrossRef]

17. Singh GD, Brinza EK, Hildebrand J, et al. Midterm outcomes after infrapopliteal interventions in patients with critical limb ischemia based on the TASC II classification of below-the-knee arteries. *J Endovasc Ther*. 2017;24(3):321-330. [CrossRef]

18. Pavé M, Benadiba L, Berger L, Gouicem D, Hendricks M, Plissonnier D. Below-the-knee angioplasty for critical limb ischemia: Results of a Series of 157 procedures and impact of the angiosome concept. *Ann Vasc Surg*. 2016;36:199-207. [CrossRef]

19. Nakano M, Hirano K, Yamauchi Y, et al. Three-year clinical outcome after infrapopliteal angioplasty for critical limb ischemia in hemodialysis patients with minor or major tissue loss. *Catheter Cardiovasc Interv*. 2015;86(2):289-298. [CrossRef]

20. Kok HK, Asadi H, Sheehan M, McGrath FP, Given MF, Lee MJ. Outcomes of infrapopliteal angioplasty for limb salvage based on the updated TASC II classification. *Diagn Interv Radiol*. 2017;23(5):360-364. [CrossRef]

21. Sabri SS, Hendricks N, Stone J, Tracci MC, Matsumoto AH, Angle JF. Retrograde pedal access technique for revascularization of infrainguinal arterial occlusive disease. *J Vasc Interv Radiol*. 2015;26(1):29-38. [CrossRef]

22. Iida O, Soga Y, Kawasaki D, et al. Angiographic restenosis and its clinical impact after infrapopliteal angioplasty. *Eur J Vasc Endovasc Surg*. 2012;44(4):425-431. [CrossRef]

23. Schmidt A, Ulrich M, Winkler B, et al. Angiographic patency and clinical outcome after balloon-angioplasty for extensive infrapopliteal arterial disease. *Catheter Cardiovasc Interv*. 2010;76(7):1047-1054. [CrossRef]

24. Conrad MF, Crawford RS, Hackney LA, et al. Endovascular management of patients with critical limb ischemia. *J Vasc Surg*. 2011;53(4):1020-1025. [CrossRef]

25. Romiti M, Albers M, Brochado-Neto FC, Durazzo AE, Pereira CA, De Luccia N. Meta-analysis of infrapopliteal angioplasty for chronic critical limb ischemia. *J Vasc Surg*. 2008;47(5):975-981. [CrossRef]

26. Sadek M, Ellozy SH, Turnbull IC, Lookstein RA, Marin ML, Faries PL. Improved outcomes are associated with multilevel endovascular intervention involving the tibial vessels compared with isolated tibial intervention. *J Vasc Surg*. 2009;49(3):638-643; discussion 643-644. [CrossRef]

Staged angioplasty using a full-length balloon catheter to achieve maturation of arteriovenous fistulas

 Miju Bae[1,2]
 Chang Ho Jeon[3]
 Sung Woon Chung[1,2]
 Chung Won Lee[1,2]
 Up Huh[1,2]
 Jongwon Kim[2]
 Hyuncheol Jeong[2]

[1]Pusan National University School of Medicine, Department of Thoracic and Cardiovascular Surgery, Yangsan, Republic of Korea

[2]Pusan National University Hospital, Biomedical Research Institute, Department of Thoracic and Cardiovascular Surgery, Busan, Republic of Korea

[3]The Catholic University of Korea, College of Medicine, Eunpyeong St. Mary's Hospital, Department of Radiology, Seoul, Republic of Korea

Corresponding author: Chang Ho Jeon, MD, PhD

E-mail: changho.jeon@gmail.com

PURPOSE

To evaluate the efficacy of staged full-length balloon-assisted maturation (BAM) for the maturation of arteriovenous fistulas (AVFs) on entire segmental veins, including stenosis, causing primary AVF failure.

METHODS

This study included patients who underwent AVF surgery using an autogenous vein between February 2020 and June 2021 and received staged angioplasty with a full-length balloon catheter. To minimize balloon overlap and the risk of barotrauma to the immature vein, serial-staged upsizing balloon angioplasty with a long balloon catheter covering the entire vein segment was employed approximately 2 weeks apart.

RESULTS

Twenty-three patients (mean age, 69.50 years; mean follow-up, 620.62 days) with average diameters of the radial artery and cephalic vein at 2.14 ± 0.5 mm and 2.43 ± 0.5 mm, respectively, were enrolled. In the first procedure, the average AVF diameter and flow were 4.03 ± 0.57 mm and 438.08 ± 220.95 mL/min, respectively, with juxta-anastomotic stenosis (JAS) present in 61.5% of cases. After staged full-length BAM, the average fistula diameter and flow improved to 5.95 ± 0.86 mm and 717.52 ± 305.95 mL/min, respectively. Maturation was achieved in 87% of the cases. No hematomas or ruptures occurred around the arterialized veins. Despite successful maturation and cannulation, 65.2% of the patients required additional percutaneous transluminal angioplasty (PTA) during the follow-up period. The necessity for PTA was determined by the presence of JAS prior to the first staged full-length BAM, with an odds ratio of 11.74 (95% confidence interval: 1.31–104.96, $P = 0.03$).

CONCLUSION

Staged full-length BAM can be safely used in patients with small veins requiring further maturation. Most patients achieved successful cannulation following maturation without post-procedural complications.

CLINICAL SIGNIFICANCE

Staged full-length BAM is a safe and effective method for enhancing maturation in patients with underdeveloped small veins.

KEYWORDS

Arteriovenous fistula, balloon-assisted maturation, hemodialysis, maturation, stenosis

Due to the increasing number of patients requiring hemodialysis, efforts are underway to create arteriovenous fistulas (AVFs) in arteries or veins previously considered too small for AVF surgery. Although technological advancements have raised expectations for improved maturation rates, this issue remains a substantial challenge.[1] Several studies have addressed the failure of AVF maturation. Suggested interventions include preoperative vein preservation,[2] exercise,[3] and enhanced examination methods for veins and arteries, along with various surgical techniques introduced during the procedure.[4] Post-AVF forma-

tion, treatments such as balloon angioplasty for stenosis that impedes maturation, surgical ligation, or endovascular coil embolization of the collateral veins where flow steal occurs may be performed.[5-7] Additionally, techniques aimed at forcibly increasing vein size through surgical intervention have been attempted.[8]

Numerous studies have explored the application of balloon angioplasty following AVF creation to address the strictures causing primary AVF failure; however, the results, including technical and clinical success, remain unsatisfactory.[9-14] When balloon angioplasty is performed for anastomosis or juxta-anastomotic stenosis (JAS), although flow improvement is typically observed, the diameter of the entire vessel within the AVF circuit does not always increase. Consequently, the fistula cannot be immediately needled, requiring more time before the AVF is usable. Moreover, there are relatively few reports on balloon maturation in small veins ≤3 mm in diameter, and the clinical significance of such interventions, including long-term outcomes, remains unclear.[15,16]

In this study, we performed percutaneous angioplasty on the entire vein segment, addressing the stenosis responsible for primary AVF failure. To minimize the risk of barotrauma to the immature vein, we utilized two approaches: serial-staged upsizing balloon angioplasty and a long balloon catheter covering the entire vein segment to minimize balloon overlap. We analyzed the technical success of this staged full-length balloon-assisted maturation (BAM) and investigated clinical success rates, including AVF salvage, long-term AVF patency, and the occurrence of additional stenosis during long-term follow-up.

Main points

· Balloon-assisted maturation (BAM) for an arteriovenous fistula (AVF) involves adjusting the balloon catheter size to match the vein's actual size. Balloon dilation is performed along the entire length of the anatomical segment to minimize barotrauma in areas of overlapping balloon exposure.

· Among the patients, 34.6% underwent three or more procedures. The average AVF diameter increased from 4.03 mm to 5.95 mm, and the average AVF flow from 438.08 mL/min to 717.52 mL/min.

· No hematomas or ruptures were observed following full-length staged BAM; however, 65.2% of patients required additional percutaneous transluminal angioplasty to maintain patency during the follow-up period.

Methods

This retrospective study was conducted in accordance with the principles of the Declaration of Helsinki and received approval from the Institutional Review Board of Pusan National University Hospital, Republic of Korea (IRB no: 2308-024-130, date: 19.08.2023). Due to the retrospective nature of this study, the requirement for informed consent was waived.

Patient selection and data collection

Among 275 patients who underwent AVF surgery using autogenous veins at our hospital between February 2020 and June 2021, we collected data from patients who underwent staged angioplasty using a full-length balloon catheter. Patients who visited the outpatient clinic at 4–6 weeks post-AVF surgery underwent ultrasonography to evaluate AVF maturation. Staged full-length BAM was recommended for patients who exhibited an unsatisfactory increase in vein size, generally defined as no more than 4.5 mm in diameter. Additionally, even if the vein diameter exceeded 4.5 mm, challenges in cannulation could occur if the vessel was deeply situated. Out of these, 23 patients who consented to the procedure and have been under continuous observation with no loss to follow-up were included in the analysis (Figure 1).

Variables such as age, sex, follow-up duration, type of AVF, comorbidities, and smoking history were recorded. Detailed information on the size and depth of the arteries and veins before surgery, as well as the size and depth of the AVF at the time of the first procedure, was collected. Blood flow data, the total number of procedures performed, the degree of balloon used, the size and depth of the AVF post-final procedure, subsequent blood flow information, and success rates of cannulation and maturation were further investigated.

Staged balloon-assisted maturation using a full-length balloon catheter

Radiocephalic and brachiocephalic fistulas were assessed by puncturing the radial artery at the wrist, draining vein, or internal jugular vein under ultrasound guidance. During the procedure, the balloon diameter was set approximately 1 mm larger than the size of the native vein, and the balloon size was incrementally increased by 1 mm during subsequent procedures. The balloon length was determined by measuring the distance from the anastomosis to the tip of the anatomical section of the vein. The entire anatomical segment of the vein was dilated using a balloon measuring at least 120 mm in length. For patients on dialysis, a uniplanar angiography suite with a contrast agent was used; however, for pre-dialysis patients, a guidewire was inserted under ultrasound guidance to position the balloon, and fluoroscopy was used only for additional ballooning (Figure 2).
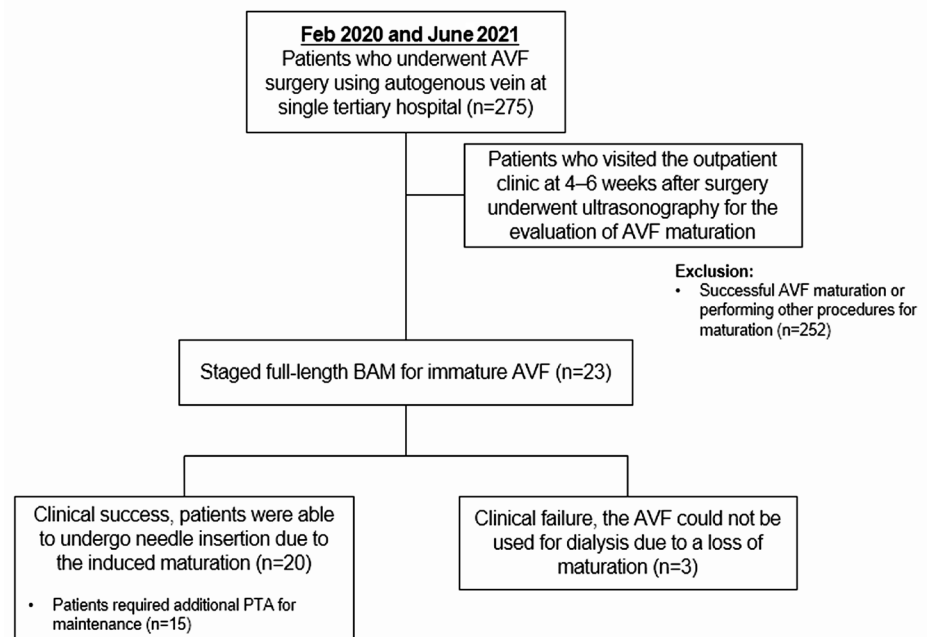

Figure 1. Flow chart depicting the patient selection process-arteriovenous fistula (AVF); balloon-assisted maturation (BAM); percutaneous transluminal angioplasty (PTA).

All patients returned for follow-up as outpatients 10 days after the initial procedure, at which point clinicians assessed the need for a second procedure. If necessary, the second treatment was conducted approximately 2 weeks after the first. These procedures were repeated until the vein size reached or exceeded 6 mm.

Outcomes and complications

Technical success was defined as the intentional expansion of the vein diameter without rupture, as confirmed by outpatient ultrasonography 10 days following the staged full-length BAM procedure. Clinical success was defined as the ability to conduct stable dialysis using an AVF within 3 months of performing the staged full-length BAM.

Postprocedural complications such as skin bruising, perivascular hematoma, rupture, and infection were monitored-additionally, progress after AVF maturation was observed, including cases where further procedures or surgeries were necessitated. The main lesions targeted in additional interventions were also documented.

Statistical analysis

Statistical analyses were conducted using basic descriptive statistics, with results presented as means and standard deviations. Logistic regression analysis was employed to estimate factors influencing failures and additional interventions post-maturation, whereas the chi-square test was used to compare characteristics between groups (intervention vs. non-intervention). Primary patency rates were calculated using Kaplan–Meier life-table analysis. Statistical significance was established at P values <0.05. All analyses were performed using MedCalc Statistical Software version 20.106 (MedCalc Software, Ostend, Belgium).

Results

The mean age of the patient cohort was 69.50 ± 11.12 years, and 39% of the patients were women. The average follow-up duration was 620.62 days. Among the comorbidities, 80.8% of the patients had diabetes, and the current smoking rate was 8.7%. Additionally, 88.5% of the patients had radiocephalic fistulas at the wrist, with the mean diameter of the radial artery being 2.14 ± 0.5 mm and that of the brachial artery being 4.5 ± 0.14 mm. The mean diameter of the veins used for surgery was 2.43 ± 0.5 mm. At the time of the first procedure, the mean diameter was 4.03

± 0.57 mm, and the average flow rate was 438.08 ± 220.95 mL/min. JAS was present in 61.5% of the cases. The median time from the

AVF operation to the first staged full-length BAM was 51 days. The patient characteristics are summarized in Table 1.
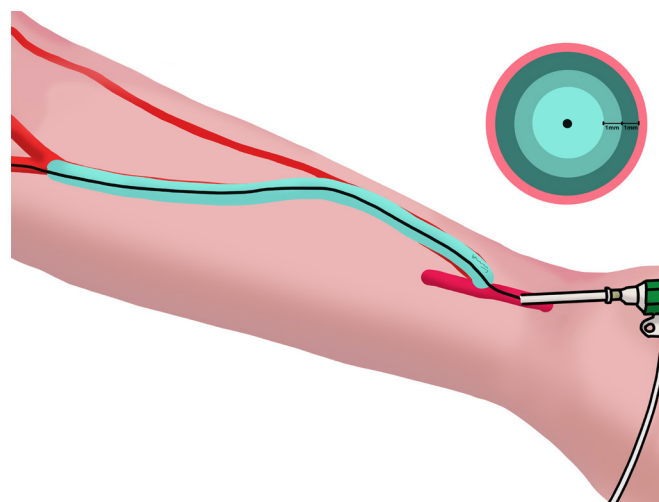
Figure 2. Illustration of staged full-length balloon-assisted maturation.

Table 1. Demographic data of the study participants

Variables		n = 23
Age (mean, SD) (years)	69.50	11.12
Sex (M:W)		17:9
Follow-up duration (mean, SD) (days)	620.62	260.40
Type of AVF (n, %)		
Radiocephalic	23	88.5%
Brachiocephalic	2	7.7%
Radiobasilic (with transposition)	1	3.8%
Preoperative condition (mean, SD)		
Artery diameter (mm)		
Radial	2.14	0.5
Brachial	4.5	0.14
Vein diameter (mm)	2.43	0.5
Duration (days) between surgery to the first staged balloon PTA* [median, (range)]	51	11–343
Preprocedural condition (mean, SD)		
Fistula diameter (mm)	4.03	0.57
Fistula depth (cm)	3.3	1.06
Fistula flow (mL/min)	438.08	220.95
Comorbidities (n, %)		
Diabetes	21	80.8%
Hypertension	17	23.1%
CAOD	5	19.2%
CVA	5	19.2%
Malignancy	2	7.7%
Glomerulonephritis	2	7.7%
Smoking status (n, %)		
Ex-smoker	12	46.2%
Current smoker	2	8.7%

Normally distributed data are presented as means and standard deviations; otherwise, medians and minimum-maximum values* are used. AVF, arteriovenous fistula; CAOD, coronary artery occlusive disease; CVA, cerebrovascular accident; W, women; M, men; PTA, percutaneous transluminal angioplasty; SD, standard deviation.

Staged full-length balloon-assisted maturation

Ten patients (28.5%) underwent a single procedure, whereas nine (34.6%) underwent three or more procedures (Table 2). The Mustang balloon (Boston Scientific, Marlborough, MA, USA) was the most commonly used balloon catheter. The balloons typically had a diameter of 5 mm and a length of 150 mm. After the final procedure, the AVF diameter was measured separately at the arterial and venous needle cannulation areas (Table 2). These measurements were taken during hemodialysis sessions using the fistula. Detailed information on the balloons used, the condition of the AVF prior to the procedures, and the outcomes are provided in the Supplementary Table.

Outcomes and complications

There was a substantial increase in both the pre- and postoperative diameters of the AVF at the arterial and venous cannulation sites. Additionally, there was a considerable increase in blood flow within the AVF (Table 3). The fistula matured successfully in 87% of the patients. However, clinical failure occurred in 3 of the 23 patients, as their AVFs could not be used for dialysis due to unsuccessful maturation, as noted with an asterisk (*) in the Supplementary Table. Logistic regression analysis was conducted to identify potential factors contributing to these failures, but no statistically significant factors were identified.

Despite successful maturation and cannulation, 15 of the 23 patients (65.2%) required additional percutaneous transluminal angioplasty (PTA). The frequency of additional PTA and the number of these procedures are detailed in the Supplementary Table. The decision to perform additional PTA was influenced by the presence of JAS prior to the first full-length balloon angioplasty. The odds of requiring additional PTA for patients with pre-existing JAS were significantly higher, with an odds ratio of 9.33 (P = 0.03; 95% confidence interval: 1.22–97.62). When comparing AVF data between patients who underwent additional PTA and those who did not, a notable difference in the incidence rate of JAS was observed (Table 4). Additional PTA targeted the JAS in 7 of the 15 patients and was performed on various venous zones outside the JAS in the remaining 8 patients. The 1-year primary patency rate of these interventions was 49.2% (Figure 3).

In terms of postoperative complications, bruising occurred in 3 patients; however, there were no cases of hematoma, vascular rupture, procedure-related infections or access-site complications.

Discussion

BAM is a method for the forced maturation of immature AVFs that initially appears effective; however, there is an ongoing debate about its long-term patency.[7,17-22] A recent meta-analysis by Tordoir et al.[5] reported BAM success rates ranging from 43% to 97%. The most frequent complication was a hematoma, occurring in about 40% of cases, typically caused by using overly large balloons in the forearm. The study also noted a low long-term primary patency rate (28%–72%), indicating that multiple interventions might be necessary to maintain patency.[5]

In previous research, de Oliveira Harduin et al.[23] conducted percutaneous angioplasty on the entire vein segment to expand the vessel wall and enhance blood flow by inducing controlled rupture or controlled intramural hematoma from the intima, media, and adventitia layers. This technique resulted in the formation of a large-diameter AVF circuit with patency comparable to that of a mature AVF. Although this approach achieved a high success rate of approximately 91%, substantial complications such as massive pseudoaneurysm from large-sized ballooning, uncontrolled steal, and juxta-anastomosis rupture requiring AVF ligation still occurred in about 5% of cases.[23]

In situations where the balloon diameter exceeds the AVF size by more than 2 mm, the vessel circumference increases by approximately 6 mm, substantially raising the risk of rupture. Therefore, the present study utilized staged full-length BAM to reduce this risk and increase the size of the entire venous segment where maturation was inadequate. The clinical outcomes of this staged approach did not substantially differ from earlier reports. Despite the intended uniform

Table 2. Characteristics of staged balloon percutaneous transluminal angioplasty

Number of procedures performed (median, [range])	2	[1–4]
1	10	28.5%
2	7	26.9%
3	6	23.1%
4	3	11.5%
Median diameter of the first balloon (median, [range]) (mm)	5	[3–7]
Median length of the first balloon (median, [range]) (mm)	150	[120–220]
Type of the first balloon (n, %)		
Mustang[a]	18	69.2%
Passeo[b]	3	11.5%
Achilles[c]	4	15.4%
Sterling[d]	1	3.8%
Postprocedural fistula diameter (mean, SD) (mm)		
Arterial needle cannulation area	5.94	0.86
Venous needle cannulation area	5.7	0.81
Postprocedural fistula depth (mean, SD) (mm)		
Arterial needle cannulation area	2.9	0.71
Venous needle cannulation area	2.6	1.03
Postprocedural fistula flow (mean, SD) (mL/min)	716.25	663.5
Success rate of maturation and needling (n, %)	24	92.3%

[a]Mustang balloon: Boston Scientific, Marlborough, MA, USA; [b]Paseo balloon: Biotronik AG, Bülach, Switzerland; [c]Achilles balloon: BrosMed Medical, Guangdong, China; [d]Sterling balloon: Boston Scientific, Natick, MA, USA. SD, standard deviation.

Table 3. Independent t-test results comparing pre- and postprocedural fistula diameter and flow

Parameter	Preprocedural	Postprocedural	P value
Arterial needle cannulation area (mm)	4.15	5.94	<0.01
Venous needle cannulation area (mm)	4.09	5.70	<0.01
Flow (mL/min)	438.08	716.25	<0.01

increase in size not occurring in all patients, there were no procedure-related complications, such as hematoma or rupture.

The immediate technical success rate in this study was 100%, and the clinical success rate of the dialysis access technique described was 87%. For the 3 patients in whom the procedure failed, vein size was maintained during follow-up at the outpatient clinic 2 weeks post-procedure. However, severe intimal hyperplasia developed within 3 months, preventing lumen maintenance and rendering the AVFs unusable. Consequently, AVFs that underwent unsuccessful BAM were ligated, and new AVFs were created.

In patient 26 (Supplementary Table), the fistula was a left wrist radiocephalic type. Ultrasound examination conducted 15 weeks post-fistula formation showed an ambiguous vein size of 5.3 mm. Despite attempts at puncture, repeated hematomas occurred due to the deep placement and small size of the vein, which is unsuitable for dialysis. The staged full-length BAM was selected to potentially facilitate easier puncture by increasing the vein diameter. The procedure was performed at 2-week intervals using 6 mm and 7 mm balloons. Immediately after the procedure, the diameter and flow were confirmed to be sufficient for maturation success. However, for reasons not well understood, severe intimal hyperplasia developed throughout the forearm cephalic vein, leading to fistula failure (Figure 4). Prior to balloon angioplasty, the vein was cleaner and well-maintained. At the time of radiocephalic fistula formation, the cephalic vein in the upper arm increased in size, and the balloon did not traumatize the area. Subsequently, a brachiocephalic fistula was created and maintained successfully for 2 years without further intervention. In such cases, it may have been preferable to perform superficialization without BAM or PTA. Even if the vein diameter was initially large, staged full-length BAM did not consistently induce maturation, and the veins could fail during the maturation process due to intimal damage along the entire length of the vein caused by the balloon.

In patients 14 and 24 (supplement), there was little or no increase in vein size following balloon angioplasty; in some instances, the actual vein diameter was smaller than before the procedure. Ultrasound imaging revealed extensive intimal hyperplasia throughout the forearm cephalic vein, and an AVF occlusion developed within a month, necessitating a switch to an arteriovenous graft. Logistic regression analysis was conducted to identify

Table 4. Comparison of groups that required and did not require additional treatment after maturation

Variable	Additional intervention (+)	Additional intervention (-)	P value
Preoperative factors			
Artery diameter (mm)	2.24 ± 0.82	2.43 ± 0.79	0.56
Vein diameter (mm)	2.39 ± 0.46	2.49 ± 0.59	0.64
Preprocedural factors			
Fistula diameter (mm)	4.19 ± 0.80	4.09 ± 0.49	0.71
Fistula flow (mL/min)	407.01 ± 227.59	480.45 ± 214.73	0.41
JAS [n (%)]	12 (80%)	4 (36.3%)	0.03
Postprocedural factors			
Fistula diameter (mm)	6.20 ± 0.75	5.57 ± 0.89	0.06
Fistula flow (mL/min)	699.43 ± 315.66	739.20 ± 299.25	0.75

JAS, juxta-anastomosis stenosis.
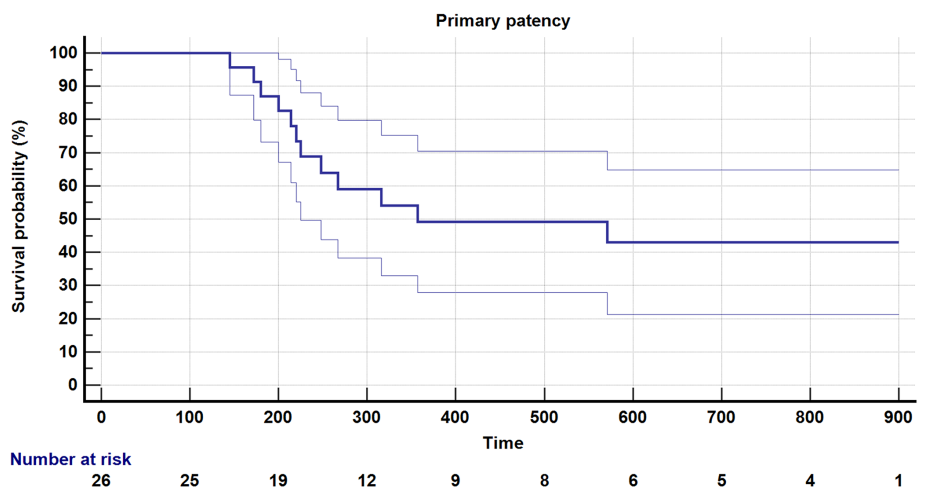
Figure 3. Primary patency of arteriovenous fistulas following staged full-length balloon-assisted maturation. The 1-year primary patency rate was 49.2%.
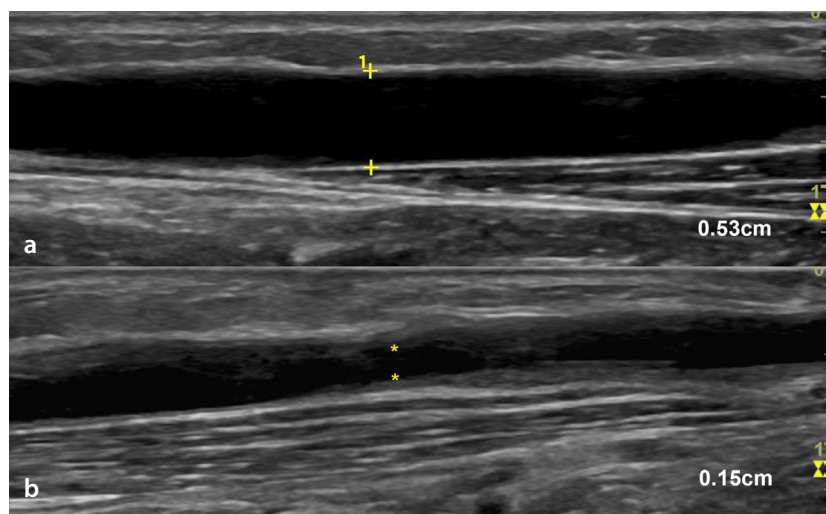
Figure 4. An example case of a patient who failed to achieve staged full-length balloon-assisted maturation (BAM). **(a)** Arteriovenous fistula image before cannulation showing a vein diameter of 0.56 cm and a clean, undamaged wall. **(b)** Severe intimal hyperplasia observed 3 months after staged full-length BAM.

factors influencing the failure of the procedure due to severe intimal hyperplasia, but no substantial factors were identified; even after a thorough review of the raw data and images, no singular cause was determined.

Overall, 73.9% of the patients included in this study had small veins (≤2.5 mm) before AVF formation. The smallest recorded vein diameter was 1.3 mm, with 3 patients presenting veins ≤1.6 mm in diameter. Despite these small diameters, a radiocephalic fistula was chosen for these patients as a radial-based native fistula, which was expected to increase blood flow gradually while minimizing the impact on existing heart disease. Notably, 2 of the 3 patients with preoperative vein diameters of ≤1.6 mm successfully achieved maturation using staged full-length BAM.

In this study, the presence of JAS at the time of the first procedure was a substantial factor when additional PTA was required. JAS was the primary target of PTA in 46.7% of cases, with considerable stenosis occurring at various sites, including drainage veins and puncture sites. This suggests that the findings from previous studies remain relevant. The 1-year primary patency rate in this study was 49.2%. To minimize venous trauma, balloons were gradually expanded, starting with smaller sizes; however, the gradual stenosis could not be fully mitigated. These results underscore that forcibly inducing maturation of native AVFs by PTA inevitably damages the venous intima, leading to substantial stenosis over time.

This study had several limitations that should be noted. First, its single-center, retrospective design may have introduced patient selection bias. Second, the small sample size could lead to statistical inaccuracies. Third, it was not possible to ascertain the cause of clinical failure using only the data collected in this study. Further research is needed to confirm these findings.

In conclusion, in attempting BAM for AVF in this study, balloon size was gradually increased, and ballooning was performed along the full-length anatomical segment to minimize barotrauma where the balloon overlapped. As a result, 87% of patients succeeded in reaching maturation sufficient for needling, although 62.5% required additional procedures during follow-up to maintain patency. Despite the burden of repeated procedures on patients and clinicians, these findings suggest that this approach is a safe option for patients with small, immature veins.

References

1. Rezapour M, Sepehri MM, Khavanin Zadeh M, Alborzi M. A new method to determine anastomosis angle configuration for arteriovenous fistula maturation. *Med J Islam Repub Iran*. 2018;32:62. [CrossRef]

2. Vachharajani TJ, Hassanein M, Liaqat A, Haddad N. Vessel preservation in chronic kidney disease. *Adv Chronic Kidney Dis*. 2020;27(3):177-182. [CrossRef]

3. Meng L, Zhang T, Ho P. Effect of exercises on the maturation of newly created arteriovenous fistulas over distal and proximal upper limb: a systematic review and meta-analysis. *J Vasc Access*. 2024;25(1):40-50. [CrossRef]

4. Shembekar SN, Zodpe DB, Padole PM. Prediction of the anastomosis angle of arteriovenous fistula in hemodialysis to standardize the surgical technique. *Biomed Mater Eng*. 2022;33(5):423-436. [CrossRef]

5. Tordoir JHM, Zonnebeld N, van Loon MM, Gallieni M, Hollenbeck M. Surgical and endovascular intervention for dialysis access maturation failure during and after arteriovenous fistula surgery: review of the evidence. *Eur J Vasc Endovasc Surg*. 2018;55(2):240-248. [CrossRef]

6. Abreo K, Buffington M, Sachdeva B. Angioplasty to promote arteriovenous fistula maturation and maintenance. *J Vasc Access*. 2018;19(4):337-340. [CrossRef]

7. Kanchanasuttirak P, Pitaksantayothin W, Saengprakai W, Kanchanabat B. Systematic review and meta-analysis: efficacy and safety of balloon angioplasty in salvaging non-matured arteriovenous fistula. *J Vasc Access*. 2023;24(6):1244-1252. [CrossRef]

8. Nauwelaers S, Lansink W, Schroë H, Lauwers G. Surgical rejoining of small arm veins to enhance dialysis fistula maturation. *J Vasc Access*. 2020;21(1):105-109. [CrossRef]

9. Li YS, Li YC, Yu SY, et al. The clinical outcome of balloon-assisted maturation procedure between autogenous radiocephalic fistula and brachiocephalic fistula in a single-center experience. *J Vasc Surg*. 2022;76(4):1060-1065. [CrossRef]

10. Thomas SD, Sideris A, Narroway H, et al. Arteriovenous fistula formation with adjuvant endovascular maturation. *J Vasc Surg*. 2022;75(2):641-650. [CrossRef]

11. Lee SJ, Jeon GS, Lee B, Lee G, Lee JJ. Endovascular management in immature arteriovenous fistula for hemodialysis. *Medicine (Baltimore)*. 2018;97(36):e12211. [CrossRef]

12. Yadav N, Gamanagatti S, Sharma R, et al. Outcomes of endovascular therapy for salvage of hemodialysis arteriovenous fistulae. *J Clin Int Radiol ISVIR*. 2021;5(3):142-149. [CrossRef]

13. Park SC, Ko SY, Kim JI, Moon IS, Kim SD. Balloon-assisted maturation for arteriovenous fistula maturation failure: an early period experience. *Ann Surg Treat Res*. 2016;90(5):272-278. [CrossRef]

14. Park HS, Lee YH, Kim HW, et al. Usefulness of assisted procedures for arteriovenous fistula maturation without compromising access patency. *Hemodial Int*. 2017;21(3):335-342. [CrossRef]

15. Kim HK, Han A, Ahn S, et al. Better efficacy of balloon assisted maturation in radial-cephalic arteriovenous fistula for hemodialysis. *Vasc Specialist Int*. 2021;37(1):29-36. [CrossRef]

16. Kao TC, Hsieh HC, Yu SY, Su TW, Ko PJ. Long-term efficacy and risk factors of balloon-assisted maturation for radial-cephalic arteriovenous fistula with small-caliber veins. *Hemodial Int*. 2023;27(3):241-248. [CrossRef]

17. Huang HC, Hsu CY, Kang MY. Does the balloon-assisted maturation procedure offer comparable results for AVF created with a smaller vein. *J Vasc Access*. 2023:11297298221150665. [CrossRef]

18. Roy-Chaudhury P, Lee T, Woodle B, Wadehra D, Campos-Naciff B, Munda R. Balloon-assisted maturation (BAM) of the arteriovenous fistula: the good, the bad, and the ugly. *Semin Nephrol*. 2012;32(6):558-563. [CrossRef]

19. DerDerian T, Hingorani A, Boniviscage P, Carollo A, Ascher E. Acute complications after balloon-assisted maturation. *Ann Vasc Surg*. 2014;28(5):1275-1279. [CrossRef]

20. Elkassaby M, Elsaadany N, Mowaphy K, Soliman M. Balloon-assisted maturation of autogenous arteriovenous fistulae: a randomized controlled prospective study. *Vascular*. 2021;29(5):776-783. [CrossRef]

21. Park SC, Ko SY, Kim JI, Moon IS, Kim SD. Balloon-assisted maturation for arteriovenous fistula maturation failure: an early period experience. *Int J Adv Res Biol Sci*. 2021;8(2):40-49. [CrossRef]

22. Gabr AK, Allam AK, Abouelregal TE. Primary balloon angioplasty combined with balloon-assisted maturation of autogenous arteriovenous fistula in patients with small-caliber vasculature. *Ain Shams J Surg*. 2018;11(1):25-34. [CrossRef]

23. de Oliveira Harduin L, Guerra JB, Virgini-Magalhães CE, et al. Oversized balloon angioplasty for endovascular maturation of arteriovenous fistulae to accelerate cannulation and to decrease the duration of catheter use. *J Vasc Access*. 2023;24(2):238-245. [CrossRef]

Supplementary Table. Overview of the procedural details

Patient	Pre-AVF condition		Preprocedural condition			Procedure details				Postprocedural condition				Result	
	Artery size	Vein size	Size	Flow	JAS	First balloon	Second balloon	Third balloon	Fourth balloon	Size (A)	Size (V)	Flow	Needling	Additional PTA	F/U duration
1	1.6	2.3	3.5	480.0	Y	5/120 Passeo	6/150 Mustang	7/150 Mustang		6.3	6.1	716.4	Y	3	785
2	1.8	1.6	4	440.0	Y	6/120 Mustang				5.2	4.7	624.9	Y	0	398
3	2	3	4.5	403.1	N	6/120 Passeo	7/150 Mustang			6.5	6.6	719.0	Y	1	575
4	1.6	2.3	4.1	227.0	Y	5/120 Mustang	6/150 Mustang			5.2	5.4	551.0	Y	3	331
5	2.2	3	4.2	381.2	Y	5/170 Passeo		7/150 Mustang		7.6	7.2	419.5	Y	1	571
6	2	3	3.5	140.5	Y	4/150 Mustang	5/150 Mustang	6/150 Mustang	7/150 Mustang	5.5	5.6	1140.0	Y	3	908
7	3.2	2.7	5.2	1000.0	N	7/20 Mustang				6.4	6.3	1618.0	Y	1	936
8	2.3	3.5	4.5	860.0	N	5/150 Mustang				6.2	6.3	800.0	Y	0	698
9	2.5	2.5	4.4	623.0	N	5/200 Mustang	6/200 Mustang			5.5	5.9	1074.0	Y	0	870
10	2.3	3	4.3	458.4	N	6/200 Mustang	7/200 Mustang			6.3	6.8	576.3	Y	0	876
11	1.9	2	3.6	436.2	Y	5/120 Mustang				6.1	5.1	451.5	Y	2	833
12	2	1.3	4.6	631.5	N	5/150 Mustang	6/200 Mustang	7/200 Mustang		7.8	6.5	868.2	Y	1	858
13	**4.6	2.4	3.6	321.4	N	4/150 Mustang	5/120 Mustang	6/80 Mustang	6/80 Mustang	5.6	5.2	702.1	Y	4	752
*14	2	1.4	3	388.0	Y	3/220 Sterling	4/220 Sterling	5/220 Sterling		4.2	4.2	341.0	N	0	110
15	1.5	2.4	4.1	332.0	N	5/150 Achilles				6.4	5.4	790.6	Y	0	675
16	2.8	2.5	3.8	168.0	Y	5/200 Mustang	6/150 Achilles			5.6	5.4	475.8	Y	1	734
17	2.8	2.5	3.4	794.9	Y	5/120 Mustang	6/200 Mustang	7/200 Mustang		6.5	6.1	912.0	Y	0	570
18	2.2	2.4	3.9	573.0	Y	5/200 Mustang	6/200 Mustang			5.9	6.5	774.0	Y	3	352
19	2	2	3.3	114.2	Y	5/200 Mustang				5.9	4.5	580.0	Y	1	797
20	2.2	2.5	4	220.0	Y	5/22 Mustang				5.8	5.8	624.4	Y	0	596
21	2.3	2.6	4.4	376.5	Y	5/150 Mustang	5/150 Mustang	6/120 Mustang	6/170 Passeo	5.5	5.4	539.5	Y	2	1013
22	3	2.6	4.5	509.7	N	5/200 Mustang	6/200 Mustang			5.4	5.4	980.0	Y	0	477
23	**4.4	2.9	4.2	488.9	Y	5/150 Achilles				6.0	6.2	1203.0	Y	0	767
*24	1.9	2.5	4.6	170	N	5/150 Mustang				3.8	3.9	220	N	0	82
25	1	2	4.5	297	Y	5/150 Achilles	5/200 Achilles			6.7	5.3	429	Y	0	325
*26	2.2	2.4	5.3	555.6	Y	6/150 Achilles	7/200 Mustang			6.5	6.3	525.4	Y	0	161

*Failure within 3 months; ** Brachial artery. The unit of size is mm, and the unit of flow is mL/min. AVF, arteriovenous fistula; JAS, juxta-anastomosis stenosis; N, no; PTA, percutaneous transluminal angioplasty; size (A), diameter of arterial needle cannulation area; size (V), diameter of venous needle cannulation area; Y, yes.

Short-term outcomes of the iCover balloon-expandable covered stent for iliac artery lesions

 Murat Canyiğit[1]
 Muhammed Said Beşler[2]

[1]Yıldırım Beyazıt University Faculty of Medicine, Department of Radiology, Ankara, Türkiye

[2]Kahramanmaraş Necip Fazıl City Hospital, Clinic of Radiology, Kahramanmaraş, Türkiye

PURPOSE

To describe the short-term follow-up results of the recently introduced iCover balloon-expandable covered stents for iliac artery lesions.

METHODS

All consecutive patients treated with iCover balloon-expandable covered stents between March 2022 and August 2023 were retrospectively reviewed. The primary endpoint was target lesion revascularization (TLR) at 6 months. Secondary endpoints included major adverse events, freedom from TLR throughout the follow-up period, primary and secondary patency, and clinical and technical success.

RESULTS

In the study population of 40 adult patients (87.5% men, mean age: 63.5 ± 11 years), the mean follow-up period was 6.2 ± 2.8 months. A total of 98 stents of various sizes were implanted. The technical success rate was 100%. Freedom from TLR was 95.8% [95%, confidence interval (CI): 95%–96.6%], the primary patency rate was 91.7% (95%, CI: 89.8%–93.6%), and the secondary patency rate was 95.8% (95%, CI: 95%–96.6%) at 6 months. The all-cause mortality rate was 5%.

CONCLUSION

These real-world data demonstrate a high technical and clinical success rate, a high 6-month primary patency rate, and a low requirement for TLR. These are promising indicators for the safety and efficacy of iCover stents.

CLINICAL SIGNIFICANCE

Balloon-expandable covered stents are frequently used in iliac artery atherosclerotic disease. This study shows that the short-term follow-up results of the new iCover stent are satisfactory, indicating its safety and efficacy.

KEYWORDS

Angiography, balloon-expandable covered stent, iliac artery disease, peripheral, stent

E ndovascular treatment, particularly stent implantation procedures, is widely used, with high technical success and patency rates in peripheral artery stenoses and occlusions, such as those found in the aorto-iliac, subclavian, and mesenteric arteries.[1,2] Covered stents are theoretically known to reduce restenosis rates by limiting neointimal hyperplasia and thrombosis and providing early luminal endothelialization.[3] The use of covered stents is common in treating conditions such as arteriovenous fistula, iliac aneurysms, and peripheral arterial disease.[4,5]

Balloon-expandable and self-expandable stent grafts show similar performance in mid-term results.[6,7] In a study by Krankenberg et al.[8] examining uncovered stents for the treatment of iliac artery occlusive disease, self-expandable stents showed lower rates of restenosis and target lesion revascularization (TLR) compared with balloon-expandable stents at a 1-year

Corresponding author: Muhammed Said Beşler

E-mail: msbesler@gmail.com

follow-up. Balloon-expandable stents have advantages over self-expandable stents, including higher radial strength and more predictable deployment.[9] In the DISCOVER trial, no difference was found in the rates of freedom from restenosis and TLR between covered and bare-metal stents at a 2-year follow-up for common iliac artery atherosclerotic disease.[10] Some studies have shown that, compared with bare-metal stents, covered stents can increase freedom from TLR in aorto-iliac arterial disease and be advantageous and preferable in more complex and severely calcified lesions.[11,12] The 5-year results of the COBEST study demonstrate that covered stents provide higher patency in aorto-iliac occlusive disease compared with bare-metal stents in long-term follow-up.[13]

For these reasons, the use of covered stents in iliac artery diseases is becoming more widespread. Currently, there are no original studies or case reports in the literature regarding the recently introduced iCover stents for iliac artery lesions. This study aims to evaluate the safety and short-term effectiveness of the iCover stents using real-world data.

Methods

Study design

This single-center, retrospective study was approved by the Ankara Bilkent City Hospital Review Board (decision number: E2-23-4066, date of approval: 10.05.2023). It received a waiver of informed consent and was conducted in accordance with the Declaration of Helsinki. All consecutive patients treated with iCover stents during the study period, between March 2022 and August 2023, were assessed. Patients with stents implanted in the subclavian artery (n = 7), renal artery (n = 3), celiac artery (n = 2), and brachiocephalic truncus (n = 1) were excluded. The study population consisted of 40 adult patients treated for common and external

iliac arteries (Figure 1). Among these patients (87.5% men, mean age: 63.5 ± 11 years), the mean follow-up period was 6.2 ± 2.8 months (Table 1). Patients included in the study had symptomatic peripheral arterial disease in the iliac arteries, with severe stenosis or occlusions ranging from claudication limiting quality of life to tissue loss (Rutherford category 3 or higher). All procedures were performed by an interventional radiologist with 20 years of experience in peripheral artery interventions.

Demographic characteristics, comorbidities, stenosis or occlusion locations, procedural adverse events, pre-procedural symptoms, follow-up examinations, and post-procedural antiplatelet medication compliance were recorded.

The iCover balloon-expandable expanded polytetrafluoroethylene (e-PTFE)-covered stent (iVascular, Barcelona, Spain) was compatible with a 0.035-inch guidewire, catheter lengths of 80 or 140 cm, and 6F or 7F introducer sheaths. It was available in various diameters (5–10 mm) and lengths (17–57 mm). Stents with a diameter of 5–8 mm allowed post-dilation up to 10 mm, whereas those with a diameter of 9–10 mm permitted post-dilation up to 12 mm.

The femoral artery was preferred for vascular access in 35 patients, whereas the brachial artery was chosen in five patients. A 7F introducer sheath was inserted. At the beginning of the procedure, 70 U/kg heparin was administered as an intravascular bolus. After confirming significant stenosis or occlusion with digital subtraction angiography, the lesion was crossed with a 0.035-inch guidewire. The native vessel diameter and lesion length were measured on a case-by-case basis, and a stent was deployed. Pre-dilation or post-dilation was performed using a non-compliant balloon if necessary. An additional 2,500 U heparin dose was administered every hour if the procedure lasted a long time. The procedure was concluded if <30% residual stenosis was seen on post-procedural angiography.
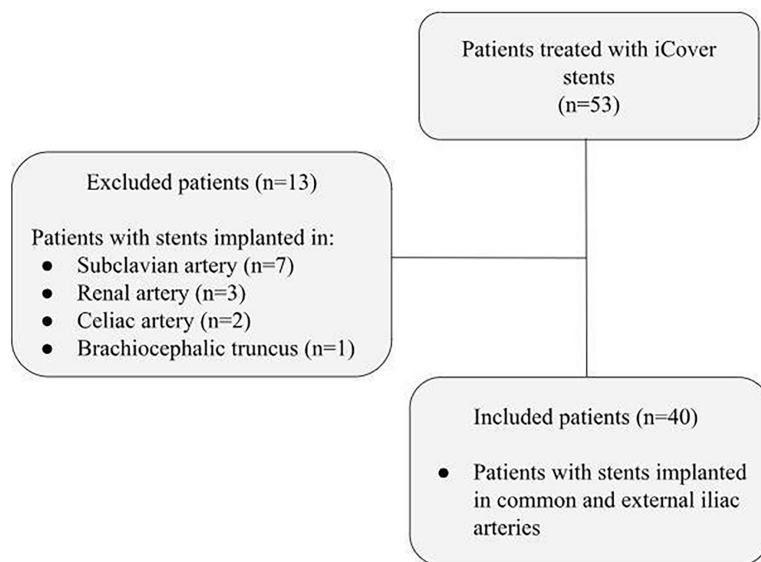

Figure 1. Flowchart of patient selection.

Main points

- Balloon-expandable covered stents can be used for iliac artery lesions.

- The novel iCover stents have demonstrated satisfactory freedom from target lesion revascularization and high primary and secondary patency rates in short-term follow-up.

- According to the study results, the newly introduced stents are safe and effective for the treatment of iliac artery atherosclerotic disease.

Table 1. Baseline characteristics of the study population

Characteristic	Total (n = 40)
Gender, men	35 (87.5)
Age, years	63.5 ± 11
Hypertension	28 (70)
Diabetes mellitus	22 (55)
Coronary artery disease	20 (50)
Smoking (pack/years)	22.5 [0–40]
Peripheral arterial bypass graft history	3 (7.5)
Previous endovascular treatment in the target lesion area	5 (12.5)
Limb amputation history	1 (2.5)
Data are presented as number (percentage), mean ± standard deviation, and median [interquartile range 25–75].	

Each patient was prescribed clopidogrel (75 mg) daily for 6 months and lifelong acetylsalicylic acid (100 mg).

Outcome measures

Primary patency was defined as <50% restenosis on Doppler ultrasound or computed tomography angiography, along with no revascularization, bypass surgery, or target limb amputation. A peak systolic velocity ratio of <2 corresponded to a diameter stenosis of <50%. Secondary patency was defined as the patency of the target lesion after treatment of a reocclusion through either a surgical bypass or endovascular intervention. Procedural success was defined as <%30 residual stenosis on final angiography. Clinical success was defined as at least a one-point improvement in the Rutherford category for iliac artery lesions.

The primary endpoint was TLR at 6 months. Secondary endpoints included major adverse events (death, myocardial infarction at 30 days, stent thrombosis, acute limb ischemia, target limb amputation, or procedure-related major bleeding), freedom from TLR, primary and secondary patency, and clinical and technical success rates. Reintervention was performed for >50% stent restenosis accompanied by clinical symptoms.

Clinical examinations and symptom assessments were conducted at 1, 3, 6, and 12 months of follow-up, noting any adverse events. Stent patency was assessed using computed tomography angiography or Doppler ultrasound (if the glomerular filtration rate was <60 mL/min) routinely at 3- and 6-month follow-ups, or during clinical follow-up examinations if improvement was not achieved according to clinical success criteria.

Statistical analysis

Statistical analysis was conducted using SPSS 26.0 (IBM, Armonk, NY, USA). In descriptive statistics, the normality of data distribution was determined by the Shapiro–Wilk test. Continuous variables were expressed as mean ± standard deviation, median (range: minimum–maximum), or median (interquartile range: 25–75), whereas categorical variables were expressed as numbers and percentages. Patency rates and freedom from TLR during follow-up were calculated using Kaplan–Meier estimates.

Results

A total of 98 stents were implanted in 40 patients for iliac artery diseases. The intervention was performed on the common iliac artery in 55% of the patients, on the external iliac artery in 30%, and on both the common and external iliac arteries in 15%. Stents were implanted in the stenosis area in 21 patients (52.5%) and in the occlusion area in 19 patients (47.5%). The stents had a median diameter of 8 mm (range: 6–10 mm) and a median length of 37 mm (range: 27–57 mm) (Table 2). One patient with extensive aorto-iliac disease was treated using the covered endovascular reconstruction of the aortic bifurcation technique. The technical success rate was 100%, and the overall clinical success rate was 90%.

During follow-up, stent occlusion was detected in the common iliac arteries of two patients. One of these patients under-

went aortofemoral bypass surgery. The other patient had a reintervention with the deployment of an iCover stent, and the newly deployed stent was patent at the 6-month follow-up. It was found that these patients, who experienced stent occlusion, had discontinued clopidogrel after the 1st month post-procedure, continuing only with acetylsalicylic acid. Freedom from TLR was 95.8% [95%, confidence interval (CI): 95%–96.6%], the primary patency rate was 91.7% (95%, CI: 89.8%–93.6%), and the secondary patency rate was 95.8% (95%, CI: 95%–96.6%) at 6 months (Figures 2-4).

In one patient, during iliac artery stent deployment, plaques migrated to the terminal aorta, necessitating the placement of kissing stents. In another patient who underwent stent placement in the external iliac artery, plaque migrated to the internal iliac artery, which was managed by deploying an uncovered stent in the internal iliac artery. Similarly,

Table 2. The sizes and numbers of deployed stents

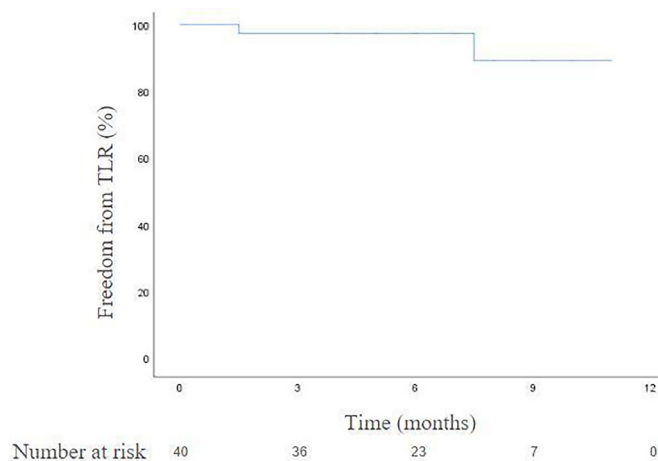| Diameter (mm)–length (mm)	Number of stents (n = 98)
6–27	1
6–37	10
6–57	4
7–27	10
7–37	4
7–57	15
8–27	8
8–37	8
8–57	10
9–27	7
9–37	8
9–57	8
10–27	1
10–37	4

Figure 2. Kaplan–Meier estimate of freedom from target lesion revascularization throughout the follow-up period. TLR, target lesion revascularization.
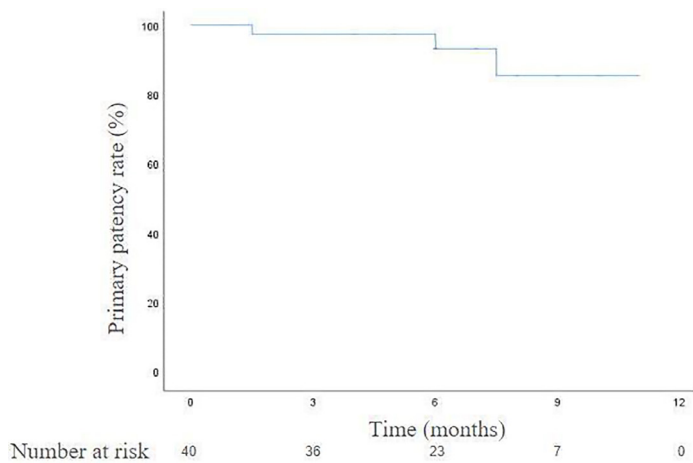
Figure 3. Kaplan–Meier estimate of primary patency throughout the follow-up period.
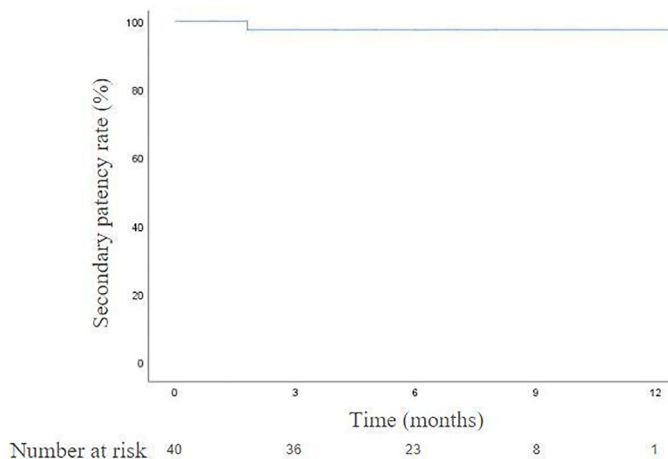

Figure 4. Kaplan–Meier estimate of secondary patency throughout the follow-up period.

in a patient where stent placement was performed in the external iliac artery through brachial artery access, plaque migrated from the terminal aorta to the contralateral external iliac artery, requiring the placement of a stent in that region as well. Vascular access adverse events included a femoral artery pseudoaneurysm in one patient, which was corrected with manual compression. No structural concerns, such as stent fracture or kinking, were encountered. No major amputations of the target limb occurred during follow-up.

The all-cause mortality rate was 5% (n = 2). No in-hospital mortality was observed within the first 30 days. After 30 days, mortality unrelated to endovascular procedures occurred. One patient experienced gastrointestinal bleeding due to anticoagulant and antiplatelet therapy for graft thrombosis after bypass surgery in the target vessel, and another patient with colon cancer and acute pulmonary edema died.

Discussion

In this study observing early outcomes of a newly introduced balloon-expandable stent in 40 patients, real-world data was evaluated. The use of stents in iliac arteries and short-term follow-up results were examined. Despite a median follow-up of 6 months, the absence of technical failures, high clinical improvement rates, and elevated primary and secondary patency rates, along with a high rate of freedom from TLR, suggest the safety and effectiveness of the stent in treating iliac artery disease.

In e-PTFE-covered stents, the surrounding membrane reduces cytokine and growth factor secretion, thereby inhibiting smooth muscle cell migration and neointimal tissue growth. This thin membrane decreases stent radial pressure, cutting off the connection between the vessel wall and blood flow, which helps reduce re-embolization.[14] Balloon-expandable and self-expandable covered stents, as well as bare-metal stents, offer various solutions in the primary treatment of peripheral arterial occlusive disease.[8,15,16] A study highlighting the use of balloon-expandable covered stents, especially in the iliac arteries, noted that these stents were clinically useful for addressing recurrent in-stent restenosis.[17] In this study, a balloon-expandable covered stent was used for the treatment of iliac artery reocclusion, and the newly deployed stent was patent at the 6-month follow-up.

In the guideline by the Society for Cardiovascular Angiography and Interventions regarding aorto-iliac arterial interventions, drug-eluting stents are not recommended for aorto-iliac arterial disease. However, self-expandable covered stents are suggested with a weak to moderate recommendation, whereas bare-metal stents are recommended at various levels. Balloon-expandable covered stents are endorsed with a moderate to strong recommendation. Specifically, balloon-expandable covered stents are strongly recommended for aorto-iliac bifurcation and common iliac artery locations, particularly in cases of moderate to severely calcified lesions.[18] In the ICE trial, the use of uncovered stents for treating iliac artery occlusive disease was compared. The results showed that self-expandable stents had better primary patency at a 1-year follow-up than balloon-expandable stents.[8] In the DISCOVER trial, at a 2-year follow-up for the treatment of common iliac artery atherosclerotic disease, the results for balloon-expandable covered stents and balloon-expandable bare-metal stents were similar.[10] In a study involving a 2-year follow-up on iliac axis occlusions, both self-expandable and balloon-expandable covered stents, used alone or in combination, achieved excellent patency rates.[19] For aorto-iliac occlusive disease, the long-term results of balloon-expandable covered stents provide acceptable patency rates.[13,20] The BOLSTER clinical trial demonstrated that balloon-expandable covered stents for iliac artery occlusive disease had 89.1% primary patency, 96% freedom from TLR, and 90.5% clinical improvement at the 9-month follow-up.[21] In the VISIBILITY study, a 9-month follow-up on atherosclerotic diseases of the common and external iliac arteries showed that balloon-expandable stents achieved a primary patency and freedom from target vessel revascularization rate of 95.8%.[22] Our study population's results, with 91.7% primary patency, 95.8% freedom from TLR, and 90% clinical success rates, are comparable with these short-term studies.

In cases of iliac artery occlusion where primary patency was not maintained and there was a need for TLR, after the 1st month, patients continued with acetylsalicylic acid medication alone due to non-compliance with dual antiplatelet therapy. While there is no consensus on the duration of use in peripheral arterial disease, dual antiplatelet therapy is considered more beneficial than mono antiplatelet therapy for preventing thrombotic adverse events following interventions.[23] Dual antiplatelet therapy prevents major adverse limb events such as loss of patency, TLR, and major amputation. However, as the duration of use increases, the rising risk of major bleeding should also be considered.[24] Strict adherence to the prescribed antiplatelet treatment is crucial for maintaining stent patency.

In the study conducted by Tomoi et al.,[25] which treated aorto-iliac arterial disease in 149 patients using balloon-expandable covered stents, residual stenosis, artery rupture resolved with additional stenting, and acute stent thrombosis due to manual compression were encountered. In our study population, technical success was achieved in all patients, and plaque migration occurring during the procedure was treated without complications through stent implantation in three patients. In studies on balloon-expandable stent-grafts for iliac artery occlusions, the mortality rate was 4% in the VISIBILITY study and 4.5% in the BOLSTER study, with these rates being unrelated to the procedure.[21,22] The AVOCADO II study showed a 1-year overall survival rate of 93%.[25] Similarly, in this study, the mortality rate unrelated to the procedure was 5%.

This study has some limitations. First, it is a single-center, retrospective study that lacks a comparative analysis with another stent design. Additionally, mid- and long-term follow-up results were not available due to the recent release of the stent. Multicenter, prospective, randomized, and long-term follow-up studies should be conducted to improve our understanding of the safety and efficacy of this stent.

In conclusion, the early results of iCover balloon-expandable covered stents in the treatment of iliac artery disease are satisfactory. Therefore, this newly introduced stent can be used safely, similar to other balloon-expandable or self-expandable covered stents and bare-metal stents.

Conflict of interest disclosure

The authors declared no conflicts of interest.

References

1. Rossi M, Iezzi R. Cardiovascular and Interventional Radiological Society of Europe guidelines on endovascular treatment in aortoiliac arterial disease. *Cardiovasc Intervent Radiol*. 2014;37(1):13-25. [CrossRef]

2. Aboyans V, Ricco JB, Bartelink MEL, et al. 2017 ESC Guidelines on the Diagnosis and Treatment of Peripheral Arterial Diseases, in collaboration with the European Society for Vascular Surgery (ESVS): Document covering atherosclerotic disease of extracranial carotid and vertebral, mesenteric, renal, upper and lower extremity arteriesEndorsed by: the European Stroke Organization (ESO)The Task Force for the Diagnosis and Treatment of Peripheral Arterial Diseases of the European Society of Cardiology (ESC) and of the European Society for Vascular Surgery (ESVS). *Eur Heart J*. 2018;39(9):763-816. [CrossRef]

3. Virmani R, Kolodgie FD, Dake MD, et al. Histopathologic evaluation of an expanded polytetrafluoroethylene-nitinol stent endoprosthesis in canine iliofemoral arteries. *J Vasc Interv Radiol*. 1999;10(4):445-456. [CrossRef]

4. Quinn SF, Sheley RC, Semonsen KG, Sanchez RB, Hallin RW. Endovascular stents covered with pre-expanded polytetrafluoroethylene for treatment of iliac artery aneurysms and fistulas. *J Vasc Interv Radiol*. 1997;8(6):1057-1063. [CrossRef]

5. Violari E, Payomo A, Schiro BJ, Powell A, Gandhi RT, Pena CS. Endovascular treatment of infrainguinal peripheral arterial disease (PAD): update on stent technology. *Tech Vasc Interv Radiol*. 2022;25(3):100840. [CrossRef]

6. Cortolillo NS, Guerra A, Murphy E, Hoel AW, Eskandari MK, Tomita TM. Outcomes of the Gore® Excluder® iliac branch endoprosthesis using self expanding or balloon-expandable stent grafts for the internal iliac artery component. *J Endovasc Ther*. 2023: 15266028231169177. [CrossRef]

7. Lima GB, Tenorio ER, Marcondes GB, et al. Outcomes of balloon-expandable versus self-expandable stent graft for endovascular repair of iliac aneurysms using iliac branch endoprosthesis. *J Vasc Surg*. 2022;75(5):1616-1623. [CrossRef]

8. Krankenberg H, Zeller T, Ingwersen M, et al. Self-expanding versus balloon-expandable stents for iliac artery occlusive disease: the randomized ICE trial. *JACC Cardiovasc Interv*. 2017;10(16):1694-1704. [CrossRef]

9. Choi WG, Rha SW, Choi CU, et al. Study design and rationale of the 'Balloon-Expandable Cobalt Chromium SCUBA Stent versus Self-Expandable COMPLETE-SE Nitinol Stent for the Atherosclerotic ILIAC Arterial Disease (SENS-ILIAC Trial) Trial': study protocol for a randomized controlled trial. *Trials*. 2016;17(1):302. [CrossRef]

10. Bekken JA, Vroegindeweij D, Vos JA, et al. Editor's choice - two year results of the randomised DISCOVER trial comparing covered versus bare metal stents in the common iliac artery. *Eur J Vasc Endovasc Surg*. 2023;65(3):359-368. [CrossRef]

11. Zeng C, Wu Z, Lei J, et al. Covered stents vs bare metal stents for aortoiliac arterial diseases: a systematic review and meta-analysis. *J Endovasc Ther*. 2023: 15266028231212761. [CrossRef]

12. Li J, Shen C, Zhang Y, Fang J, Qu C, Teng L. Outcomes of covered vs bare metal stents for the treatment of aortoiliac occlusive disease. *J Vasc Surg*. 2024;79(2):330-338. [CrossRef]

13. Mwipatayi BP, Sharma S, Daneshmand A, et al. Durability of the balloon-expandable covered versus bare-metal stents in the covered versus balloon expandable stent trial (COBEST) for the treatment of aortoiliac occlusive disease. *J Vasc Surg*. 2016;64(1):83-94. [CrossRef]

14. Cassano R, Perri P, Esposito A, et al. Expanded polytetrafluoroethylene membranes for vascular stent coating: manufacturing, biomedical and surgical applications, innovations and case reports. *Membranes (Basel)*. 2023;13(2):240. [CrossRef]

15. Laird JR, Loja M, Zeller T, et al. iCAST balloon-expandable covered stent for iliac artery lesions: 3-year results from the iCARUS multicenter study. *J Vasc Interv Radiol*. 2019;30(6):822-829. [CrossRef]

16. Squizzato F, Mosquera-Rey V, Zanabili Al-Sibbai A, et al. Outcomes of self-expanding covered stents for the treatment of external ILIAC artery obstructive disease. *Cardiovasc Intervent Radiol*. 2023;46(5):579-587. [CrossRef]

17. Giles H, Lesar C, Erdoes L, Sprouse R, Myers S. Balloon-expandable covered stent therapy of complex endovascular pathology. *Ann Vasc Surg*. 2008;22(6):762-768. [CrossRef]

18. Feldman DN, Armstrong EJ, Aronow HD, et al. SCAI guidelines on device selection in aorto-iliac arterial interventions. *Catheter Cardiovasc Interv*. 2020;96(4):915-929. [CrossRef]

19. Zanabili Al-Sibbai AA, Camblor Santervás LA, Álvarez Marcos F, et al. Midterm results of endovascular treatment for complete iliac axis occlusions using covered stents. *Ann Vasc Surg*. 2020;63:241-249. [CrossRef]

20. Holden A, Takele E, Hill A, et al. Long-term follow-up of subjects with iliac occlusive disease treated with the viabahn VBX balloon-expandable endoprosthesis. *J Endovasc Ther*. 2023:15266028231165723. [CrossRef]

21. Laird JR, Zeller T, Holden A, et al. Balloon-expandable vascular covered stent in the treatment of iliac artery occlusive disease: 9-month results from the BOLSTER multicenter study. *J Vasc Interv Radiol*. 2019;30(6):836-844. [CrossRef]

22. Rundback JH, Peeters P, George JC, Jaff MR, Faries PL. Results from the VISIBILITY iliac study: primary and cohort outcomes at 9 months. *J Endovasc Ther*. 2017;24(3):342-348. [CrossRef]

23. Beiswenger AC, Jo A, Harth K, Kumins NH, Shishehbor MH, Kashyap VS. A systematic review of the efficacy of aspirin monotherapy versus other antiplatelet therapy regimens in peripheral arterial disease. *J Vasc Surg*. 2018;67(6):1922-1932. [CrossRef]

24. Tsai SY, Li YS, Lee CH, et al. Mono or dual antiplatelet therapy for treating patients with peripheral artery disease after lower extremity revascularization: a systematic review and meta-analysis. *Pharmaceuticals (Basel)*. 2022;15(5):596. [CrossRef]

25. Tomoi Y, Takahara M, Soga Y, et al. Clinical outcome of endovascular therapy using a VIABAHN VBX-covered stent for complex aortoiliac artery disease: the AVOCADO II study. *Heart Vessels*. 2023;38(10):1288-1297. [CrossRef]